Doctoral Dissertation
Doctoral Program in Metrology (31.st cycle)

Development of a fiber optic probe for tumor laser ablation with integrated temperature measurement capabilities

Riccardo Gassino

* * * * * *

Supervisors
Prof. G. Perrone, Supervisor
Prof. A. Vallan Co-supervisor

Doctoral Examination Committee:
Prof. Michele Norgia, Referee, Politecnico di Milano
Prof. Francesco Prudenzano, Referee, Politecnico di Bari

Politecnico di Torino
2019

I hereby declare that, the contents and organisation of this dissertation constitute my own original work and does not compromise in any way the rights of third parties, including those relating to the security of personal data.

. . . . . .

Riccardo Gassino

Turin, 2019

Summary

The combination of new chemotherapies and surgical treatments has dramatically improved the survival rates of people affected by cancer over the last decades. However, these successes are not evenly distributed among the various types of cancer; in particular, little progress has been made in the treatment liver and pancreas tumors.

The Ph.D. activity aimed to contribute by proposing an innovative all-fiber optic applicator with embedded sensing capabilities for the Laser Ablation (LA) treatment of liver and pancreas tumors.

LA is one of the so-called minimally invasive tumor therapies – the others being radio-frequency (RFA) and microwave (MWA) ablation – that rely on the local increase of the temperature above cytotoxic levels to induce the necrosis of malignant cells. In particular, LA exploits the temperature increase due to the tissue absorption of a high power laser beam, usually at near-infrared wavelengths. These hyper-thermal therapies constitute an alternative to more traditional surgical resection and are particularly attractive because of their reduced post-operative discomfort since they can be performed through percutaneous needles and affect only a limited body zone. Although LA has already demonstrated several advantages over competing procedures, its diffusion is still limited. One of the main reasons is the lack of a proper treatment protocol to be used first for planning and then to monitor as it progresses. A first step towards the definition of such procedure is the real-time monitoring of the temperature reached by the tissue under treatment so that it is possible to ensure reaching the proper cytotoxic level while avoiding damages to the surrounding healthy tissue.

In this framework, the Ph.D. activity explored the feasibility of a new type of applicator for LA that embeds Fiber Bragg Gratings (FBGs) as temperature sensors. FBGs were selected because being all-fiber-based are entirely compatible with the laser radiation and present several advantages with respect to other fiber optic sensors due to their technological maturity and widespread use in different fields of engineering.

In a first phase, several commercial FBGs were encapsulated in different embodiments to reduce the effect due to strain cross-sensitivity and characterized in uniform temperature conditions in order to find their sensitivity. Then, the errors

due to their use with a real temperature distribution in simulated operative conditions have been thoroughly analyzed. Indeed, even if FBGs are commonly employed for several applications, no detailed studies of their response and errors in presence of non-uniform temperature distributions, which are typical of LA, were present in the literature. Numerical models to simulate the sensors readings in presence of steep temperature gradients have been developed and the results have been experimentally confirmed with dedicated setups. The effect of the sensor position, length, and embodiment in the temperature distribution estimation have been quantified for different sensor configurations.

Then, the work has focused on the development of a new applicator to simultaneously deliver a high power laser beam with a suitable pattern to match the tumor size and sense the temperature. This has required studying an appropriate fiber surface modification to allow also the lateral irradiation. Using a double-cladding specialty fiber, it has been possible to write several FBG sensors in the inner core for temperature mapping and use the inner cladding to guide the beam for LA. The irradiation pattern and the integrated sensors response have been characterized in phantoms to allow reproducible test conditions and then validated using ex-vivo porcine liver. Finally, the realized applicator has been tested in in-vivo animal cases, obtaining preliminary results on the clinical validity of the proposed approach.

Acknowledgements

And I would like to acknowledge all the people that made possible the realization of this work and in particular:

Prof. Emiliano Schena, Dr. Carlo Massaroni and all the people working with them at the Campus Biomedico in Roma, for their hospitality, their professionalism and their willingness in sharing works and ideas;

Prof. Paola Saccomandi, Dr. Giuseppe Quero, Dr. Alfonso Lapergola and all the people that made possible the incredible experience held in Strasbourg, a unique chance to make steps forward in the tumor laser ablation.

Moreover, I would also like to acknowledge the people that worked with me during this period, even if the results obtained together have not been reported here, for conciseness:

Prof. Daniele Tosi and his group at Nazarbayev University in Kazakhstan, for the efforts made together trying to understand chirped FBGs behavior under temperature gradients;

Prof. Ivana Fenoglio, Prof. Chiara Riganti, Mrs. Ida Kokalari and their group at the University of Torino, for the results obtained in the free radical activity for tumor treatments.

Contents

List of Tables

List of Figures

Acronyms

ASE	Amplified Spontaneous Emission.
CCD	Charge Coupled Device.
CT	Computed Tomography.
DC	Double Cladding.
FBG	Fiber Bragg Grating.
FEM	Finite Element Method.
GFRP	Glass Fiber Reinforced Polymer.
HCC	Hepatocellular Carcinoma.
HPV	Human Papilloma Virus.
IHU	Institut de Chirurgie Guidée par l'Image.
IR	Infra-Red.
LA	Laser Ablation.
LD	Laser Diode.
MRI	Magnetic Resonance Imaging.
MWA	Micro-Wave Ablation.
NIR	Near Infra-Red.
OFDR	Optical Frequency Domain Reflectometer.
OSA	Optical Spectrum Analyzer.
OTDR	Optical Time Domain Reflectometer.
PRF	Proton Resonance Frequency.

RFA	Radio-Frequency Ablation.
SLED	Super-luminescent LED.
SMS	Single mode - Multi mode - Single mode.
SNR	Signal to Noise Ratio.
US	Ultrasound.
UV	Ultra-Violet.
VIS	Visible.
WHO	World Health Organization.

List of Publications on Journals

[1] Liu Y., **Gassino R.**, Braglia A., Vallan A., Perrone G., *"Fibre probe for tumour laser thermotherapy with integrated temperature measuring capabilities"*, ELECTRONICS LETTERS, 52:10(2016), pp. 798-800

[2] Saccomandi P, Varalda A., **Gassino R.**, Tosi D., Massaroni C., Caponero M. A., Pop R., Korganbayev S., Perrone G., Diana M., Vallan A., Costamagna G., Marescaux J., Schena E., *"Linearly chirped fiber Bragg grating response to thermal gradient: from bench tests to the real-time assessment during in vivo laser ablations of biological tissue"*, JOURNAL OF BIOMEDICAL OPTICS, 22:9(2017), pp. 1-9

[3] **Gassino R.**, Liu Y., Konstantaki M., Vallan A., Pissadakis S., Perrone G., *"A Fiber Optic Probe for Tumor Laser Ablation with Integrated Temperature Measurement Capability"*, JOURNAL OF LIGHTWAVE TECHNOLOGY, 35:16(2017), pp. 3447-3454

[4] Schena E., Davrieux F., Saccomandi P., Tosi D., **Gassino R.**, Massaroni C., Lo Presti D., Costamagna G., Perrone G., Vallan A., Diana M., Marescaux J., *"Solutions to improve the outcomes of thermal treatments in oncology: multipoint temperature monitoring"*, IEEE JOURNAL OF ELECTROMAGNETICS, RF AND MICROWAVES IN MEDICINE AND BIOLOGY, (2018), pp. 1-8

[5] **Gassino R.**, Pogliano J., Perrone G., Vallan A., *"Issues and characterization of fiber Bragg grating based temperature sensors in the presence of thermal gradients"*, MEASUREMENT, 124(2018), pp. 15-19

[6] Saccomandi P., Quero G., **Gassino R.**, Lapergola A., Guerriero L., Diana M., Vallan A., Perrone G., Schena E., Costamagna G., Marescaux J., Di Matteo F. M., *"Laser ablation of the biliary tree: in vivo proof of concept as potential treatment of unresectable cholangiocarcinoma"*, INTERNATIONAL JOURNAL OF HYPERTHERMIA, (2018)

[7] Korganbayev S., Orazayev Y., SovetovS., Bazyl A., Schena E., Massaroni C., **Gassino R.**, Vallan A., Perrone G., Saccomandi P., Caponero M. A., Palumbo G., Campopiano S., Iadicicco A., Tosi D., *"Detection of thermal gradients through fiber-optic Chirped Fiber Bragg Grating (CFBG): Medical thermal ablation scenario"*, OPTICAL FIBER TECHNOLOGY, (2018), pp. 48-55

Chapter 1

Introduction

The World Health Organization (WHO) [1] states that "cancer is a leading cause of death worldwide", with an estimation of about 1 in 6 deaths in 2018 due to cancer, 70% of which occurring in low- and middle-income countries. In 2016 the number of global cancer-related deaths was half of those due to cardiovascular diseases, the main cause of death, but almost three times those related to respiratory diseases, the third cause (Fig. 1.1). Besides for the social impact, cancer implies, therefore, health care costs, which was estimated at approximately US $ 1.16 trillion in 2010.

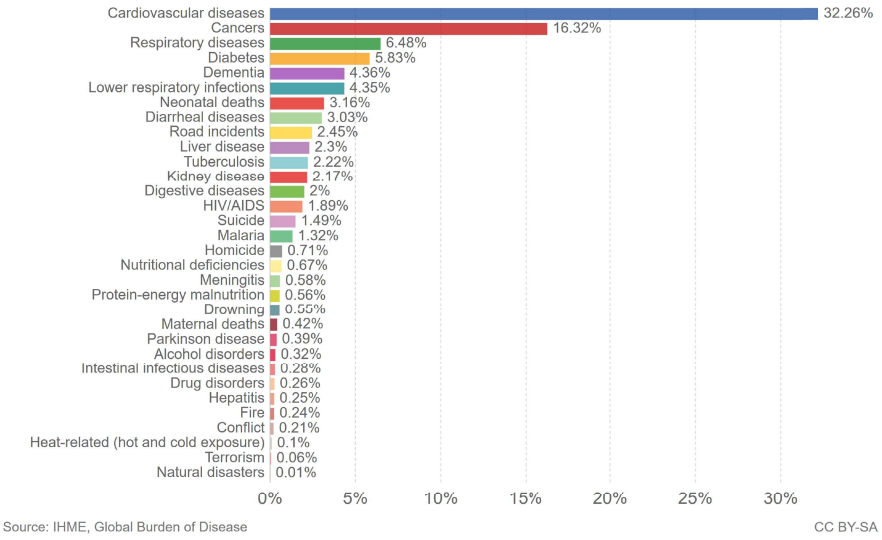

Figure 1.1: Annual number of deaths by cause, World, 2016. Data refers to the specific cause of death, which is distinguished from risk factors for death, such as air pollution, diet and other lifestyle factors [2].

Different types of cancer exist (Fig. 1.2), with different causes. However, according to the cited document of WHO, in high-income countries "one-third of deaths from cancer are due to the 5 leading behavioral and dietary risks: high body mass index, low fruit and vegetable intake, lack of physical activity, tobacco use, and alcohol use". On the other hand, "cancer causing infections, such as hepatitis and Human Papilloma Virus (HPV), are responsible for up to 25% of cancer cases in low- and middle-income countries" [3].

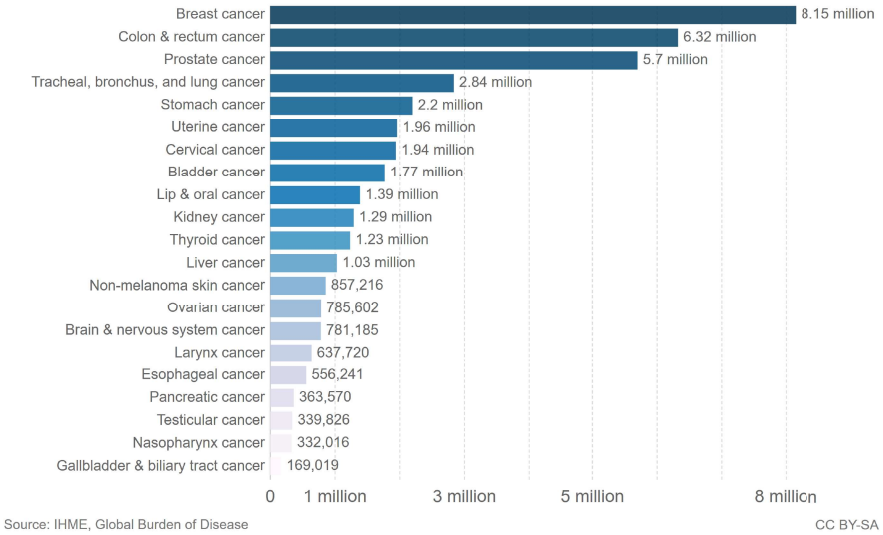

Figure 1.2: Total number of people suffering from cancer in the world in 2016, differentiated by cancer type and measured across both sexes and all ages [2].

Comparing the number of people affected by cancer by type in Fig. 1.2 with the corresponding deaths in Fig. 1.3, it is evident that for some cancers current therapies are fairly adequate (e.g., for breast cancer), while for others they are clearly ineffective (e.g., for liver and pancreas cancers) [4]. Indeed, cancer mortality rates are globally decreasing in countries of all income levels, especially for most common types of malignancies, with the exception of liver cancer in both sexes; this "can be explained by lifestyle exposure changes and lack of liver cancer screening protocol, vaccination, or known curative treatment" [5]. In other words, despite the progress of chemotherapies and of surgery, liver tumors – but also other types tumors of the gastrointestinal tract, such that of the pancreas – still require a lot of research efforts to improve the survival rates.

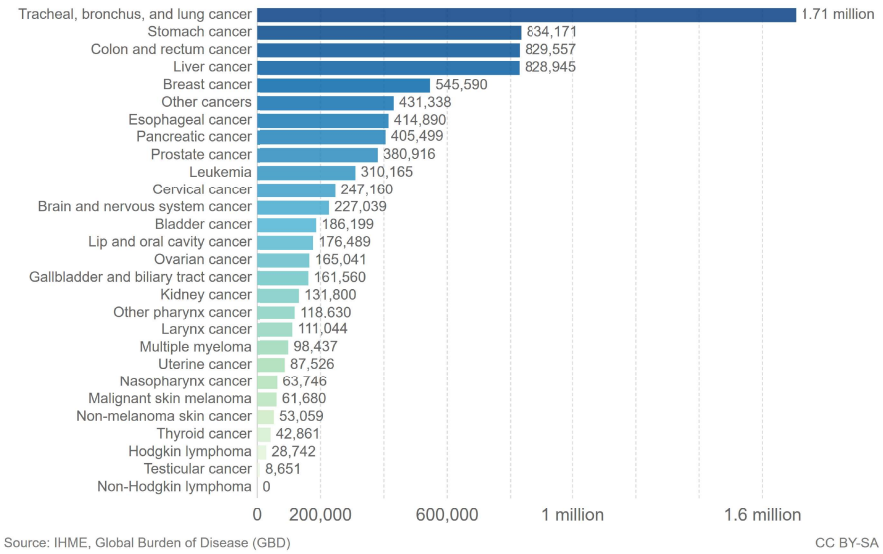

Figure 1.3: Total annual number of deaths from cancers across all ages and both sexes, broken down by cancer type [2].

This thesis aims at providing a contribution to the fight against these types of cancer by reporting the results obtained during the Ph.D. studies, which have been devoted to the investigation of a new laser tool for the minimally invasive treatment of solid tumors in deep-laying organs, with a particular focus on the liver cancer. Before going into the details of the Ph.D. activities, next sections describe the most common techniques that are nowadays employed to treat liver cancer and the possibilities to control these treatments.

1.1 Minimally-invasive tumor thermal treatments

The liver tumor is said to be "primary", Hepatocellular Carcinoma (HCC), if its origin is in the liver or "secondary" – the most common type – if it is a metastasis coming from another site, such as pancreas, colon, stomach, breast, or lungs [6]. In both situations, "surgical resection remains the best treatment of choice" with "a long-term survival of 25% up to 41% after five years" [7], even if it can be applied only to patients in which the tumor affects a confined region only and co-morbidities are not present. An alternative is represented by less-invasive techniques – generally known as "ablations" –, which are suitable, however, mainly for lesions smaller than 3 cm in diameter [8][9].

Among these techniques, several new percutaneous approaches have been proposed in recent years. In these cases, different treatments can be performed locally on the tumor site by mean of thin tools inserted via small needles through the skin (Fig. 1.4), with many advantages related to the abbreviated recovery period [10].

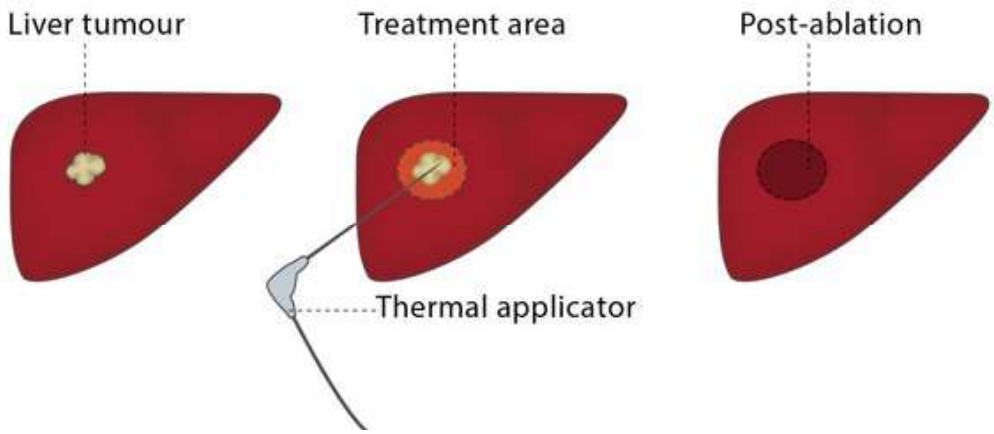

Figure 1.4: Schematic of the procedure for general tumor ablation. The applicator is inserted percutaneously into the liver in order to reach the tumor and cause the cell necrosis (often by delivering electromagnetic energy); afterward, the dead cells are absorbed from the organism [11].

These minimally invasive approaches are usually performed under imaging control and, in most of the cases, they rely on the cell necrosis caused by thermal effects. Indeed, by providing to the cells a thermal shock for the appropriate amount of time (Fig. 1.5), it is possible to obtain permanent cytotoxic effects.

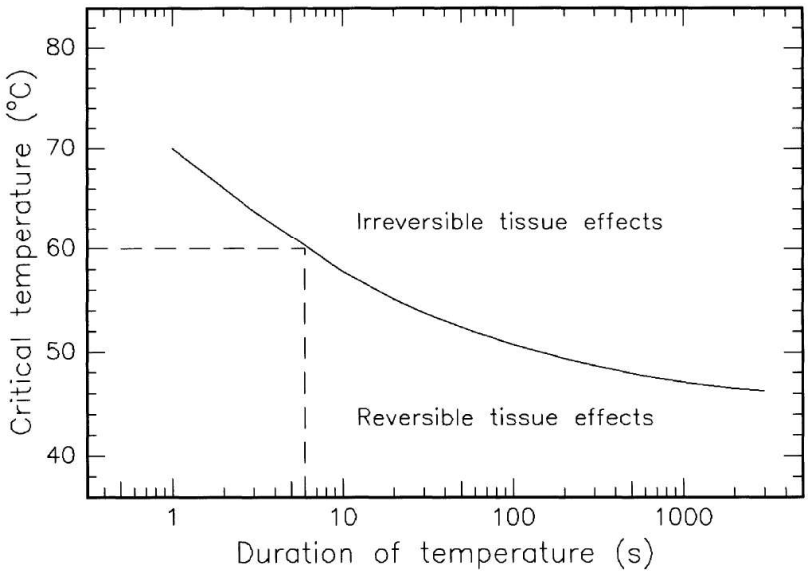

Figure 1.5: Irreversible effects on cells depending on the temperature-procedure duration combination [12].

In particular, the biological effects on the cells caused by a temperature increase

are those reported in Tab. 1.1. In practice, the temperature is usually kept between 55 °C to 100 °C for 5-10 minutes, in order to have a good tissue response in reasonable time and to avoid too high temperatures that would carbonize the tissue, hampering the treatment outcomes besides for being dangerous for surrounding healthy tissue.

Table 1.1: Main biological effects of temperature increase on cells [12].

Temperature °C	Effect
37	Normal
45	Hypertermia
50	Reduction in enzyme activity, cell immobility
60	Denaturation of proteins and collagen, coagulation
80	Permeabilization of membranes
100	Vaporization, thermal decomposition
>100	Carbonization
>300	Melting

In the next subsections, the most common minimally-invasive thermal therapies currently employed to treat liver (and not only) cancer are described.

1.1.1 Radio-frequency ablation

Radio-Frequency Ablation (RFA) is the thermal ablation method with the longest history [13]. In this treatment, an alternate current with a frequency in the 375 kHz to 500 kHz range [14] is delivered through a thin active electrode that is inserted into the tumor mass and a larger one, the grounding pad, that is stuck on the patient skin to close the electrical loop [15]. The current flows into the tissues producing the ionic agitation, which turns into the heat production [16].

Typical active electrodes have a needle shape, in which the body is insulated but the tip, for a length of 1 cm to 3 cm; in this cases, however, the heating is mainly in the proximity of the active part of the electrode, with a consequent narrow ablation region. To overcome this, multiple electrode systems have been proposed (Fig. 1.6 (left)), but the insertion of more than one needle in the correct position is challenging.

More recent electrodes have an umbrella shape as shown in Fig. 1.6 (center-right); obviously, they are inserted closed through a needle and then the hooks can be expanded to fit different tumor sizes [18]. The needles employed for the active electrode insertion are from 14 to 17 Gauges, which correspond to 1.1 mm to 1.6 mm of external diameter.

The RF generators usually deliver 50 W to 200 W of electrical power and cost between 12.000 $–30.000 $, whereas each applicator, the disposable part, costs

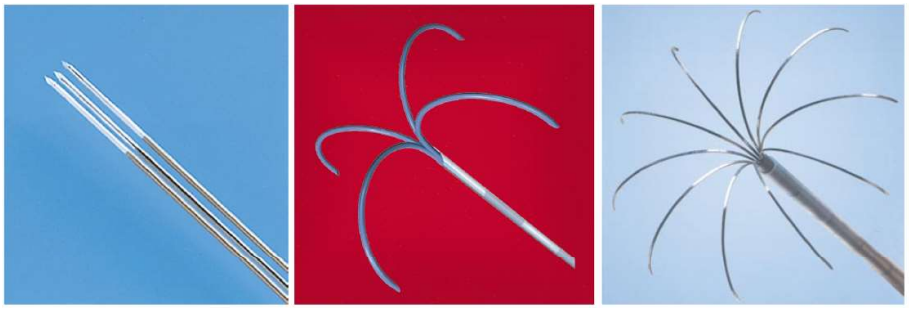

Figure 1.6: Comparison between different RFA applicators: multiple electrode type employed to increase the ablation size (left) and two versions of the more sophisticated umbrella-shape electrode (center and right) [17].

between 500 $ –1000 $; hence RFA results quite expensive [17]. Needles positioning is usually performed under Ultrasound (US) guide, but there are commercial devices that are compatible with Computed Tomography (CT) and Magnetic Resonance Imaging (MRI) in order to achieve better results [19], even if these techniques require more expensive facilities and therefore are less employed.

Although some commercial devices can be used with CT and MRI for the positioning in those situations where the US are not suitable, a possible CT/MRI temperature mapping to monitoring the procedure is slightly compromised due to artifacts induced by the applicator material [20, 21]. Therefore, to perform a treatment monitoring without imaging support, different solutions are implemented in the RFA systems itself. The most common solutions currently available are tiny thermocouples located inside the active portion and the impedance evaluation of the current path inside the patient body [22, 23, 24, 25].

1.1.2 Microwave ablation

Despite the introduction of more effective applicators, the main limitation of RFA is tumor size, which is usually less than 3 cm [26]. To overcome this limitation, MWA has been proposed over the years and nowadays this is the second most employed ablation technique worldwide [27]. In MWA an electromagnetic field in the 0.9 GHz to 2.5 GHz frequency range is applied through an antenna percutaneously inserted into the tumor, without any grounding pad on the patient (Fig. 1.7).
This field is less subjected to tissue desiccation and variability, hence, theoretically, more substantial ablation can be performed [28, 29]. Even if an experimental characterization of the tissue properties is still missing [30], preliminary clinical trials suggested that MWA can replace the RFA [31].

The microwave generator can provide about 60 W and costs around 45.000 $. The antennas are, usually, 25 cm long and are applied by mean of 14 Gauges needles.

Figure 1.7: Example of a commercial MWA system, constituted by the microwave generator and the antenna applicator; from *(Solero® - MWA System*, Balmer Médical SA, Rte de Provence 52, CH-1426 Concise).

Each applicator is not reusable and costs about 500 $ [17]. Even in this case, some thermocouples can be embedded inside the applicator to measure the temperature reached by the tissues and control the delivered power. Moreover, several external probes, also fiber optic based, are proposed in the literature to be combined with the antenna and measure the temperature in different regions [32, 33].

1.1.3 Laser ablation

Another interesting opportunity to perform the tissue ablation is exploiting the absorption of laser light by tissue, the so-called Laser Ablation (LA). Laser light is generated by stimulated emission [34] and, unlike the light coming from the sun or a lamp, is almost monochromatic (single wavelength) and more "ordered"; thus it can be collimated and focused more efficiently, allowing higher power densities that are useful for many surgical applications [35]. The use of laser light for ablation has some intrinsic advantages, such as the absence of currents (so no electrocution risks) and, most important, the possibility to deliver the beam by means of thin optical fibers. This constitutes one of the main advantages of LA over the other proposed techniques since optical fibers are made with dielectric materials only and are therefore suitable to be employed under MRI and CT guidance. Lasers emitting at different wavelengths covering the entire spectrum from Ultra-Violet (UV) to Infra-Red (IR) exist. One of the most widespread, and less expensive, family is semiconductor Laser Diodes (LDs), which, as the name implies, have a diode junction structure and emit light exploiting the recombination of electrons and holes; they typically emit in the Visible (VIS) or Near Infra-Red (NIR) ranges depending on the semiconductor alloy forming the junction (e.g., GaN, GaAs, InP, etc.). LDs have widely employed for several applications in medicine thanks to the possibility to have different effects on different tissues exploiting the relation between the wavelength and the penetration depth. For example, LDs emitting at a wavelength of 670 nm are often employed for external applications, like in

dermatology, while those with a wavelength between 800 nm to 1200 nm are usually more suitable for deep-laying tissue structures [36].

In particular, considering the absorption of the liver reported in Fig. 1.8, a good compromise between tissue absorption and penetration depth (hence the extension of the treated tumor mass) occurs for wavelengths in the region between 800 nm to 1000 nm.

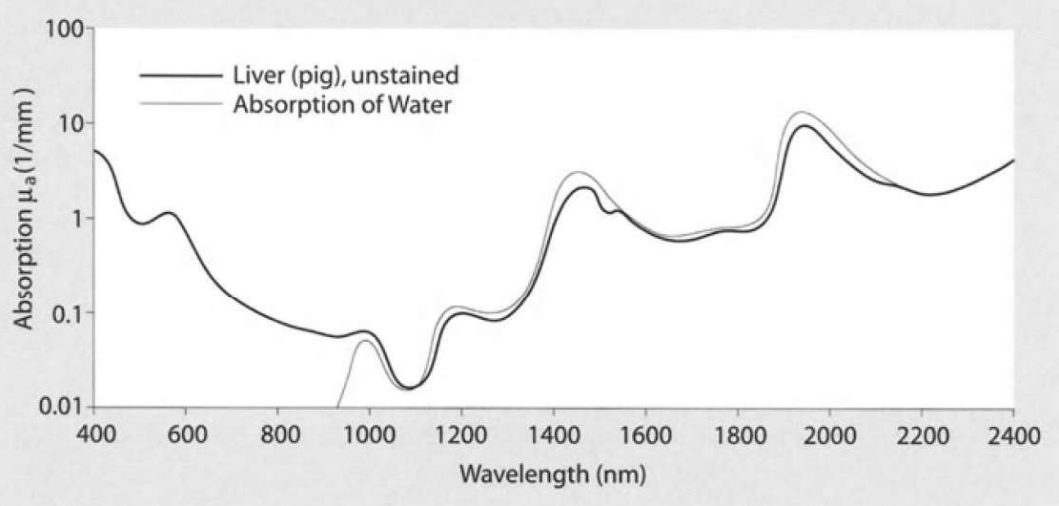

Figure 1.8: Optical properties of 100 unstained pig liver. Mean values from three measurements, mean thickness 0.5 mm [37].

The tissue penetration depth is one of the drawbacks of the laser light, which can turn into tiny ablations due to the easy tissue charring close to the fiber tip delivering the energy. To prevent this problem, in recent years, several solutions have been proposed to increase the treatment area, from cooled applicators (which, however, increase the tool diameter) to multiple applicators or diffusing fibers [38, 39].
According to the application, the laser can be modulated (pulsed) or continuous; the former is usually applied for cutting purposes, while the latter is employed for heating.

A typical laser system can deliver few watts for each fiber, in the case of conventional fiber emitting from the tip or up to 30 W in the case of diffusing applicators (in continuous emission mode). The cost can be of 20.000 $ – 50.000 $ for the laser system and up to 2.000 $ for the applicator, which however can be used to treat up to 50 patients citeRFAneedles.

Considering these possibilities, in the thesis work a diode laser was used with a nominal wavelength of 980 nm (BMU25-9xx-01/02-R, *Oclaro*) and maximum output power of 25 W, in a continuous way. Then, the delivery fiber has been modified in order to become diffusive, as described in 5. This allows on the one side to

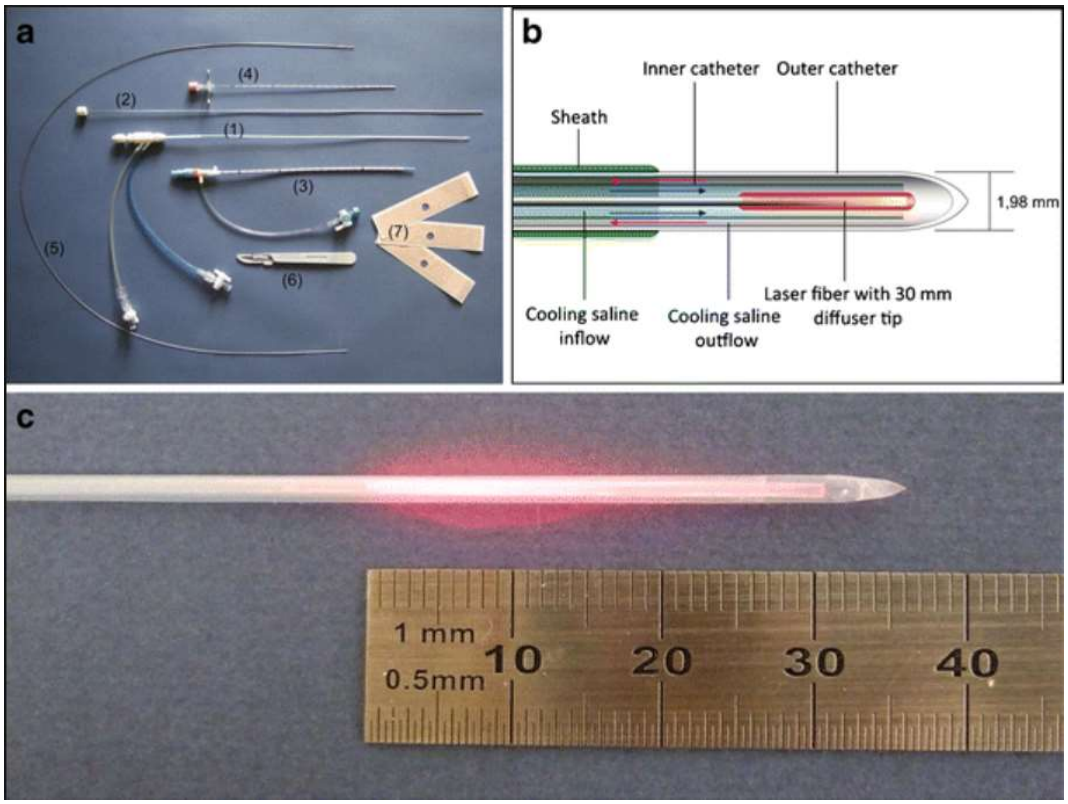

Figure 1.9: Example of commercial diffusing fiber with cooling system [40]: a) insertion kit to introduce the fiber percutaneously in the liver; b) scheme of the applicator; c) picture of the applicator.

increase the treatment region, avoiding carbonizations, but on the other side to easily include some temperature sensors in the delivery fiber, since the region to be monitored is larger. This possibility is of particular relevance since so far only external probes have been proposed on the market [41], where a further insertion has to be performed on the patient with all the related drawbacks of the correct positioning (Fig. 1.10).

The possible sensors that can be integrated into the delivery probe are considered and described in the following.

1.2 Treatment temperature monitoring

In general, there are several possibilities to monitor the temperature increase due to the energy deposition into the tissues. Many of these solutions have already been discussed in the previous sections and are already available with commercial devices. However, in the case of the laser ablation, particular attention has to be paid, because conventional sensors originate large artifacts when exposed to laser

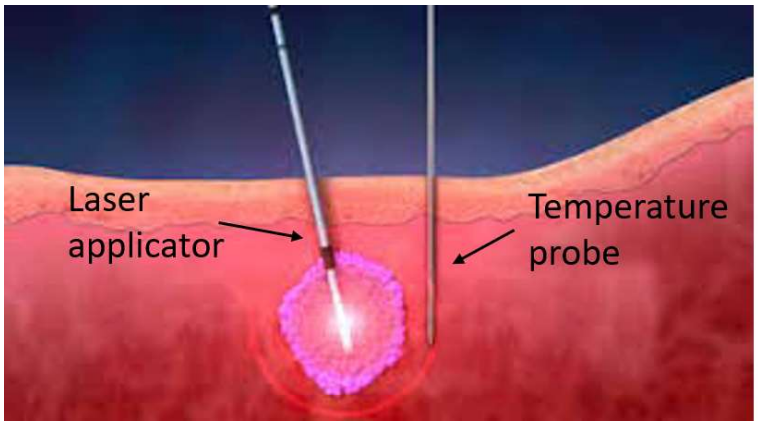

Figure 1.10: Representation of a laser ablation monitored with an external temperature probe, positioned in the proximity of the laser applicator [41].

light. Advantages and disadvantages of the most common possibilities currently employed are discussed in this section.

1.2.1 Metallic sensors

The first possibility is to use tiny metallic sensors, usually thermocouples, which are widespread and cheap. Metallic sensors can be embedded into the same applicator that delivers the energy, which is metallic for RF and MW ablation, so without changing the temperature distribution in the tissues, or, they can be used in external probes to measure in the tumor boundaries [42]. However, in the case of LA, it would not be possible to include a metallic sensor in the applicator, since it is an optical fiber; therefore only external temperature probes are possible. Although this solution is feasible and has been employed in several works [43, 44], it has to be considered that the metallic sensor strongly absorbs the laser light, providing large artifacts [45, 46] (Fig. 1.11) that can be up to about 5 °C for a distance of 1 cm from the applicator [47].

Therefore, even if it could be possible to monitor the temperature increase due to the laser absorption in the tissues with a thermocouple probe, the practical use is cumbersome because it requires correcting the reading as a function of the distance from the applicator and the operating power.

1.2.2 Imaging

The most interesting possibility comes from imaging techniques, such as CT and MRI. With these, it is theoretically possible to obtain the temperature mapping inside the tissues in a totally non-invasive way. In CT, the image is obtained from the attenuation of x-rays in the tissue with the following formula:

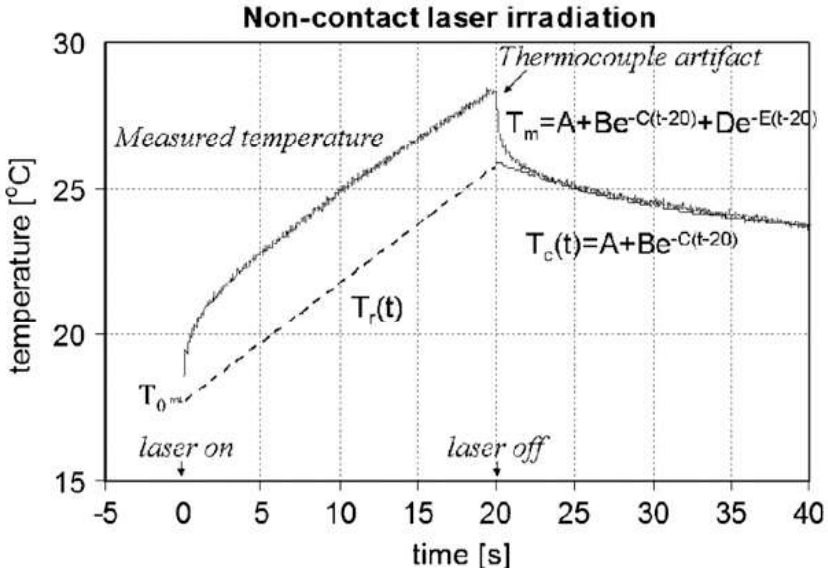

Figure 1.11: Temperature measurement of a thermocouple not in contact with the laser source during a canine prostate ablation. The figure reports the thermocouple artifact, the corrected cooling curve ($t > 20\,\mathrm{s}$) and the calculated tissue temperature during laser exposure (dashed line). T_m: measured temperature; T_c: calculated temperature ($t > 20\,\mathrm{s}$); T_r: reconstructed temperature during laser exposure [48].

$$CT(x,y) = 1000 \cdot \frac{[\mu(x,y) - \mu_{H_2O}]}{\mu_{H_2O}} \tag{1.1}$$

where $\mu(x,y)$ and μ_{H_2O} are the tissue and the water (taken as a reference) attenuation coefficients, respectively. The tissue attenuation is related to its density and therefore to the temperature by:

$$\rho(T) = \frac{\rho(T_0)}{1 + \alpha\Delta T} \tag{1.2}$$

with T_0 the reference temperature, ρ the tissue density and α the coefficient of tissue expansion with the temperature [49].

Due to CT x-rays nature, in recent years particular attention has been given to the MRI because it uses non-ionizing radiations, even if it is a more expensive technology, not always available in all facilities and with some limitations for the patients (no metallic implants allowed, claustrophobia, etc...) [50].

Several MRI techniques have been proposed to retrieve the tissue temperature distribution but the most promising are based on the spin-lattice relaxation time T_1 and on the Proton Resonance Frequency (PRF) shift sequence. The former is related to the temperature by:

$$T_1 \propto \exp\left(-\frac{E_a(T_1)}{kT}\right) \tag{1.3}$$

where $E_a(T_1)$ is the activation energy of the relaxation process, k is the Boltzmann constant and T is the absolute temperature. This method has a high sensitivity even with low fields, but it is tissue dependent. The other method, the PRF, is less tissue dependent, has an even higher sensitivity and is linear with the temperature in a broader range. However, it requires a very uniform field distribution to be accurate and therefore it cannot be used with open magnets, preventing the possibility to have access to the patient inside the MRI [51] during the treatment.

Given the extraordinary potential of these techniques, massive efforts have been made to overcome their drawbacks [52, 53]. However, the most recent results still report substantial inaccuracies and long acquisition time [54, 55]; therefore, they are still not suitable to be used for real-time monitoring of an LA process.

1.2.3 Fiber optic sensors

Fiber optic sensors constitute another promising possibility for the temperature measurement during an LA process.

Optical fibers are cylinders made of concentric rods of dielectric materials, such as glass or plastic, with diameters in the order of hundreds of micrometers; they capable of guiding light, with low losses, by exploiting the total internal reflection at the interface between the inner rod, called "core" and the outer rod, called "cladding". For mechanic and protection reasons, other buffer layers are then added over the cladding, as depicted in Fig. 1.12.

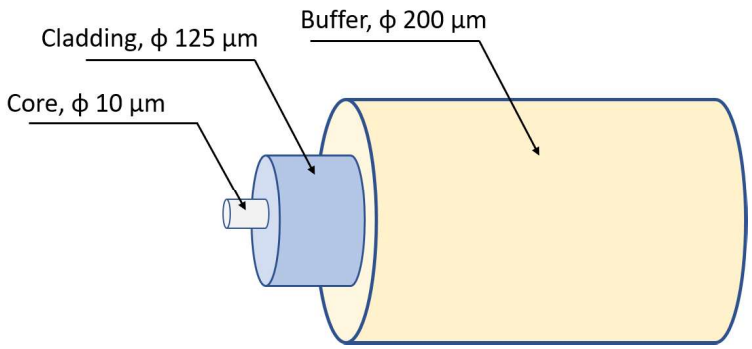

Figure 1.12: Structure of an optical fiber: the dimensions are those typical for a single mode fiber employed for telecommunications.

Depending on the core size, operation wavelength, and core-cladding refractive index difference, an optical fiber can propagate one or more electromagnetic field

configurations, called “modes”; therefore it can be correspondingly called “single” or “multimode” fiber [56].

Optical fibers have been extensively used for fabricating several kinds of sensors for the most widespread applications. These sensors are commonly classified in two groups: intrinsic sensors, when the optical fiber is itself the sensing element; extrinsic sensors when the optical fiber conveys the light, which interacts with the measurand and changes its characteristics [57].

Considering the temperature measurement, the main types of fiber optic sensors are:

- *Fluorence sensors*: sensors based on the dependency of the fluorescence decay time of a phosphor material with temperature. A light source, coupled inside a standard optical fiber, is used to excite the phosphor, and its response is acquired with a photodetector and processed to recover the decay time [58];

- *Interferometric sensors*: sensors based on the shift of the interference pattern with temperature; one of the most promising examples is a Mach-Zehnder like structure based on the interference between fundamental and first high order mode in a Single mode - Multi mode - Single mode (SMS) structure [59]. These sensors exhibit a very large sensitivity but their cross-sensitivity issues and sizes still prevent them from being effectively employed for the considered LA applications.

- *Distributed temperature sensors*: sensors in which the entire fiber length is employed as a sensor. The measure can be performed in the time, Optical Time Domain Reflectometer (OTDR), or frequency , Optical Frequency Domain Reflectometer (OFDR), domains by measuring the Rayleigh backscattering or the Brillouin stimulated scattering. This technique is theoretically able to provide a very high spatial resolution, less than 1 mm, over quite long distances [60];

- *Emissivity based sensors*: a possibility to measure the tissue temperature could be given by the IR emissions shift from the target, due to its temperature increase. This IR light can be collected from an optical fiber and delivered to a sensor in order to be measured. However, the amount of light collected can be very tiny and is principally due to the temperature of the tissue right in front of the fiber tip. In order to measure the temperature in more than one point, a bundle of fiber has to be devised and this can be difficult and can increase the probe diameter. Moreover, since in order to keep the fiber bundle together it must be embedded into a capillary, each sensing fiber could collect only the light coming from the capillary and, therefore, it could lead to temperature errors.

- *Fiber Bragg Gratings (FBGs)*: sensors better introduced in the next chapter since they are the solution investigated in detail in this thesis because they are a good compromise between performance and technological maturity. Indeed, while fluorescence-based sensors can provide large artifacts when employed with ablation laser light [61, 62], due to the laser absorption from the phosphor material, distributed sensors have good performances but their interrogation system is expensive ($\sim$ 100.000 \$), FBGs can be interrogated with relatively cheap systems ($\sim$ 10.000 \$) and are extremely compatible with the laser radiation [63].

Chapter 2

Fiber Bragg gratings

Among the various fiber optic sensors, in this thesis, the focus is on FBGs, since they represent the most promising sensors to be used for LA monitoring for their unique combination of technology maturity and sensing performance. Moreover, they induce very little perturbation due to laser light absorption, can be multiplexed along the same fiber to measure in several points and can be easily integrated into the applicator with the high power laser light delivery. The last feature is the most important for this work because the aim is, on the one hand, to study an FBG based probe to sense the temperature; on the other hand, to develop an applicator capable of both delivering the light beam used for ablation and integrating control process sensors. This solution is thoroughly described in Chapter 5.

FBGs are a periodic perturbation of the refractive index inscribed in the core of a single-mode optical fiber. There are several methods to induce this perturbation in standard fibers [64, 65], all based on the photosensitivity mechanism for which the fiber core refractive index increases if it is exposed to a proper light source; the most common exploit a UV intense laser beam and are:

- *interference lithography method*, in which theUV laser beam is split in two and then recombined forming a certain angle to create the desired interference periodic pattern into the fiber sample, in turn, capable of inducing a periodic refractive index variation;
- *phase mask method*, in which the UV laser light is launched through a silica phase mask with a defined period, obtaining at the output again a periodic light pattern.

An alternative approach makes use of a *femtosecond laser* (an ultra-fast laser capable of emitting pulses with a duration of few hundred femtoseconds and for a peak power reaching gigawatt) to induce localized material compaction and thus writing the FBG point by point.

If a broadband light source is launched through a grating, a reflection peak is obtained for the wavelength that satisfies a specific condition (the Bragg condition)

as a consequence of the coherent combination of the various reflections originated by periodic perturbation. All the other wavelength are transmitted with very low losses (Fig. 2.1).

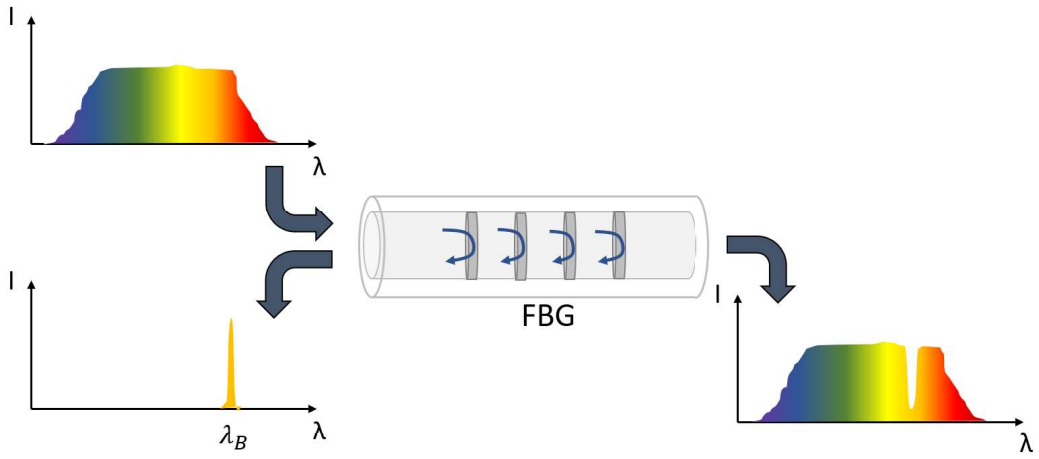

Figure 2.1: FBG working principle. If a broadband light is launched into a fiber, with an FBG inscribed, only a certain wavelength will be reflected wile the others are transmitted.

Given their notch response, FBGs have been mainly employed first as filters in optical communications. However, since the Bragg wavelength also depends on the temperature and strain applied to the grating, more recently they have been widely used as sensors structural health monitoring [66] and temperature measurements in particular conditions or harsh environments [67, 68].

In the next sections are provided and discussed all the equations that relate FBGs reflection peak position with strain and temperature, a model based on transmission lines to emulate the sensor response in different conditions and different acquisition systems to interrogate the FBGs.

2.1 Sensing principles

As mentioned before, launching a broadband light source into an FBG, only the wavelengths close to the Bragg condition are reflected, while all the other wavelengths undergo an extremely weaker reflection because of the phase mismatch. This condition can be written as [69]:

$$\lambda_B = 2n_{eff}\Lambda \tag{2.1}$$

where λ_B is the Bragg wavelength (i.e., the wavelength at which the reflection peak is centered), n_{eff} is the modal effective index and Λ is the refractive index

modulation period. In order to understand the relation between grating temperature/strain variation and λ_B shift, it is necessary to take the differential of the Eq. 2.1:

$$\begin{aligned} \mathrm{d}\,\lambda_B &= \frac{\delta\lambda_B}{\delta\varepsilon}\mathrm{d}\,\varepsilon + \frac{\delta\lambda_B}{\delta T}\mathrm{d}\,T = \\ &= \left[\frac{\delta}{\delta\varepsilon}2n_{\mathrm{eff}}\Lambda\right]\mathrm{d}\,\varepsilon + \left[\frac{\delta}{\delta T}2n_{\mathrm{eff}}\Lambda\right]\mathrm{d}\,T = \\ &= \left[2n_{\mathrm{eff}}\frac{\delta\Lambda}{\delta\varepsilon} + 2\Lambda\frac{\delta 2n_{\mathrm{eff}}}{\delta\varepsilon}\right]\mathrm{d}\,\varepsilon + \left[2n_{\mathrm{eff}}\frac{\delta\Lambda}{\delta T} + 2\Lambda\frac{\delta 2n_{\mathrm{eff}}}{\delta T}\right]\mathrm{d}\,T \end{aligned} \tag{2.2}$$

dividing the Eq. 2.2 by $\lambda_B = 2n_{\mathrm{eff}}\Lambda$ it becomes:

$$\frac{d\lambda_B}{\lambda_B} = \left[\frac{1}{\Lambda}\frac{\delta\Lambda}{\delta\varepsilon} + \frac{1}{n_{\mathrm{eff}}}\frac{\delta n_{\mathrm{eff}}}{\delta\varepsilon}\right]d\varepsilon + \left[\frac{1}{\Lambda}\frac{\delta\Lambda}{\delta T} + \frac{1}{n_{\mathrm{eff}}}\frac{\delta n_{\mathrm{eff}}}{\delta T}\right]dT \tag{2.3}$$

where the first part represents the strain effect, while the second is associated with temperature variations. In particular, the strain acts in two ways on the FBG reflection: it modifies the grating period Λ but also the n_{eff} value (photo-elastic effect). The latter, can be expressed through the photo-elastic coefficient p_e as:

$$\Delta\lambda_B = (1 - p_e)\,\lambda_B\varepsilon \tag{2.4}$$

where p_e ($\sim 0.22 \times 10^6 \mu\varepsilon^{-1}$ for silica fibers) is given by:

$$p_e = \left(\frac{n_{\mathrm{eff}}^2}{2}\right)[p_{12} - \nu\,(p_{11} + p_{12})] \tag{2.5}$$

where p_{11} and p_{12} are the components of the strain-optic tensor and ν is the Poisson's ratio.

The relation between temperature changes and Bragg wavelength shift can be written as:

$$\Delta\lambda_B = (\alpha + \xi)\,\lambda_B\Delta T \tag{2.6}$$

where $\alpha = \left(\frac{1}{\Lambda}\right)\left(\frac{\delta\Lambda}{\delta T}\right)$ is the thermal expansion coefficient, $\xi = \left(\frac{1}{n_{\mathrm{eff}}}\right)\left(\frac{\delta n_{\mathrm{eff}}}{\delta T}\right)$ is the thermo-optic coefficient and ΔT is the temperature variation experienced by the grating. For silica fibers the thermo-optic coefficient is about $8.6 \times 10^{-6}\,1/°\mathrm{C}$, while the thermal expansion is negligible ($0.55 \times 10^{-6}\,1/°\mathrm{C}$) [70]. Finally, the total wavelength shift can be expressed as:

$$\Delta\lambda_{\mathrm{B}} = \left\{1 - \left(\frac{n_{\mathrm{eff}}^2}{2}\right)\left[p_{12} - \nu\left(p_{11} + p_{12}\right)\right]\right\}\varepsilon\lambda_{\mathrm{B}} + \\ + \left\{\left(\frac{1}{\Lambda}\right)\left(\frac{\delta\Lambda}{\delta T}\right) + \left(\frac{1}{n_{\mathrm{eff}}}\right)\left(\frac{\delta n_{\mathrm{eff}}}{\delta T}\right)\right\}\Delta T\lambda_{\mathrm{B}} \quad (2.7)$$

or, more easily:

$$\Delta\lambda_{\mathrm{B}} = K_{\varepsilon}\cdot\varepsilon + K_{\mathrm{T}}\cdot T \quad (2.8)$$

where K_{ε} is the strain sensitivity (approximately 1 pm/$\mu\varepsilon$), while K_{T} is the temperature sensitivity (about 10 pm/°C). Therefore, it appears evident the importance of discriminating the different contributions in order to selectively measure strain and temperature despite their cross-sensitivity.

2.2 FBGs transmission lines based model

For a uniform grating of length L, the reflectivity at a specific wavelength λ can be analyzed by means of the coupled mode theory [71], which gives:

$$R\left(L,\lambda\right) = \frac{\Omega^2\sinh^2 sL}{\Delta k\sinh^2 sL + s^2\cosh^2 sL} \quad (2.9)$$

where $\Delta k = k - \dfrac{\pi}{\lambda}$ is the detuning wave vector, with $k = \dfrac{2\pi n_0}{\lambda}$ the propagation constant and n_0 the average index in the fiber core, and $s = \sqrt{\Omega^2 - \Delta k^2}$. $\Omega = \dfrac{\pi\Delta n\eta\left(V\right)}{\lambda}$ is the coupling coefficient, where Δn is the amplitude of the refractive index modulation and $\eta\left(V\right)$ is a function of the fiber normalized frequency V, which takes into account the fraction of the fiber mode power contained in the core. This is a closed-form equation that, however, holds only if the sensor is uniform (i.e., uniform spacing between the grating layers and uniform refractive index modulation), which means that it has to be subjected to uniform temperature or strain too, otherwise its properties would be modified in a non-uniform way.

The application discussed in this thesis uses FBGs that are working in highly non-uniform conditions; therefore, a closed-form solution is not possible and another model has to be used. A simple approach is to approximate the propagation of the core mode in the periodic structure forming the grating as that of a TEM wave in a multi-layered structure, in turn, modeled as the cascade of transmission line segments, as sketched in Fig. 2.2 [72, 73, 74].
For each wavelength, the propagation constant and the characteristic impedance of the equivalent transmission line for the i-th layer are:

$$k_{\mathrm{z,i^{th}}} = k_0 n_{\mathrm{i^{th}}} \quad (2.10)$$

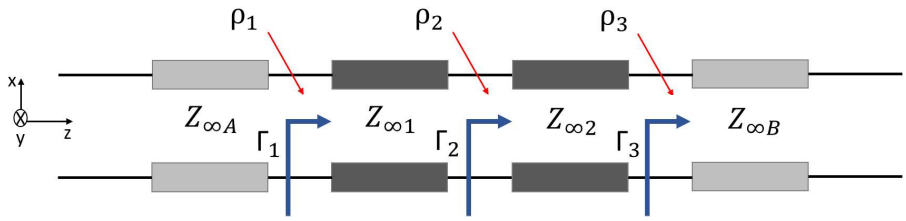

Figure 2.2: Schematization of a four-layer equivalent transmission line structure.

$$Z_{\infty,\mathrm{i^{th}}} = \frac{Z_0}{n_{\mathrm{i^{th}}}} \tag{2.11}$$

where, k_0 is the vacuum wavenumber, Z_0 is the vacuum characteristic impedance (i.e. $\sim 377\,\Omega$), and $n_{\mathrm{i^{th}}}$ is the refractive index of the i-th layer. Then, the Fresnel reflection coefficients ρ_i can be computed at each interface as:

$$\rho_\mathrm{i} = \frac{Z_{\infty,\mathrm{i^{th}}} - Z_{\infty,\mathrm{i^{th}}-1}}{Z_{\infty,\mathrm{i^{th}}} + Z_{\infty,\mathrm{i^{th}}-1}} \tag{2.12}$$

and, finally, it is possible to compute the input reflection coefficient Γ_in starting from the last section and back-propagating the reflection coefficient as:

$$\Gamma_{\mathrm{i^{th}}} = \frac{\rho_{\mathrm{i^{th}}} + \Gamma_{\mathrm{i^{th}}+1} e^{-2jk_{\mathrm{i^{th}}}L_\mathrm{i}}}{1 + \rho_{\mathrm{i^{th}}}\Gamma_{\mathrm{i^{th}}+1} e^{-2jk_{\mathrm{i^{th}}}L_\mathrm{i}}} \tag{2.13}$$

where L_i the length of i-th layer. With this procedure it is possible to easily obtain the grating reflectivity even in non-uniform conditions, changing the properties layer by layer. In particular, it is possible to design different kinds of gratings with various reflectivity values or bandwidth [75]. The reflectivity increases with the number of layers, thus with the grating length and with the refractive index modulation. Usually, commercial gratings are available from 1 mm up to few centimeters: shorter gratings must have higher refractive index changes in order to be strong enough. Typically, a refractive index modulation in the order of 10^{-4} can be obtained by UV exposure. Another parameter that can be tailored, according to the grating length and the refractive index modulation, is the FBGs $\Delta\lambda_\mathrm{FWHM}$, which can be defined as:

$$\Delta\lambda_\mathrm{FWHM} = \lambda_\mathrm{B}\alpha\sqrt{\left(\frac{1}{2}\frac{\Delta n}{n}\right)^2 + \left(\frac{1}{N}\right)^2} \tag{2.14}$$

where α is the grating strength between 0 and 1 (1 for strong gratings) and N is the number of layers. Given this, once the refractive index change is fixed, it is possible to increase the grating length in order to have narrower reflection peaks.

As an example, in Fig. 2.3 are reported the results obtained with transmission lines approach, simulating a standard grating centered at 1549.47 nm. The figure

also shows the response of a commercial grating obtained with the values reported in Tab. 2.1.

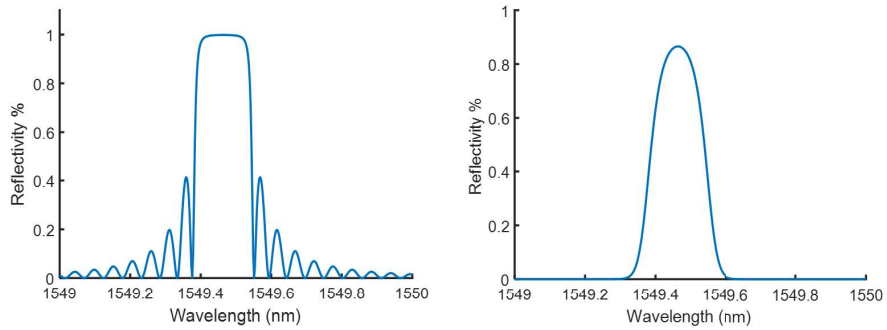

Figure 2.3: Comparison between the reflectivity of a uniform grating and the same grating with apodization applied to avoid secondary lobes.

The difference between the two spectral responses is related to their refractive index modulation, that in the commercial grating is non-constant (called apodized) to avoid the oscillations in the reflectivity that are present in the first case. In the uniform case, the refractive index perturbation can be modeled as:

$$n(z) = n_0 + A(z)\,\Delta n_{\mathrm{ac}}(z)\cos\left(\left(\frac{2\pi}{\Lambda}\right)z + \vartheta(z)\right) + \Delta n_{\mathrm{dc}}(z) \tag{2.15}$$

with n_0 the core refractive index, $A(z)$ the apodization function (equal to 1 in this case), $\Delta n_{\mathrm{ac}}(z)\cos\left(\left(\frac{2\pi}{\Lambda}\right)z + \vartheta(z)\right)$ the alternating part of the perturbation and $\Delta n_{\mathrm{dc}}(z)$ the perturbation offset. In commercial gratings, several apodization profiles are commonly applied, like the Gaussian or the raised cosine. In this thesis, the apodization function applied to the implemented FBG model is [76] $A(z) = \cos^8\left(\frac{2z}{L} - 1\right)$ and the results are shown in Fig. 2.4.

Table 2.1: Values employed for the numerical simulation with transmission lines.

Parameter	Value
n_0	1.4440
Δn_{ac}	$1e-4$
Δn_{dc}	$2e-4$
Λ	536 nm
Layers	54000
Grating length	1.5 cm

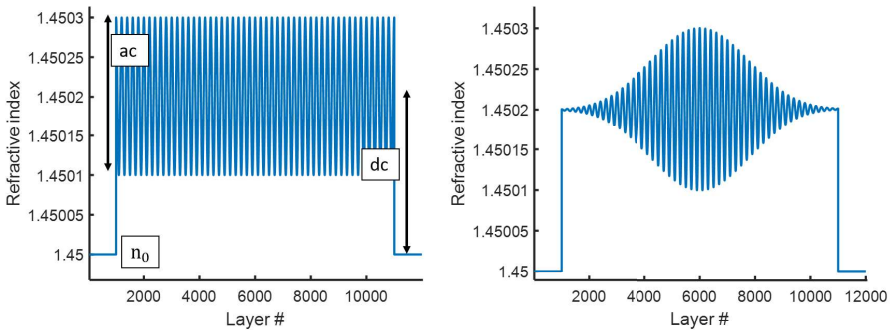

Figure 2.4: Comparison between the refractive index modulation of a uniform FBG (left) and of an apodized one (right). For the sake of clarity in these graph the refractive index has been computed on a small number of layers.

2.3 Typologies

As mentioned in the previous sections, according to the writing technology employed and the application aim, it is possible to obtain a different kind of refractive index patterning that provides as many grating typologies.

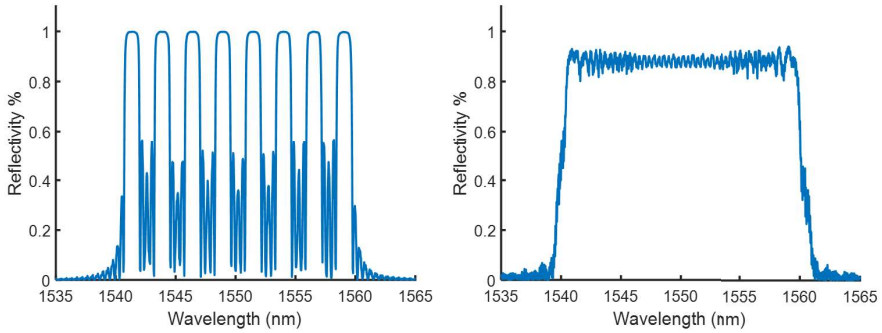

Figure 2.5: Comparison between the spectrum of a 5 uniform (not apodized) FBGs array (left) and a chirped grating (right) obtained from the transmission lines model.

The most widespread and employed type of grating is the uniform one, in which the refractive index modulation is that described by Eq. 2.15, even if, as explained, for many applications an apodization is required. Since many grating manufacturers refer to apodized gratings as uniform, also in this thesis the name uniform is used for apodized gratings although they belong to two different typologies. Moreover, the same uniform grating can be inscribed alone on a fiber or an array of gratings with different central wavelengths can be realized. Depending on the application - thus on the expected maximum temperature and/or strain variation - attention has to be paid in the specification of the array parameters since the various spectral

responses can overlap if the FBG central wavelengths are not spaced enough. The possibility to multiplex the FBGs signal is one of the grating key features that was of great importance in this work. Indeed, since one of the aims is to sense the temperature in several points along the treatment region during an LA, it can be exploited with an array made of short FBGs multiplexed on the same fiber. The extremization of this concept is provided by the chirped grating, where the refractive index is modulated with increasing period. Therefore, in principle, it is a continuous array that can give information on a long region, even if they have been invented for telecommunication applications, such as for dispersion compensation. A comparison between array and chirped FBG spectra is shown in Fig. 2.5, where the transmission line model was employed to obtain these results. Then, other configurations, that were not considered in this work, are [77]:

- *blazed grating*, also known as tilted, because of the perturbation direction that has an angle with respect to the fiber axis. They have been widely employed for the gain-equalization in Er-doped fiber amplifiers, but are currently used for sensing purposes, especially in biochemical applications;
- *superstructure FBGs*, in which a slow spatial modulation is superimposed on rapidly varying refractive index amplitude and pitch modulation; these are currently employed in signal processing and tunable fiber lasers.

Depending on the grating structure and application, a proper interrogation system has to be used to detect FBGs response. The main possibilities are explained in the next section.

2.4 Acquisition system architectures

Most of the information that can be retrieved from FBG sensors is associated with the central peak wavelength position of the reflection spectrum. This gives several advantages in terms of robustness: indeed, if the sensor parameters were related to the intensity of the signal, bending losses would introduce dramatic errors in applications where the fiber is subjected to any movement or has to be handled unless a proper compensation method is employed [78]. In the FBG case, this problem could still occur, but only for curvature angles too narrow, otherwise, as far as the Signal to Noise Ratio (SNR) is enough to detect the peak, it is possible to estimate the central wavelength shift. Another advantage of wavelength encoding method is the possibility to multiplex several grating inscribed on the same fiber and sensing different point, in order to perform a quasi-distributed measurement. In this case, the FBGs have to be appropriately designed in order to avoid any spectra overlapping, since each reflection peak has its central wavelength and they

have to be separated according to the peak width and the expected shift due to the application and the sensor sensitivity.

In order to analyze the FBG reflected spectrum, several methods are available. In this section are described the two most comprehensive solutions [79] that have also been employed in this thesis.

2.4.1 Broadband source and tunable filter

The first possibility to interrogate FBGs is to use a Super-luminescent LED (SLED) or an Amplified Spontaneous Emission (ASE) source to generate a broadband spectrum. Then, light is guided through an optical circulator to the grating and the reflection is acquired by an Optical Spectrum Analyzer (OSA) or a spectrometer (Fig. 2.6).

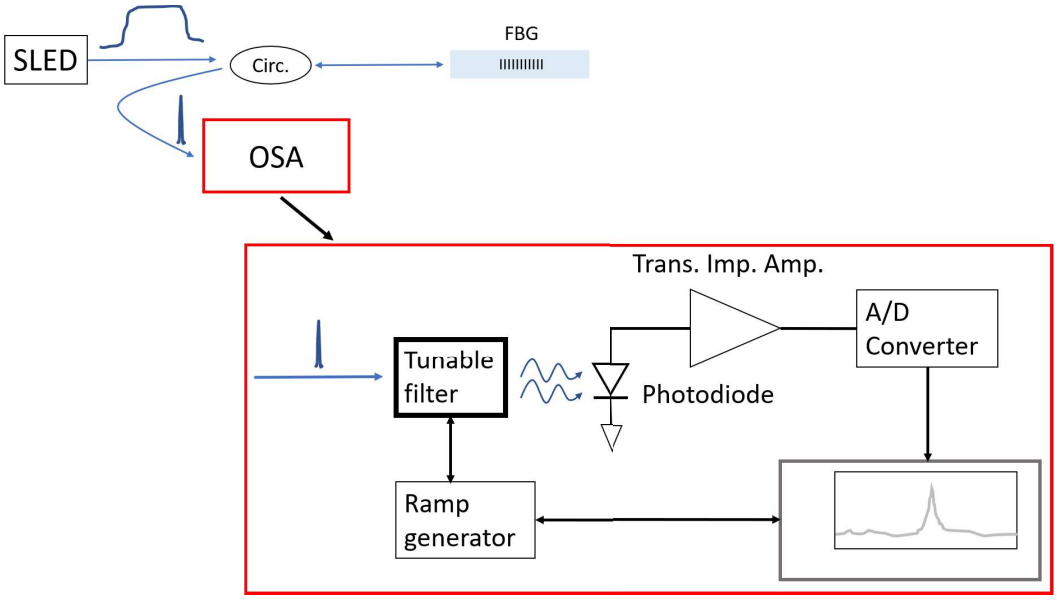

Figure 2.6: Schematic diagram of the FBG interrogation system based on a broadband source and the OSA. In the lower part there is the OSA schematic working principle based on a tunable optical passband filter and a photodiode.

In order to sweep the input spectrum, there are several possibilities, all based on a narrow optical pass-band filter followed by a photodiode connected to a trans-impedance amplifier that converts the current in an analog voltage proportional to the optical power at that wavelength [80]. Then, the amplifier output is converted by an Analog to Digital Converter and displayed/stored. The difference between commercial instruments is the technology that realizes the filter, the most common being:

- Fabry-Perot interferometer (2.7): the input light goes in a cavity composed of two high reflectivity mirrors. The maximum transmission occurs at the cavity resonance and this depends on the distance between the two mirrors; therefore, by changing it, it is possible to scan several wavelengths and measure the received power by the photodiode;

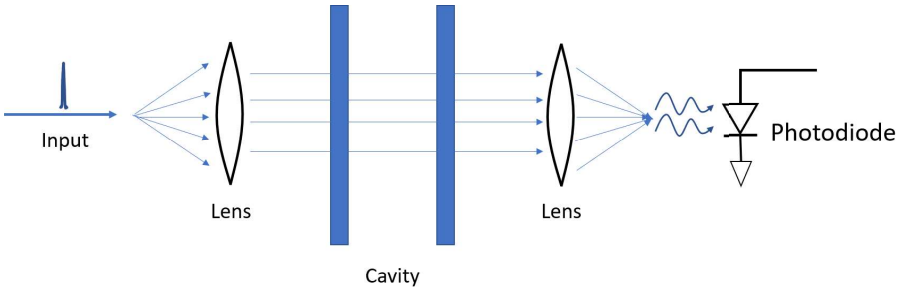

Figure 2.7: Working principle of a Fabry-Perot cavity employed to select the wavelength to be read from the photodiode: the light input is collimated into the cavity and the focused on the photodiode by mean of two lenses.

- Michelson interferometer (2.8): interferometric filter based on the superposition of two waves obtained by decomposing the input beam and have it reflected one from a fixed mirror and the other from a movable mirror. By changing the position of the movable mirror, it is possible to have constructive and destructive interference at different wavelengths.

- diffractive grating (2.9): the input light is collimated by means of a concave mirror on a rotating diffractive grating. The grating diffraction changes according to the angle and therefore can be tuned and focused by a second concave mirror on the photodiode.

All these techniques yield to high wavelength resolution ($\sim 1\,\text{pm}$) and thus are widely employed in lab bench systems. Based on the last possibility, instead of acquiring one wavelength at a time, it is possible to use a Charge Coupled Device (CCD) array, increasing the performance in terms of speed and portability, although at the expenses of the resolution ($\sim 10\,\text{pm}$) and of the SNR. This is the option that has been intensively employed for the experimental part in this thesis, and, even if compared with electrical counterparts the acquisition system is expensive, compared to other optical spectrum analyzer techniques is one of the most cheaper.

2.4.2 Tunable laser

Instead of using a broadband source and filter it, another possibility is to employ a narrowband light source, like a laser, and tune it in order to cover the desired

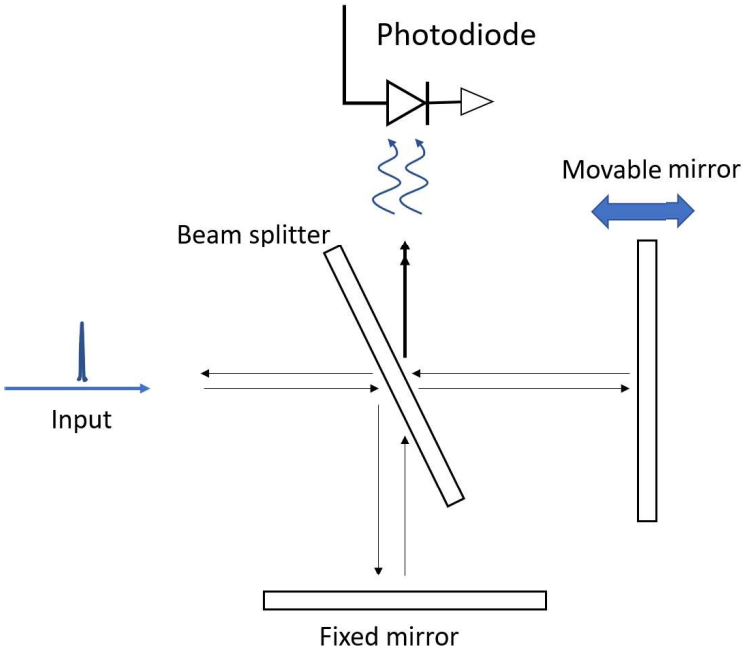

Figure 2.8: Representation of the Michelson interferometer employed as bandpass filter in a OSA.

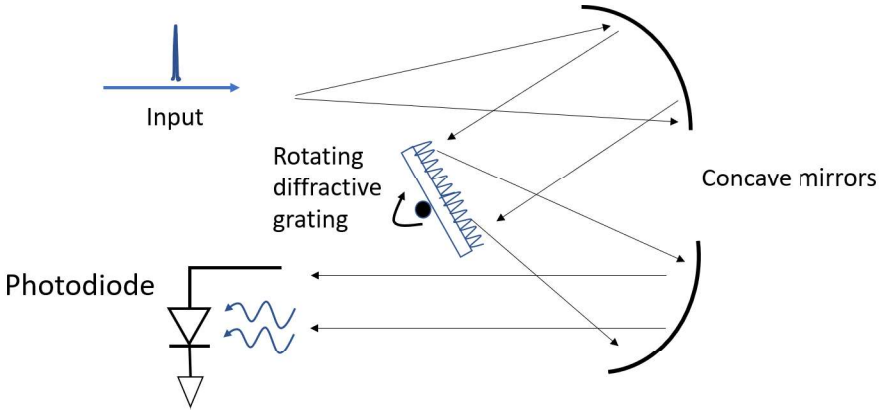

Figure 2.9: Working principle of a diffractive grating based OSA.

wavelength range (Fig. 2.10). In this case, the reflected light by the FBG is directly focused on a photodiode, also in this case with the transimpedance amplifier and the digitalization part.

This system can be cumbersome and not easy to move; therefore, it is employed as bench system and was used in this thesis especially in the FBG characterization part, since its performances allow 1 pm of accuracy and the possibility to acquire up to four channels. Moreover, compared to the diffractive grating system with CCD

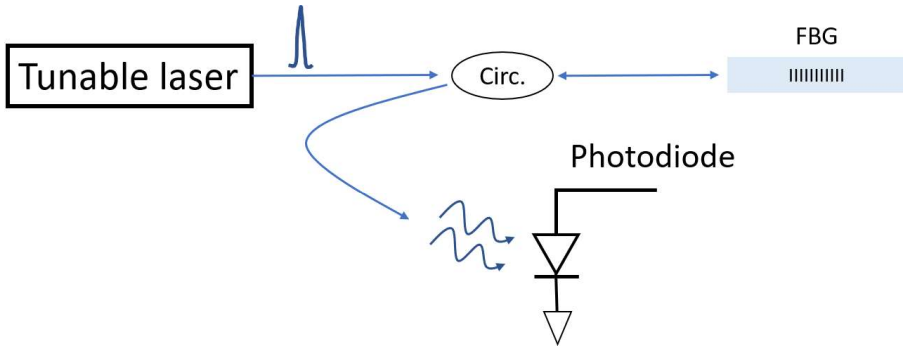

Figure 2.10: Working principle of the interrogation system based on a tunable laser.

the SNR is higher, due to the high power source, and the wavelength range is more extensive (40 nm vs. 100 nm), allowing the multiplexing of several sensors [81].

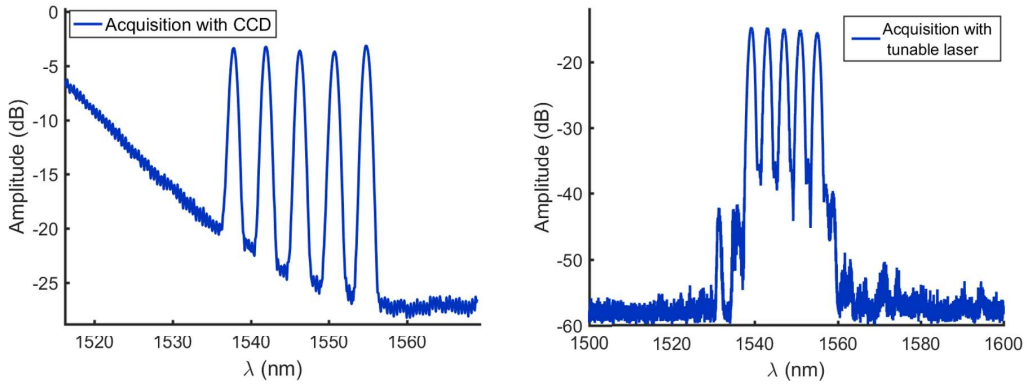

Figure 2.11: Comparison between the acquisition of a 5 FBGs array with a CCD based system (left) and tunable laser based system (right).

An example of this comparison is reported in Fig. 2.11, where the two systems that have been employed in this thesis have been used to acquire the same FBGs array. In the CCD system, the intensity of the 5 FBGs is different, since the SLED source (Exalos 1520-2111) is not flat in the working wavelengths interval (Fig. 2.12). This does not appear for the tunable laser-based system since the laser source always has the same intensity for all the wavelengths that sweeps and this results also in a higher SNR.

2.5 Peak detection algorithm

Mainly when the CCD acquisition system is employed, the wavelength resolution is limited to the array sensing elements density. The system that was intensively used (BaySpec's WaveCapture FBGA Interrogation Analyzer with Volume Phase

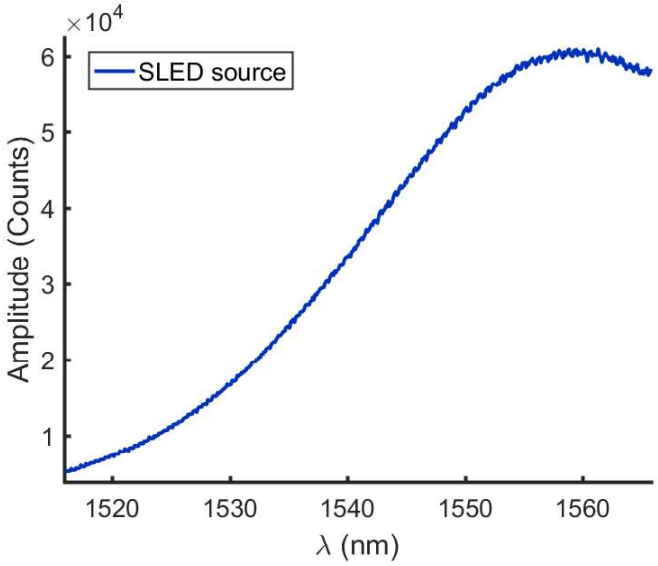

Figure 2.12: Acquisition of the SLED source employed with the CCD system.

Grating VPG®) in this thesis, during experimental tests, has a 512 elements array distributed in a 40 nm wavelength span between 1516 nm to 1569 nm, with a resulting resolution of approximately 100 pm. Considering the typical temperature sensitivity of a silica fiber FBG of 10 pm/°C this will result in a temperature resolution of 10 °C which is absolutely too high considering the application of the LA, where large errors in the temperature estimation can nullify the treatment effect of can provide risks for the patient safety. Therefore, the spectra acquired with the CCD must be in real-time processed in order to increase the resolution to at least 1 °C (i.e. 10 pm), which is reasonable considering the others uncertainty contributions that are discussed in this thesis. In order to do this, several interpolation methods have been proposed in the literature [82, 83], for different applications, according to the expected uncertainty and the acquisition time required. In the case of the LA, a few degrees of errors can be acceptable and the acquisition rate can be between 1 Hz to 10 Hz, therefore not so challenging in terms of processing. A good compromise to fit FBGs spectra was then identified in the least square error method [84] applied between the raw spectra and the objective function y_i:

$$E = \sum_{1}^{N} \left[y_i - f\left(\lambda_i\right) \right]^2 \tag{2.16}$$

where N is the number of acquired points and $f\left(\lambda_i\right)$ the powers at the wavelengths fprovided rom the CCD. In this case, y_i was a Gaussian curve described as:

$$y_i = A \cdot exp\left(-\frac{\left(\lambda_i - \mu\right)^2}{2\sigma^2} \right) + off \tag{2.17}$$

where A is the Gaussian amplitude, μ is the Gaussian mean value, σ^2 the variance and off is an offset value applied to compensate intensity fluctuations.

The algorithm developed in this thesis requires the user to input the nominal central wavelength of each FBG to be tracked. Then, around every central wavelength performs segmentation and then the fitting a small number of points (tens of points for each peak). Once the best fitting Gaussian parameters μ, σ and off have been obtained from an iteration process, they are employed to find the maximum of each peak and therefore its location in wavelength.

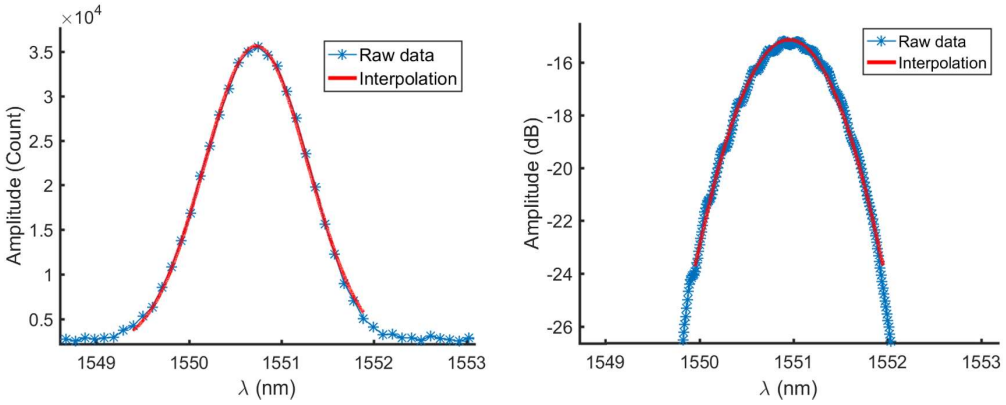

Figure 2.13: Comparison between the Gaussian fitting algorithm applied on spectra obtained from the CCD based system (left) and tunable laser based system (right).

Fig. 2.13 shows the developed fitting algorithm applied to the spectra obtained with the Bayspec system and the Micron Optics system. In particular, since in the first case the points resolution is 100 pm, the fitting has been obtained from 24 points around the peak, while, in the second case, the resolution is 10 pm, and therefore the fitting was applied on 200 points.

Chapter 3

FBGs for temperature measurement

This thesis work aims to develop and study a new fiber optic tool for tumor laser ablation with fiber optic sensing capabilities in order to both deliver the laser at the tumor site and control the temperature reached by the tissues. To this aim, FBG sensors are employed because of their compatibility with the laser radiation and their sensitivity to temperature. Unfortunately, as described in Chapter 2, their central wavelength variation also depends on strain, and strain cannot be controlled during a real ablation where the tissue undergoes coagulation. This problem has been tackled in different ways. For example it is possible to separate strain and temperature using two FBG sensors λ_{B1} and λ_{B2} inscribed in the same fiber with their proper sensitivities ($K_{T_{1,2}}$ and $K_{\varepsilon_{1,2}}$). Since the FBG equations are linear, is possible to write the following system of two equations and two unknowns [85]:

$$\begin{bmatrix} \Delta T \\ \Delta \varepsilon \end{bmatrix} = \frac{1}{D} \begin{bmatrix} K_{\varepsilon_2} & -K_{\varepsilon_1} \\ -K_{T_2} & K_{T_1} \end{bmatrix} = \begin{bmatrix} \Delta \lambda_{B1} \\ \Delta \lambda_{B2} \end{bmatrix} \tag{3.1}$$

where D is the determinant of the matrix, computed as $D = K_{\varepsilon_2} K_{T_1} - (K_{\varepsilon_1} K_{T_2})$. Given this, the more the sensitivities of the two grating are different, the more is possible to discriminate the two quantities T and ε.

This approach is effective but it requires sensors having different sensitivity coefficients, and it is thus not easy to be implemented using commercial devices. The solution investigated in this work takes advantage of a single sensor embedded in a glass capillary. The capillary prevents any strain to be transferred to the FBG. In this way, the sensor becomes only sensitive to the capillary temperature.

3.1 Commercial devices and proposed solution

There are several commercial devices based on the investigated approach:

- *Embodiment for installation* (Fig. 3.1). In this solution, a large embodiment made of stainless steel or Glass Fiber Reinforced Polymer (GFRP) is applied to prevent any strain to the FBG. The applications for these sensors is in the temperature monitoring of large structures, where is possible to weld it on the surface or embed into concrete mix and therefore the robustness in necessary.

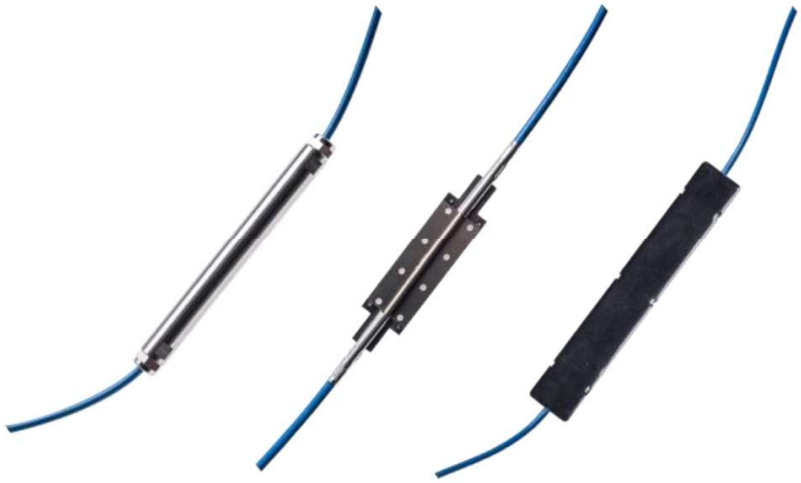

Figure 3.1: Example of the described embedded sensors (*FS63-Temperature sensors, Hottinger Baldwin Messtechnik GmbH*). From left to right: Embedded, Weldable and Composite temperature sensors.

  The main specifications are reported in Fig. 3.2, where it can be seen that the temperature accuracy is low if the proper acquisition system is employed but their dimensions are cumbersome.

- *Metallic probe* (Fig. 3.3). Another devised solution is based on a thin metallic probe that contains one or more sensors, and thus it allows a quasi-distributed temperature mapping (5 mm spacing) to be performed. The reported uncertainty is 0.7 °C which, however, is subordinated to the acquisition system.

  The specifications are reported in Fig 3.4.

- *Dielectric probe.* An interesting solution similar to the one investigated in this thesis' work is a dielectric probe which embeds the FBG (Fig. 3.5). In this case, the probe is less robust and steady during the time but its totally compatible with EM radiation.

  From the technical specifications (Fig. 3.6) is possible to see that this sensor has a lower sensitivity with respect to its metallic embedded counterpart and

Specifications

Sensitivity[1]	33 ºC/nm
Measurement range	-20 to 80 ºC
Resolution[2]	0.1 ºC
Maximum calib. error[3,4]	0.5 ºC
Dimensions	Embedded: 100 x Ø 10 mm Weldable: 45 x 15 x 0.6 mm Composite: 130 x 20 x 6 mm

[1] First order. Typical values.

[2] For 1 pm resolution in wavelength measurement, as found in FS22SI interrogator.

[3] To achieve absolute measurements as presented in this datasheet, an interrogator with an accuracy of at least ±2 pm is required.

[4] Typical traceability uncertainty of ±0.7ºC.

Figure 3.2: Specification*Hottinger Baldwin Messtechnik GmbH Fiber Sensors* for *FS63-Temperature sensors.*

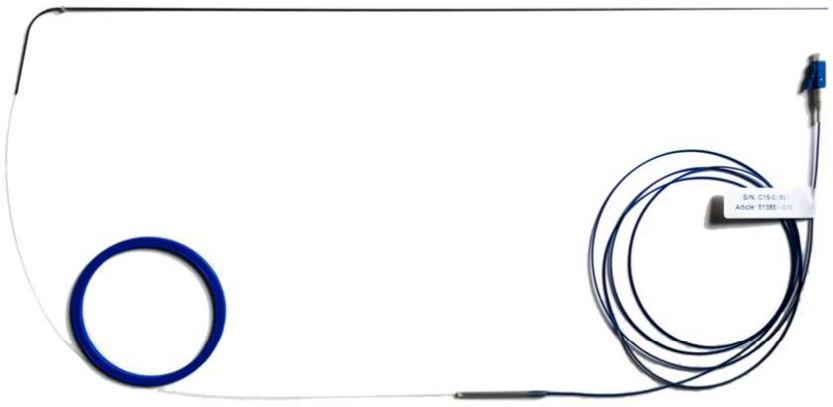

Figure 3.3: *WISTHEAT* thin probe from *PROXIMION AB*©.

a limited temperature range.

In laser ablation the embodiment must guarantee the temperature transfer from the tissue to the sensor and, on the other hand, it has to preserve the advantages of

Physical Properties	Typ	Min	Max	Comment
Number of FBGs per fiber	25	1	100	Max value limited by interrogator BW
FBG length	10 mm	1 mm	10000 mm	Continuous FBG can be up to 10 m
Operating Temperature Range		-45 °C	+250 °C	Standard temperatur range
		-45 °C	+450 °C	Extended temperatur range
		-45 °C	+650 °C	High temperature range
Thermal response	7.5 pm/°C			-50–0 °C
	10.0 pm/°C			0–100 °C
	11.8 pm/°C			100–200 °C
	13.3 pm/°C			200–300 °C
	14.4 pm/°C			300–400 °C
Package diameter	0.8 mm	0.25 mm	2 mm	Hermetic package
	1.5 mm	0.4 mm	6 mm	Non-hermetic package

Figure 3.4: Specifications of *WISTHEAT* temperature probe.

Figure 3.5: *FS63 High Temperature Dielectric Probe, Hottinger Baldwin Messtechnik GmbH.*

the fiber optic probe in terms of compatibility with the laser light and immunity to electromagnetic fields. Therefore, solutions with the metallic embodiment cannot be employed. The commercial dielectric probe of Fig. 3.5 could be a solution but, since in this thesis work the laser light is in direct contact with the probe, the sensor polymer coating could absorb part of the light and then overheat the sensor. For these reasons, in this work, the adopted solution is an IR-transparent quartz glass capillary [86]. The capillary contains the FBG sensor and it is sealed at both ends using epoxy resin(Fig. 3.7).

Specifications

Sensitivity[1]	100 °C/nm
Measurement range[2]	0 to 200 °C
Resolution[4]	0.1 °C
Maximum calib. error[5,6]	1.2 °C
Sensing point	20 mm (from the tip)
Materials	
Sensing Head	Polyimide, PTFE (Teflon®)
Cable	Perforated PTFE/Kevlar cable
Dimensions	Ø 3.0±0.5 mm
Weight	40 g

[1] Typical values.
[2] Temperature on the sensing head and cable

[4] For 1 pm resolution in wavelength measurement, as found in FS22SI interrogator.

[5] To achieve absolute measurements as presented in this datasheet, an interrogator with an accuracy of at least ±2 pm is required.

[6] Typical traceability uncertainty of ±0.5°C.
[7] Limited by the connector.

Figure 3.6: Technical specifications of *FS63 High Temperature Dielectric Probe, Hottinger Baldwin Messtechnik GmbH.*

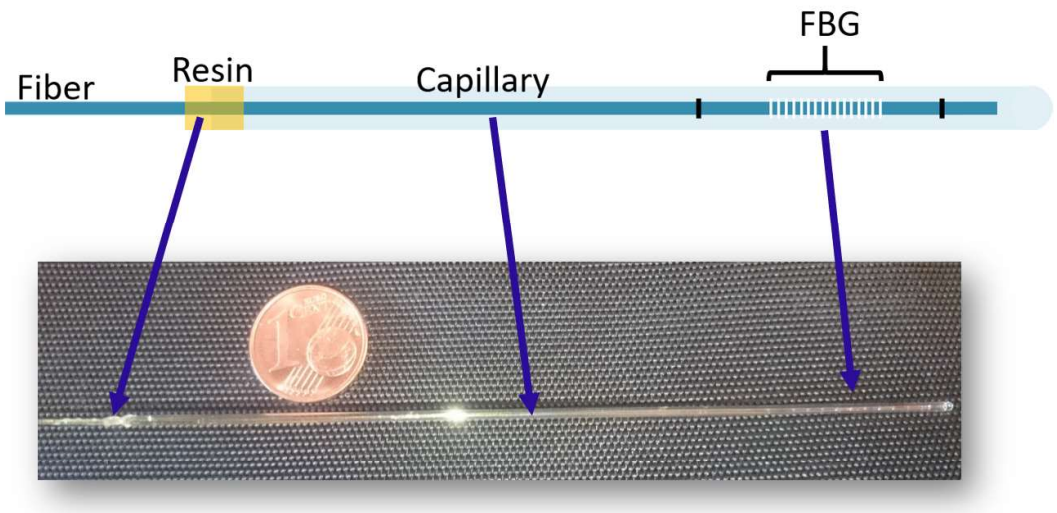

Figure 3.7: Description of a typical FBG probe employed in this thesis, where the single mode fiber containing the FBG takes place inside the quartz glass capillary. The capillary is sealed. This figure was already submitted to [87]

In this way, the FBG is free to expand inside the capillary and its thermal expansion does not introduce any strain, Capillaries made with other materials, such as PTFE, have also been considered. Simulations obtained changing the capillary material as well as the study of the errors induced from such embodiment during temperature measurements are described in Chapter 4.

3.2 Characterization in uniform conditions

A probe having the structure shown in Fig. 3.7 has been arranged and characterized in order to find the relation between the central wavelength shift and the temperature variation. This relation can be written as:

$$\lambda_B = K_T \cdot T + \lambda_0 \tag{3.2}$$

where K_T is the FBG temperature sensitivity in pm/°C and λ_0 is the FBG central wavelength at 0 °C. The procedure was carried out placing the FBGs probes inside a climatic chamber (Vötsch VC 4018) together with a Pt_{100} reference sensor (12 mK standard uncertainty) whose four terminals resistance was acquired by means with a digital multimeter (Agilent 34401A, $6\frac{1}{2}$ digits). In order to guarantee an isothermal setup, the FBGs probes were fixed on the Pt_{100} metallic body with isolating tape. The characterization procedure here described also takes advantage of the interrogation system based on a tunable laser system (Micron Optics). The acquisitions have been made from 0 °C to 80 °C with steps of 10 °C in order to have enough points to verify the sensor linearity in a temperature range similar to the one of a real application. At each step, the instruments reading were taken after that a steady, steady state condition was reached. The FBG spectra were acquired for 30 s at a 10 Hz and the results averaged. This procedure has been employed to characterize all the sensors employed in this thesis work. The results here reported are a characterization example concerning a probe made with an FBGs array of five elements of 1 mm length and spacing of 5 mm.

1. *Raw spectra acquisition with tunable laser system.*

   In this case, the raw spectra acquired at 10 Hz rate for 30 s for each temperature step have been post-processed with a fitting algorithm in order to find the central wavelength shift of each FBG with a better wavelength resolution. The test results are reported in Tab 3.1.

   The linear approximation of the sensor behavior was obtained using the Matlab® polyfit function. Results are reported in Tab. 3.2 where is possible to see that the sensitivity coefficients are close to the FBG nominal value of 10 pm/°C.

   In Fig. 3.8 is reported an example of the linear interpolation of the experimental results concerning the 4^{th} FBG , where the non-linearity error reaches

Table 3.1: Values of the central wavelengths (in nanometers) for a 5 elements FBG array during the characterization process in a climatic chamber. T_{CC} and $T_{Pt_{100}}$ are in Celsius and $R_{Pt_{100}}$ is in Ohm.

T_{CC}	$R_{Pt_{100}}$	$T_{Pt_{100}}$	FBG_1	FBG_2	FBG_3	FBG_4	FBG_5
0.1	100.222	0.568	1539.155	1543.050	1547.080	1550.979	1555.074
10.1	104.137	10.602	1539.265	1543.159	1547.189	1551.065	1555.184
20.2	108.016	20.573	1539.373	1543.267	1547.299	1551.175	1555.294
30.0	111.740	30.173	1539.475	1543.369	1547.403	1551.280	1555.398
40.0	115.616	40.195	1539.572	1543.468	1547.502	1551.381	1555.497
50.1	119.778	51.000	1539.660	1543.555	1547.592	1551.473	1555.585
60.1	124.176	62.434	1539.763	1543.658	1547.695	1551.578	1555.691
70.0	128.621	74.041	1539.883	1543.779	1547.817	1551.701	1555.816
79.8	133.240	86.146	1540.014	1543.911	1547.950	1551.836	1555.951

Table 3.2: Sensitivities and λ_0 coefficients found for the 5 FBGs.

	K_T (pm/°C)	λ_0 (nm)
FBG_1	9.67	1539.172
FBG_2	9.70	1543.066
FBG_3	9.82	1547.095
FBG_4	9.93	1550.971
FBG_5	9.87	1555.089

1.26 °C at 62.4 °C. For all the other sensors the maximum error is up to about 1 °C.

2. *Built-in peak tracking from tunable laser system.*

   The main output of the tunable laser system is the optical spectrum which has been employed to locate the Bragg peak using a fitting algorithm. The system is also able to track the peak position with a built-in function and thus some tests were performed in order to verify the accuracy of the tracking system. The sensors were thus characterized using the peak position directly provided by the interrogation system thus obtaining the results in Tab. 3.3:

   The comparison between the results of Tab. 3.2 and Tab. 3.3 shows a difference in the sensitivity of up to 0.03 pm/°C and a difference of up to 20 pm in the λ_0 value. The sensitivity difference introduces a negligible error but the offset of 20 pm cannot be neglected. As a consequence, the two methods for the peak position measurement cannot be considered interchangeable and thus during the sensor usage the temperature must be obtained processing

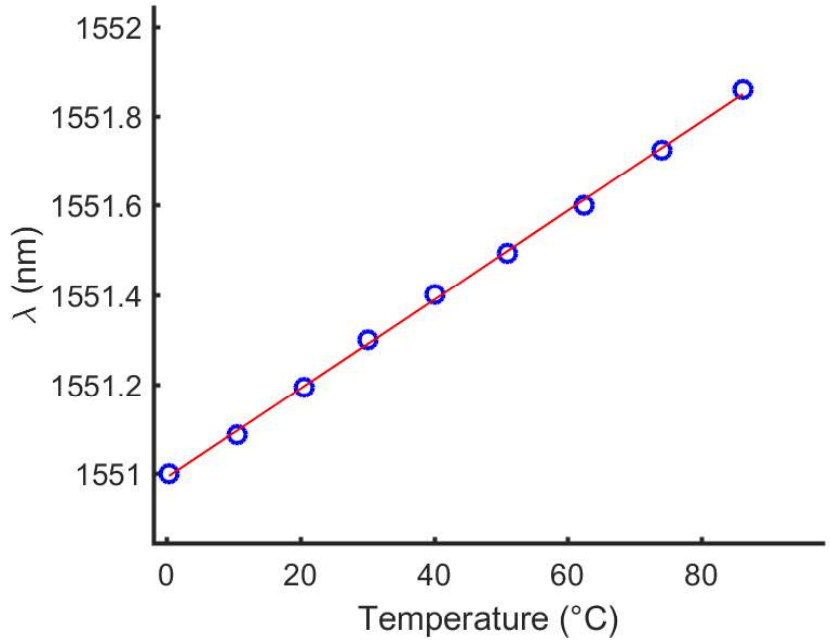

Figure 3.8: Example of linear interpolation of the experimental points for the 4^{th} FBG in the array.

Table 3.3: Sensitivities and λ_0 coefficients found for the 5 FBGs array probe obtained with the built-in peak tracking.

	K_T (pm/°C)	λ_0 (nm)
FBG_1	9.67	1539.188
FBG_2	9.67	1543.060
FBG_3	9.80	1547.098
FBG_4	9.95	1550.991
FBG_5	9.90	1555.080

the peak position obtained with the same method employed to characterize the sensor.

Chapter 4

FBGs behavior in non-uniform temperature distributions

Part of the material presented in this chapter has been already published in [88] (including Fig. 4.2, Fig. 4.3, Fig. 4.5, Fig. 4.6,Fig. 4.7, Fig. 4.8) and in [87] (including Fig. 4.9, Fig. 4.10)

As mentioned in the previous chapter, FBGs are typically employed as temperature and strain sensors in large structures or in the presence of moderate gradients so that both the quantities can be considered uniform along the sensor. During a laser ablation, the temperature must be monitored close to the delivery fiber tip in order to avoid, from one side, the tissue carbonization and, from the other, to ensure the proper treatment to the whole tumor. The sensor must be thus located close to the hot point and, therefore, the FBG will experience a high-temperature gradient because of the low thermal conductivity of organs like the liver. As a consequence, the sensor is exposed to a non-uniform temperature, a condition that is different from the calibration conditions.

Moreover, working in non-uniform conditions, became relevant the knowledge of the grating position along the optical fiber. The position is difficult to know with good accuracy since commercial gratings are expected to work in uniform conditions and therefore their position on the fiber is provided by the manufacturer with several millimeters of uncertainty. The sensor position along the fiber can be measure with high accuracy only with optical techniques such as the OFDR, which, however, is expensive and often not available.

Another relevant aspect is the effect of the sensor embodiment since it can affect the temperature distribution and thus introduce measurement errors. Indeed, it would not affects the measured temperature in uniform conditions, but introduce a systematic error in presence of a gradient. Even in this case, a key role is played by the thermal conductivity of the involved materials.

These aspects will be thoroughly discussed in the following sections.

4.1 Calibration setup for linear temperature distributions

Before to go through the particular case of the temperature gradient given by laser ablation, in order to understand the behavior of FBG under non-uniform temperature conditions, a preliminary study was made on a simplified setup. This setup is devised to reproduce linear temperature distributions, which are useful to locate the position of the grating on the fiber, and, at the same time, it allows to characterize the sensor response to the temperature. This procedure is based on the assumption that under linear temperature distribution the FBG provides the temperature value related to average temperature, as was verified by means of simulations carried out with a transmission line model (Fig. 4.1).

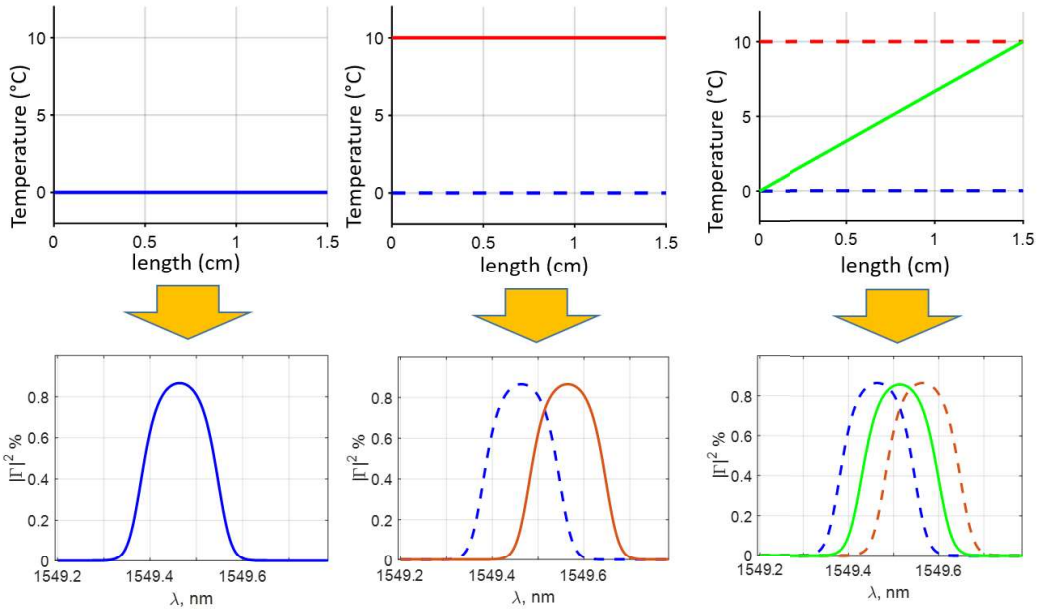

Figure 4.1: Simulations of the behavior of a 1.5 cm length under different temperature distributions: reference (left), uniform (middle) and linear (right).

Figure 4.1 shows the response of a uniform (apodized) grating when its temperature is increased from the reference value of 0 °C (left), to 10 °C (middle) in a uniform way, that is maintaining the temperature constant along the grating length. On the right, the figure shows the FBG spectrum shift when the temperature is not constant and but has a linear spatial distribution. In this case, the peak shifts according to the average temperature, with the same sensitivity found for the uniform temperature, and the spectrum width increases according to the gradient value.

The setup was realized tapering an aluminum bar in order to have a working

region of 4 cm x 1 cm x 2 mm. Along the bar, three equally spaced 0.5 mm holes of 8 mm depth were drilled, 1 cm. Three type-T thermocouples were inserted in the bar holes and eventually fixed with conventional glue (Fig. 4.2). The choice of use thermocouples is due to their small dimension in comparison with other conventional metallic sensors, allowing punctual measurements along the bar.

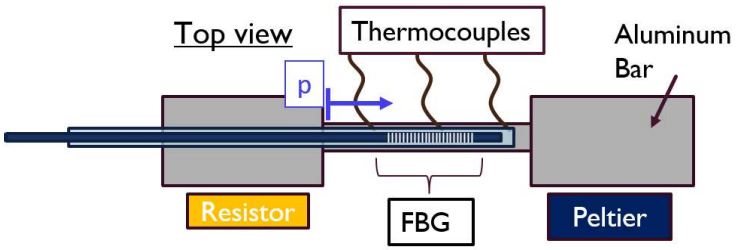

Figure 4.2: Schematic representation of the setup realized for the generation of known linear temperature distributions.

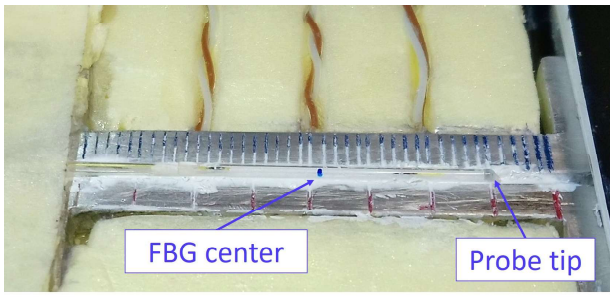

Figure 4.3: Realization of the setup. Blue marks on the bar are 1 mm spaced. The blue spot on the probe represents the FBG center.

The bar was also milled along the most extended direction thus obtaining a groove that accommodates the capillary with the grating. Thermal grease was also employed to ensure a good thermal exchange between the capillary and the bar. Along the groove, several marks were made in order to easily read the grating position on the bar (Fig. 4.3). The thermal gradient was obtained with a resistor fixed on one bar side while the opposite side was cooled with a Peltier mounted on a proper heatsink.

In order to minimize thermal convection, the setup was insulated with expanded polyurethane (Fig. 4.4).

4.1.1 Setup characterization

The characterization aim is to relate the temperatures provided by the thermocouples on the bar with the thermal distribution along it. The temperature along

Figure 4.4: Picture of the setup during its use, where it is insulated to reduce heat dissipation.

the bar is described using a linear model whose parameters, the gradient g and the temperature at the very first position T_0 on the bar, are obtained from the thermocouple measurements using a linear fitting method. The temperature T at any arbitrary position p along the bar can thus be described as:

$$T = g \cdot p + T_0 \tag{4.1}$$

where g and T_0 can be computed with the measurement of the i-th thermocouple T_i in the i-th position p_i as:

$$g = \frac{N \sum_{\mathrm{i}=1}^{\mathrm{N}} p_\mathrm{i} T_\mathrm{i} - \sum_{\mathrm{i}=1}^{\mathrm{N}} p_\mathrm{i} \sum_{\mathrm{i}=1}^{\mathrm{N}} T_\mathrm{i}}{N \sum_{\mathrm{i}=1}^{\mathrm{N}} p_\mathrm{i}^2 - \left(\sum_{\mathrm{i}=1}^{\mathrm{N}} p_\mathrm{i} \right)^2} \tag{4.2}$$

and

$$T_0 = \frac{\sum_{\mathrm{i}=1}^{\mathrm{N}} T_\mathrm{i} \sum_{\mathrm{i}=1}^{\mathrm{N}} p_\mathrm{i}^2 - \sum_{\mathrm{i}=1}^{\mathrm{N}} p_\mathrm{i} \sum_{\mathrm{i}=1}^{\mathrm{N}} (p_\mathrm{i} T_\mathrm{i})}{N \sum_{\mathrm{i}=1}^{\mathrm{N}} p_\mathrm{i}^2 - \left(\sum_{\mathrm{i}=1}^{\mathrm{N}} p_\mathrm{i} \right)^2} \tag{4.3}$$

with $N = 3$ (number of thermocouples employed).

The employed thermocouples were verified in the climatic chamber with the same procedure described in Chapter 3, with respect to the Pt_{100}; their maximum difference with respect to the reference sensor has been found to be 0.2 °C, which can be considered uniformly distributed and, therefore, the associated standard uncertainty is $u_{\mathrm{T_i}} = 0.12\,°\mathrm{C}$. Moreover, the thermocouples have been verified in a fusing ice mixture and their differences were below 0.1 °C, which means that a single verification for all the thermocouples can be performed. The thermocouples signal

is conditioned by a home-made circuit that employs as cold junction sensor an array of two digital sensors with 60 mK of resolution, based on a 24 Σ/Δ converter. The cold junction effect has been considered included in the difference between the thermocouples and the Pt_{100}, during the test presented in this thesis, the cold junction has always operated at room temperature, as during the verification in climatic chamber.

The knowledge of thermocouple position gives another contribution to the uncertainty. Two factors are considered: the location of the hole where the sensor is inserted and the dimension of the hole itself; the former can be considered negligible with respect to the latter, for which a uniform distribution large as the hole width can be assumed, thus obtaining $u_{\mathrm{p_i}} = 0.14\,\mathrm{mm}$.

Afterward, a Monte Carlo method was implemented in order to evaluate the resulting uncertainty associated with the temperatures along the bar T. In the method, the measurements from the sensors were considered with correlation equal to one to avoid any underestimation, and 10000 random samples from uniform distributions were generated. An example of uncertainty value was obtained for the situation with the sensors in nominal positions p =5, 15, 25 mm measuring respectively T =42, 60, 80 °C, which is the situation that occurs when the setup is programmed to provide a gradient of g =−2 °C/mm, where the minus sign is given according to the p increasing direction. From this situation, the simulation provides a mean value for the gradient of $g = 1.9\,^{\circ}\mathrm{C}$ with a coverage interval at 95% equal to 0.4 °C. This value was obtained by subtracting the 2.5 percentile of 1.898 °C to the 97.5 percentile of 1.902 °C of the g distribution. The same procedure was employed to measure T_0, thus obtaining a value of 32.17 °C and a coverage factor at 95% is 0.46 °C, computed as the difference between the 2.5 percentile (31.94 °C) and the 97.5 percentile (32.40 °C).

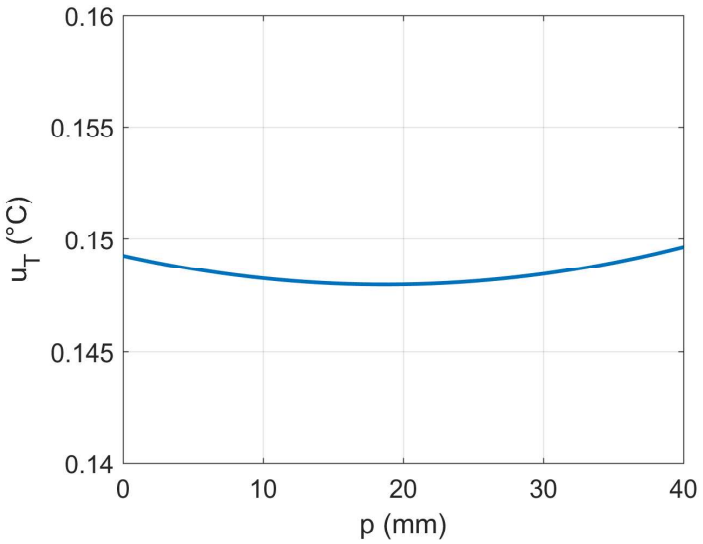

Figure 4.5: Temperature standard uncertainty obtained from the Monte Carlo simulation with $g = -2\,°\mathrm{C/mm}$.

The distributions for g and T_0 were then combined to obtain the temperature T along the bar. In the reported example the resulting standard uncertainty of T can be considered approximately constant for each position on the bar, and it is $0.15\,°\mathrm{C}$ (Fig. 4.5).

Another contribution is related to the temperature linearity. This contribution cannot be estimated with the thermocouples and thus in only three points. To this aim, an IR camera was employed (Fluke®, Ti10) in order to record the temperature along the bar with a spatial resolution of 0.5 mm. The camera cannot be employed to obtain the gradient since its accuracy is not better than the thermocouples. Fig. 4.6 shows an example of a picture taken by the camera when setup was programmed to provide a nominal gradient of $-2\,°\mathrm{C/mm}$.

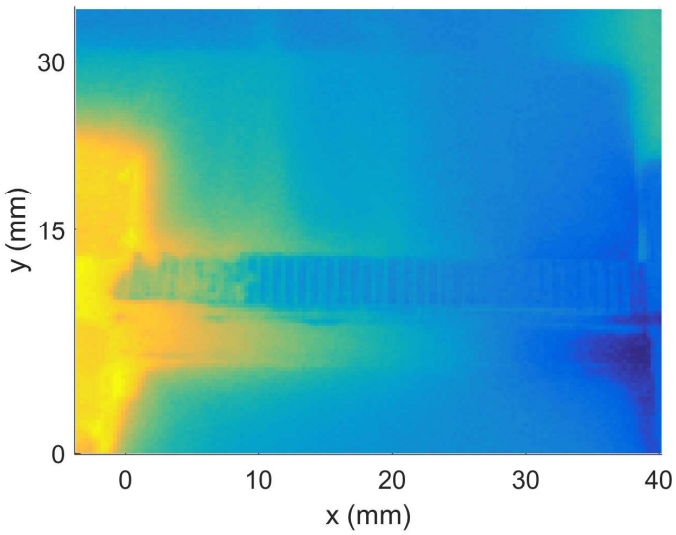

Figure 4.6: IR picture taken from the camera. The lower part of the bar was made opaque in order to better measure the temperature on it.

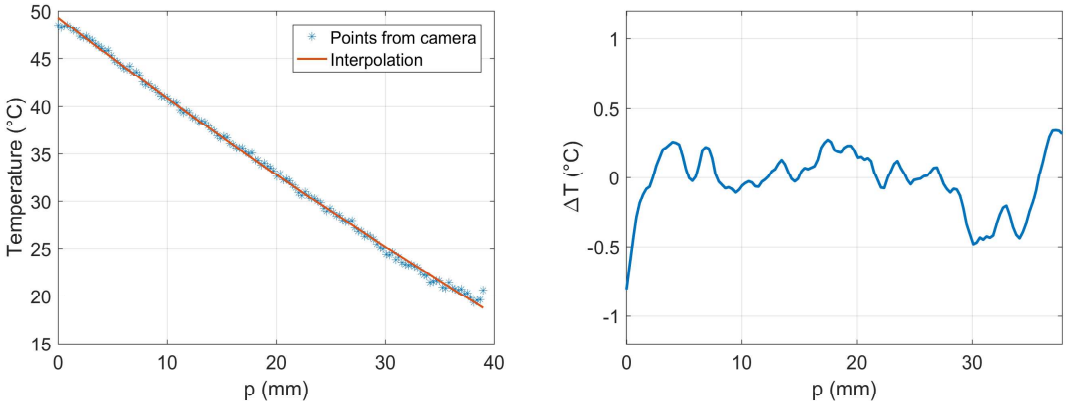

Figure 4.7: Linear interpolation of the IR camera points (left). Error between camera points and the interpolating line (right).

The non-linearity of the distribution was computed along a cut line of the bar covered by matt paint thus obtaining δ_L=0.5 °C. The quadratic sum of the bar uncertainty u_{T} and the non-linearity, assumed as uniformly distributed, yields to:

$$u_{\mathrm{Ttot}} = \sqrt{u_{\mathrm{T}}^2 + \delta_{\mathrm{L}}^2/3} = 0.33\,^{\circ}\mathrm{C} \tag{4.4}$$

This is the standard uncertainty of the temperature along the bar setup. Therefore, this will affect the knowledge of the grating position, as it is explained in the following section.

4.1.2 Measurement of the FBG position

In section is reported the characterization of a commercial FBG (Technica, 90% reflectivity, 0.3 nm FWHM), 1.5 cm long, encapsulated in quartz capillary with inner diameter of 0.8 mm and outer diameter of 1.2 mm. The fiber presents two black marks delimiting a region of 2 cm where the grating is located and therefore results evident the importance to better estimate the grating position in order to use it in the presence of relevant temperature gradients.

The described probe was previously characterized in uniform conditions in a climatic chamber, and its standard uncertainty is $u_{\mathrm{T_{FBG}}} = 0.4\,^{\circ}\mathrm{C}$.

In order to find the grating center, the sensor was placed on the aluminum bar a gradient of about $g = -2\,^{\circ}\mathrm{C/mm}$ was set controlling both the heating resistor and the Peltier cell. The FBG measures the average temperature, that is the temperature of the grating center since the temperature distribution is linear. The grating position p can be thus obtained using Eqn. 4.1 since parameters g and T_0 are known from the thermocouples measurements.

The position p can be located using the marks on the bar. These can be assumed to be 0.5 mm large that results in an associated standard uncertainty of $u_{\mathrm{m}} = 0.14\,\mathrm{mm}$.

Considering a $g = -2\,^{\circ}\mathrm{C/mm}$, this uncertainties can be combined with the setup position uncertainty, yielding an uncertainty of the grating central point position equal to:

$$u_{\mathrm{pFBG}} = \sqrt{u^2_{\mathrm{Ttot}} + u^2_{\mathrm{T_{FBG}}} + u^2_{\mathrm{m}}} = \sqrt{0.16^2 + 0.2^2 + \left(0.25/\sqrt{3}\right)^2} = 0.3\,\mathrm{mm} \qquad (4.5)$$

a value that corresponds to an uncertainty in temperature of 0.6 °C with the programmed gradient. This value is significantly smaller, compared to the one that can be obtained without characterization since the manufacturer provides the grating position with an uncertainty of 5 mm that corresponds to an uncertainty of 10 °C.

In order to verify the obtained result, the characterized FBG was placed again on the setup with the same $g = -2\,^{\circ}\mathrm{C/mm}$. The FBG center was positioned at $p = 20\,\mathrm{mm}$, where there is also the reference thermocouple. The result of this test is reported in (Fig. 4.8), where the grating measurement has a difference of 0.1 °C with respect to the temperature estimated at the same point using the thermocouples.

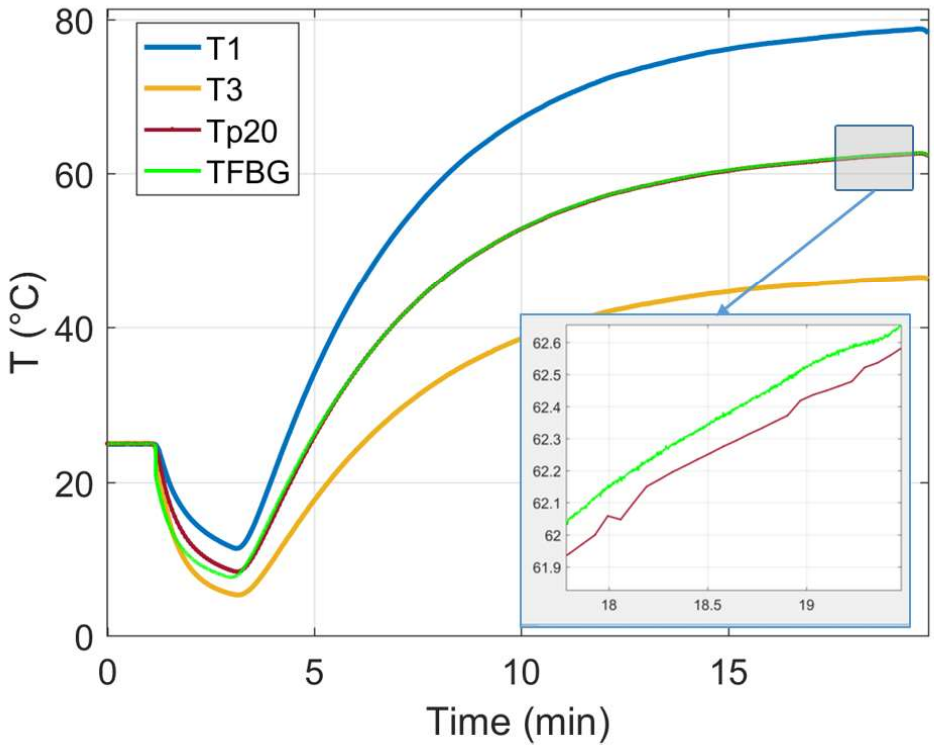

Figure 4.8: Reproducibility test of a characterized FBG. The FBG measurements correspond to the temperature of the central point which is in agreement with the temperature Tp20 obtained with Eqn. 4.1.

4.2 Errors due to the embodiment

This thesis work investigates FBGs as temperature sensors in applications where a rigid sensor embodiment, a capillary, must be employed in order to avoid strain transfer to the sensor. In this chapter, the focus is on the thermal effect of the employed embodiment.

Working with high-temperature gradients, the role of the capillary become relevant. Indeed, probes with a thermal conductivity lower than the surrounding tissue represent a preferential path for the generated heat, resulting in a lower tissue temperature; on the other hand, higher thermal conductivity results in higher tissue temperature. It is therefore important to minimize as much as possible this effect or at least to quantify it. This is what is discussed and analyze in the following sections.

4.2.1 Simulations

In order to quantify the effect on the measured temperature of the employed FBG embodiment and to identify the best one which minimizes the temperature distortion, a Finite Element software has been used to develop a model which is able to simulate the sensor and the tissue under measurement during a laser ablation.

The model simulates both the laser and the heat propagation in the tissue. The propagation of the laser light is modeled using the Lambert-Beer law. Different probes made with different materials are considered inside the liver tissue in order to estimate the temperature at the tumor site with and without the measurement probe. The temperature error given by the sensor presence is therefore obtained.

The Lambert-Beer law, written as:

$$I = \mathrm{e}^{-\mu z} \cdot I_0 \tag{4.6}$$

allows computing the light intensity I in a given position along the propagation direction z, knowing the incident light I_0 and the attenuation coefficient μ. This is an approximation of a real LA since the divergence of the laser beam is not taken into account. The μ coefficient accounts for both the absorption and the scattering of the considered material, liver in this case, and it is responsible for the power produced per length unit inside the tissue.

In order to simplify the 3D simulation, the liver model has been realized with a cylindrical geometry, where the laser light comes from the upper surface of a 20 mm in diameter and 15 mm in height cylinder (Fig. 4.9, left).

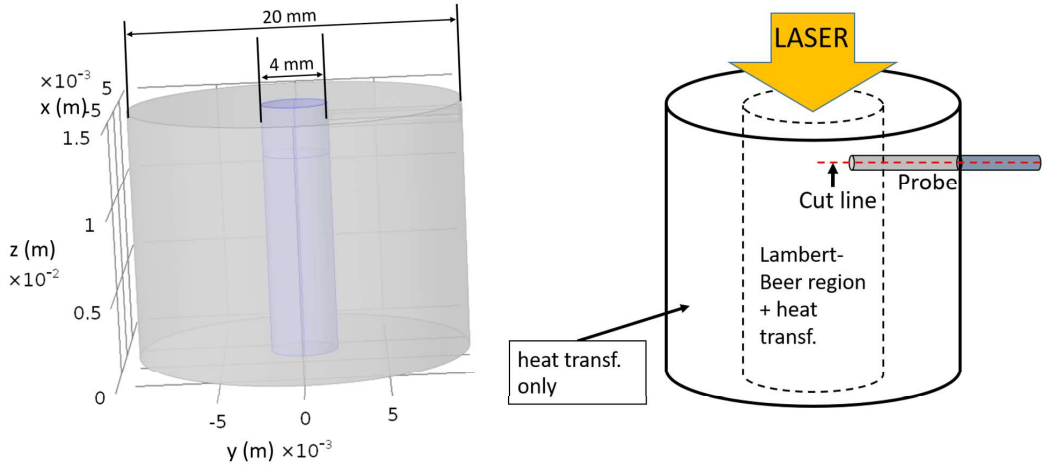

Figure 4.9: Geometry of the studied model (left). Not in scale model scheme where it can be seen the sensor position considered in the simulations (right).

To reduce the computational cost, the laser light is propagated in an inner cylindrical region of 4 mm diameter only, while the heat transfer is computed in

the whole domain. The input intensity was modeled as a Gaussian distribution, considering a delivery optical fiber having diameter of 200 µm:

$$I_0 = P_{\text{in}} \cdot e^{\left[-\left(x^2+y^2/\sigma^2\right)\right]} \tag{4.7}$$

where the input power P_{in} in the domain volume is 1.5 W and the variance of the light distribution on the fiber output surface, σ^2, is 100 µm.

The simulation was computed for a time span of 5 minutes in order to be as close as possible to a real LA procedure (Fig. 4.10). As can be seen, the extension of the ablation region is of about 0.5 cm and it is related to the fiber dimensions. This is one of the drawbacks of the LA, where small diameter fibers are employed, resulting in steep temperature distribution in front of the fiber tip.

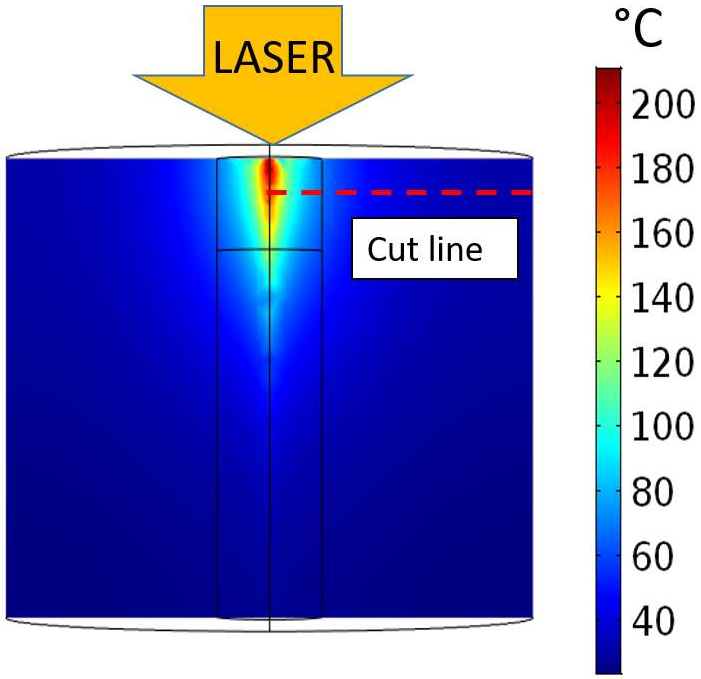

Figure 4.10: Temperature distribution in a inner section. The figure also shows the cut line along which the temperature error was computed.

At the end of the simulation, when the condition can be considered steady, the temperature along the probe longitudinal axis has been taken and compared considering different materials:

- stainless steel, a capillary 1 mm of external diameter, 600 µm internal diameter and with air inside, this emulates a metallic sensor that has been considered only for comparison purposes;

- silica glass, a fiber of 200 µm in diameter, this probe is useful to study the effect of a bare FBG without embodiment;
- silica glass bare FBG (200 µm) inside a quartz glass capillary with 1 mm of external diameter, 600 µm internal diameter and with air at the interspace;
- silica glass bare FBG (200 µm) inside a PTFE capillary with 1 mm of external diameter, 600 µm internal diameter and with air at the interspace.

The probes have been placed close to the delivery fiber tip (1 mm), just outside the region where Lambert-Beer law is computed, and the temperature along their longitudinal axis was recorded at the end of the simulation (Fig. 4.9, right).

In order to study the effect of the thermal load of the probes, their light absorption was not taken into account in these simulations. This means that the temperature distribution inside the liver tissue is modified only by the different material thermal conductivity and not from their optical properties. The error given by each probe was obtained as the difference between the temperature along the sensor and the temperature in the same region where there is the liver tissue only. The results are reported in (Fig. 4.11), where it can be seen that the larger error is obtained for each probe at the fiber tip and then it quickly decreases and becomes negligible after a few millimeters.

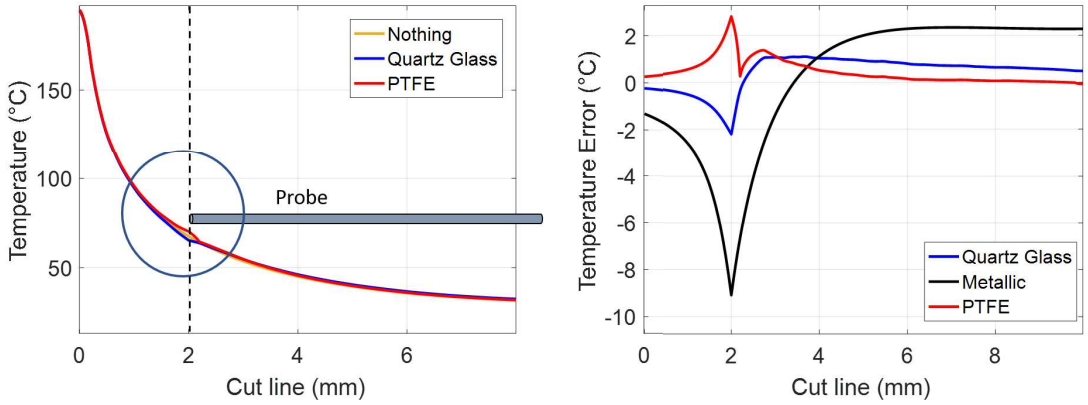

Figure 4.11: Temperature error given by different simulated probes. On the left can be seen the probe and the temperature distribution taken along the cut line, while on the right is reported the error with respect to the temperature distribution without probe.

As expected, the highest error is related to the metallic sensors since it has the most significant thermal conductivity with respect to the surrounding tissue. In this case, at the sensor tip, the error is of −16 °C, that is, the metallic sensor cools the treatment region. After a couple of millimeters, the error changes sign

and becomes positive, settling at 6.5 °C. This behavior is due to the heat that propagates into the probes, increasing its temperature. The same kind of pattern, with different values, can be found for materials with a thermal conductivity higher than the liver, as can be seen for the bare silica fiber and the silica fiber embedded in the glass capillary. In the last simulation, the error is of −3 °C at the probe tip and becomes 1 °C after 2 mm. In case of an insulating material like PTFE, the simulations return an opposite behavior. The error at the sensor tip is 2.2 °C but it decreases and nullifies after few millimeters because of the compensation between the PTFE insulation and the glass conduction of the inner fiber.

4.2.2 Experimental validation using a simplified setup

The simulation results cannot be validated during a real ablation since it is not possible to know the temperature inside the liver without using any sensor. For this reason, in order the experimentally assess the simulation results, a setup has been arranged in order to compare different probes. The setup represents a simplified version of the model shown in Fig. 4.9 but it allows the probe comparison to be carried out in controlled and reproducible conditions.

The setup is composed of a rectangular block of liver phantom made with agar jelly heated from one side with a resistor. A metallic bar distributes the resistor heat on the phantom surface. In this way, an almost uniform thermal gradient will be generated along the phantom.

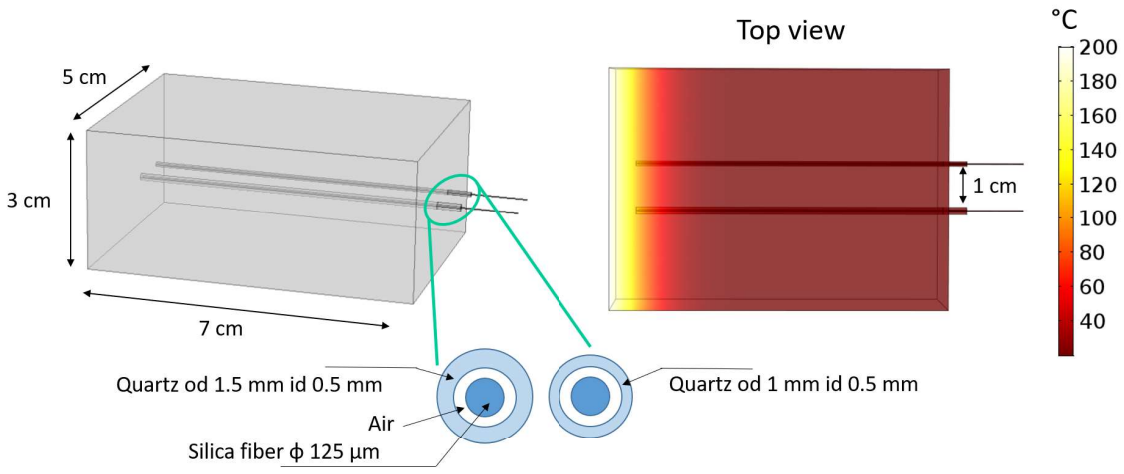

Figure 4.12: Scheme of the simplified setup (left); simulations results: temperature distribution in the liver block (right).

Two probes with different characteristics were employed and compared:

- a silica glass fiber of 125 µm in diameter, with 5 FBGs inscribed (1 mm each,

5 mm spaced), inside a quartz glass capillary with 1 mm of external diameter, 500 µm internal diameter and with air at the interspace;

- a silica glass fiber of 125 µm in diameter, with 5 FBGs inscribed (1.5 mm each, 5 mm spaced), inside a quartz glass capillary with 1 mm of external diameter, 500 µm internal diameter and with air at the interspace;

so, basically, the probes have the same structure but different capillary wall thickness (Fig. 4.12).

The setup behavior was firstly simulated from a thermal point of view. The temperature distributions obtained with the simulations are reported in (Fig. 4.13) where is possible to see that the temperature of the probe area that contains the first two FBGs, that is the area in close contact with the ablation region and thus the most important, is higher when the probes are employed.

Moreover, what it is important to notice is that a higher temperature corresponds to a larger capillary, due to the higher thermal conductivity of the probe with respect to the surrounding tissue (see Tab. 4.1).

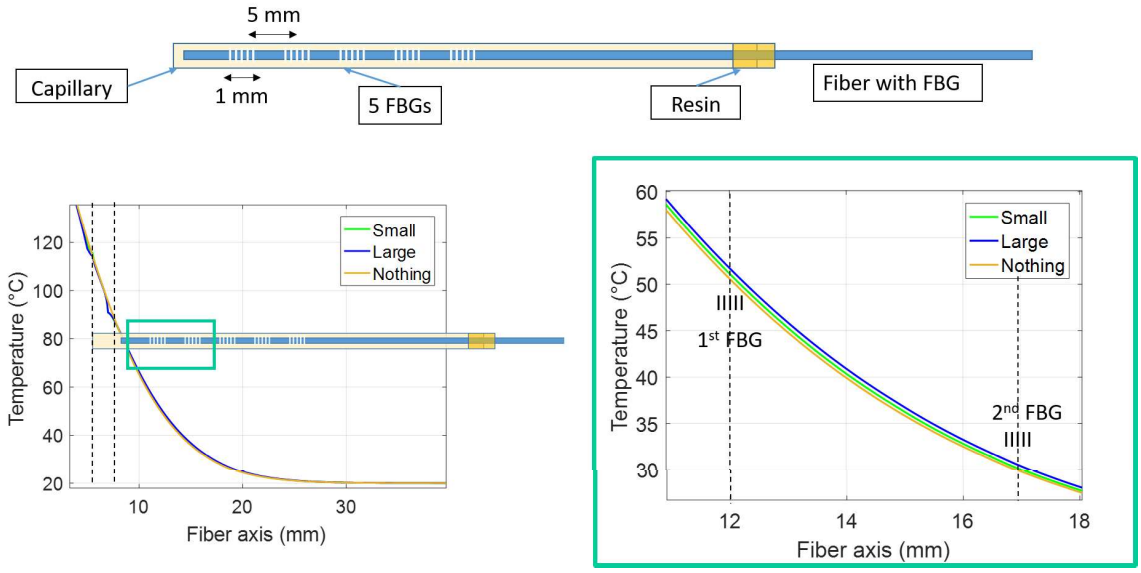

Figure 4.13: Scheme of the FBG probe employed (top); temperature distribution inside the probe (bottom left) and magnification (bottom right).

The setup was that arranged and the probes were inserted as described in the simulations. One of the main issues is the control of the probe position inside the phantom block. Working with high gradients, such as 3 °C/mm, each millimeter of error in the position corresponds to 3 °C error in the temperature estimation. For this reason, a liver phantom made with a solution of 5% w/v agar in water was employed. This has, nominally, the same thermal conductivity as the liver, in a

Table 4.1: Thermal conductivity of materials employed in the simulations.

Material	Thermal conductivity (W/mK)
Swine liver [89]	0.54
Silica glass [90]	1.38
Quartz glass [90]	1.40
Agar gel (@60 °C) [91]	0.55
Air [90]	0.03
Copper [90]	400

temperature from 55 °C to 60 °C [92, 93, 94], but it is almost transparent, allowing an accurate probe positioning to be performed. In any case, the real phantom thermal conductivity and capacitance are known with a large uncertainty and thus the setup can only approximate the simulation results. Nevertheless, the gradient is pretty uniform along the phantom main axis and thus the setup can be employed to compare different probes since they will experience the same gradient.

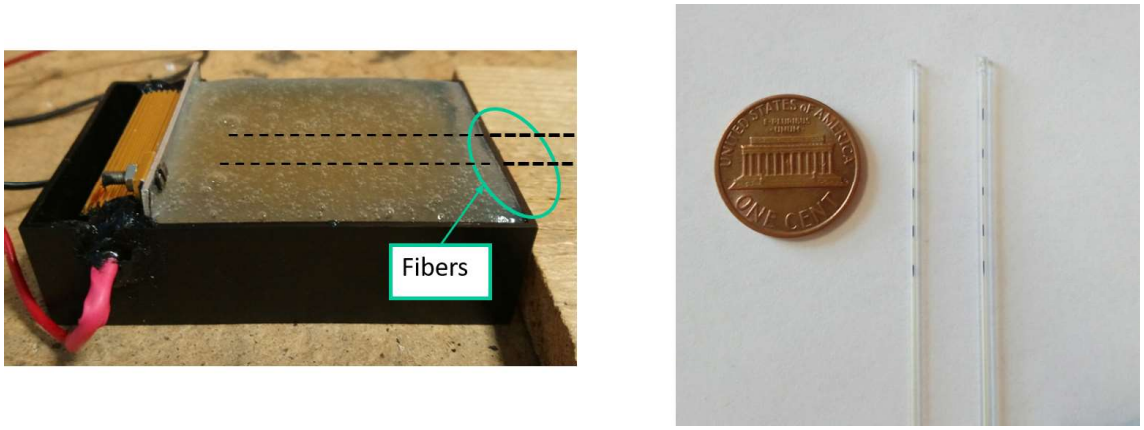

Figure 4.14: Realization of the agar setup with the hot plate on the left side (left); example of FBGs probes with different capillaries thickness employed (right).

During the test, the setup was covered with a polyurethane box in order to achieve a high-temperature gradient. The heater was turned on and after one hour the thermal transient finished and the temperature measured using the FBGs (Fig. 4.15).

As can be seen, the temperature along the thicker probe is up to 1.5 °C higher. This result is in agreement with the simulations because the quartz glass probe represents a preferential path for the heat flux with respect to the tissue.

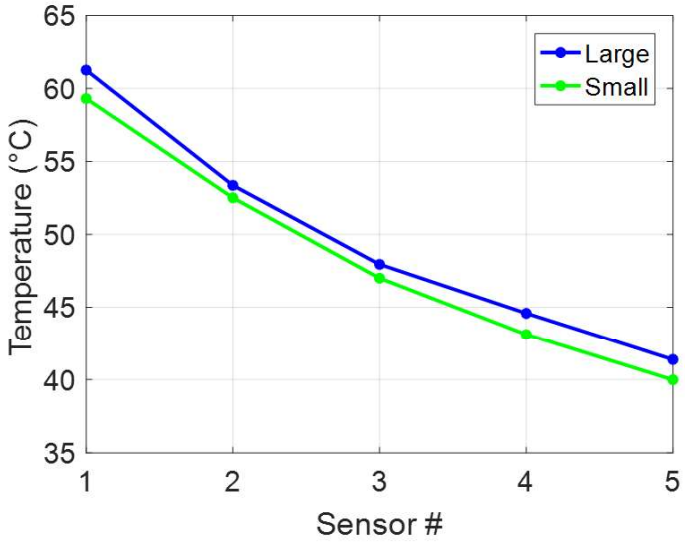

Figure 4.15: Temperature measured by different FBG probes in agar. Each probe has 5 FBGs and the one labeled as 1 is towards the probe tip

Chapter 5

All-fiber optic probe development and characterization

Part of the material presented in this chapter has been already published in [95] (including Fig. 5.6 (left), Fig. 5.7 (left), Fig. 5.14, Fig. 5.15), in [96] (including Fig. 5.18, Fig. 5.19), or submitted to to IEEE Transactions on Instrumentation & Measurement with a work entitled "Temperature Monitoring with Fiber Bragg Grating Sensors in Non-Uniform Conditions" (including Fig. 5.5 and Fig. 5.10).

In the previous chapters, FBGs have been investigated as temperature sensors for LA monitoring and issues related to the non-uniform temperature distribution along the sensor, as well as the load effect of the sensor embodiment, have been addressed and quantified. In a real application, further problems arise since the laser-delivery fiber and sensor probe positioning can be very difficult because of the significant uncertainties related to the imaging systems employed to monitor the positioning. As a consequence, large temperature errors due to the measurement in the incorrect position lead to a misunderstanding of the treatment status. Moreover, it has to be taken into account that LA should be a minimally-invasive therapy and, therefore, the fewer insertions have to be performed, the less invasive the treatment is.

Part of the thesis work was thus devoted to the development and the test of a single probe that embeds both the laser delivery fiber and the sensing fiber. The probe structure and some details regarding the manufacturing of delivery fiber are described in the following sections.

5.1 Probe realization

As mentioned before, a single probe that combines both the FBGs and the delivery fiber presents several advantages, since it is less invasive and guarantee the proper FBG position with respect to the laser source. In this section, are described

two different solutions devised to integrate the FBGs into the probe. In both cases, the delivery fiber has been modified in order to shape the radiation pattern to the tumor shape.

5.1.1 Delivery fiber modification

One potential issue of the LA is given by the optical power distribution at the delivery fiber tip. Indeed, since the light is emitted from a small surface (the fiber core, about 0.03 mm^2) the power density on the tissue is very high and carbonization can easily occur even at low power levels [97]. Carbonized tissues prevent the laser radiation to penetrate into the remaining part of the tumor (Fig. 5.1) and, therefore, it should be avoided. A solution would be to decrease the power to very low levels, but this would result in a very long treatment time.

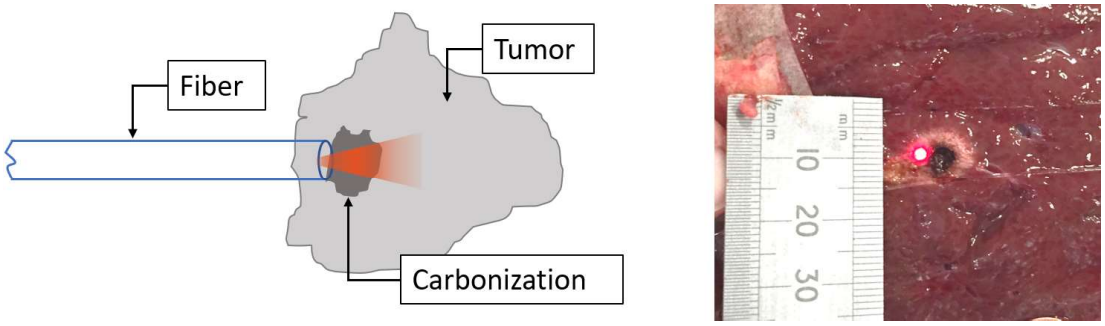

Figure 5.1: Sketch of a flat tip fiber treating a tumor (left). Example of a test conducted with a flat tip fiber on pig ex-vivo liver where there was not the tumor. It is easy to see the carbonization produced and the small ablation area (right).

For this reasons, the thesis aim was then not only to study FBGs behavior for monitoring LA treatments but also to improve the laser-delivery from the fiber in terms of ablation size and effectiveness. To this aim, different solutions have been investigated by several researchers, such as adding a lens at the fiber tip [98]. The approach studied in this thesis work does not require any additional optical component because one of the requirements is, also, to minimize to the size of the probe. The investigated solution relies on a modification of the fiber cladding in order to allow a lateral emission of the light [99]. Part of the cladding is removed so the light will be diffused in the whole damaged region, thus decreasing the power density and preventing carbonization; moreover, the damaging size and severity can be easily modified in order to tailor the optical power distribution to the tumor shape and dimension. The damages have been performed by mean of a CO_2 laser that can be absorbed from the outer cladding of a 400 µm fiber; the outcome of this procedure are small cuts from where the light goes out (Fig. 5.2).

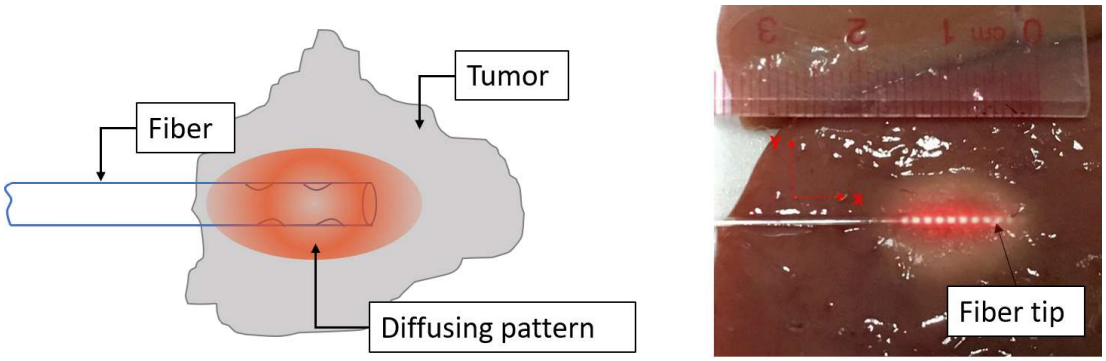

Figure 5.2: Sketch of a diffusing fiber treating a tumor (left). Example of a test conducted with diffusing fiber on pig ex-vivo liver where there was not the tumor. No carbonization occurs in this case and the ablation area is larger (right).

The emitting fiber modification also provides advantages from the sensor side: it is now possible to aggregate, without increasing the probe size, the delivery fiber with the sensing fiber, and the sensor can be located inside the hot spot in order to measure the maximum temperature. The probe that embeds the fibers in a single embodiment presents the following advantages:

1. only one, even if slightly bigger, insertion has to be done on the patient;
2. the relative position between the light source and the sensors is known (i.e. no positioning errors);
3. if the ablation pattern is symmetric, by measuring along the fiber axis is possible to retrieve the whole temperature distribution in the tumor.

The aspects related to the development and the characterization of an all-glass fiber probe for tumors laser ablation are discussed in the next sections.

5.1.2 Single probe for Laser Ablation

Different probe structures can be devised in order to minimize the dimension and to simplify the probe usage. The simplest solution is composed of two different fibers, the delivery one and the sensing one, placed together into the same capillary, fixed with optical resin at one side (Fig. 5.3). This solution is the most cheaper and flexible and has been widely employed in the experiment described in the following.

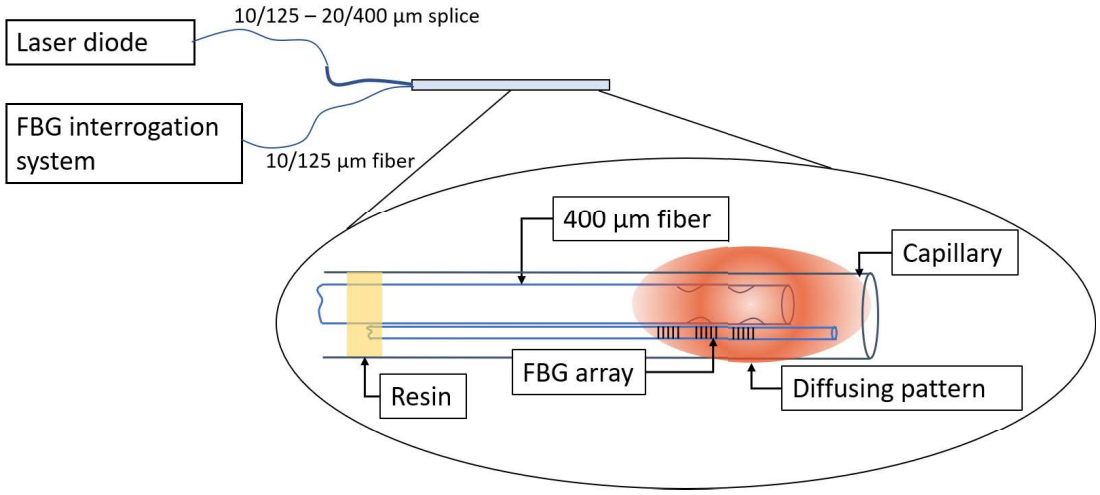

Figure 5.3: System employed with the two-fiber solution.

The second adopted solution is more complex and expensive but allows an even smaller probe realization. In this case, the employed fiber is a 20/400/440 µm Double Cladding (DC) fiber where the core has been modified inscribed a cascade of FBGs. In this, the laser is delivered through the inner cladding and the core acts as a temperature sensor. The laser light is launched into the cladding using an optical coupler that combines the laser light and the sensing signal (Fig. 5.4).

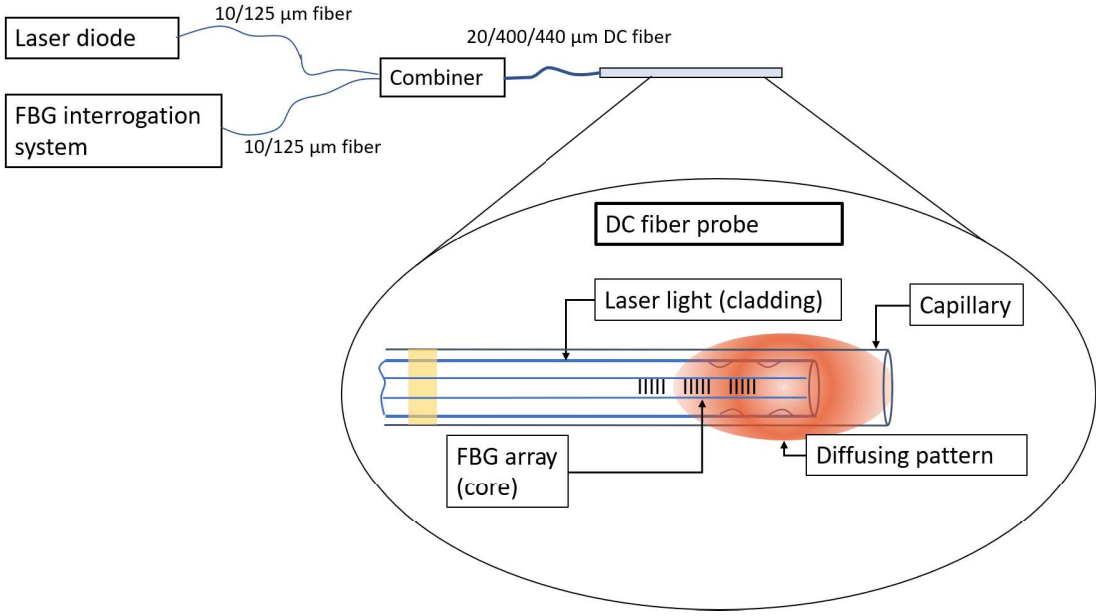

Figure 5.4: Probe based on a double cladding (DC) fiber.

In the following sections, the characterization of both the solutions will be described and measurements errors provided by the embedded FBGs will be analyzed, while in the next chapter experimental results concerning the probe application are presented.

5.2 Temperature distribution in liver phantom

So far, simulated temperature distributions were employed to study the FBGs behavior under non-uniform temperature conditions.

In this section are reported procedures and results concerning the monitoring of the temperature distribution that occurs in real applications. To do this, it is useful both to assess the radiation distribution of the proposed probe and to assess the measurement capability of the investigated temperature sensors.

To this aim, a modified version of the agar gel already presented was used. Indeed, in this case, it is important to mimic not only the liver thermal conductivity but also the optical absorption. The gel was, thus, loaded during the preparation with Indian ink [100, 101, 102]. Then, the gel was left solidify in cylindrical molds having height 0.5 cm and diameter 9 cm. The final phantom was composed of three layers so that the laser fiber can be easily inserted the middle of the phantom (Fig. 5.5 (right).

The fiber delivering the laser was, then, inserted in the inner agar layer inside a quartz capillary in order to heat the phantom central part. Tests were done to compare the radiation pattern of modified and non-modified fibers. A non-modified 400 µm flat tip fiber was used first, then the same fiber was modified and the test repeated. The laser power was set to 2 W and the temperature at the upper, external, surface of the agar pile was monitored using an IR camera. After 5 minutes the temperature was steady and then the upper agar disk was quickly removed thus exposing the delivery fiber and internal part of the phantom. The temperature distribution was immediately recorded with the camera thus obtaining the result of Fig. 5.6. Qualitatively, it is easy to see that the phantom temperature increase is more extensive for the diffusing fiber.

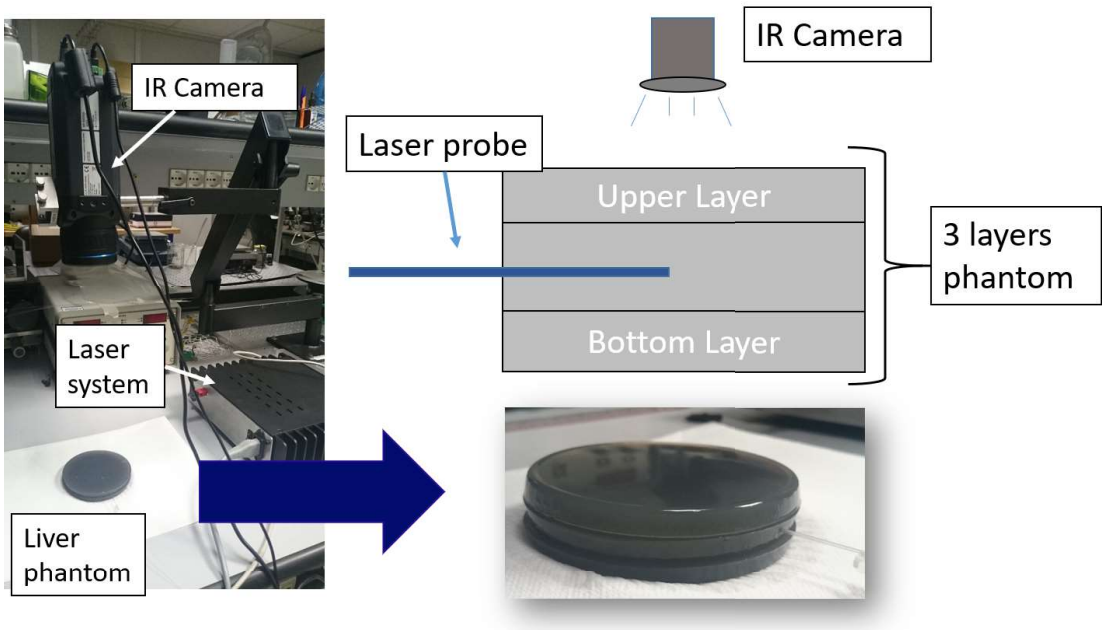

Figure 5.5: Employed setup for the LA temperature distribution, with the laser, the IR-camera and the liver phantom (left); sketch of the setup where the three layers phantom has the laser delivery fiber inside and the IR-camera above (right).

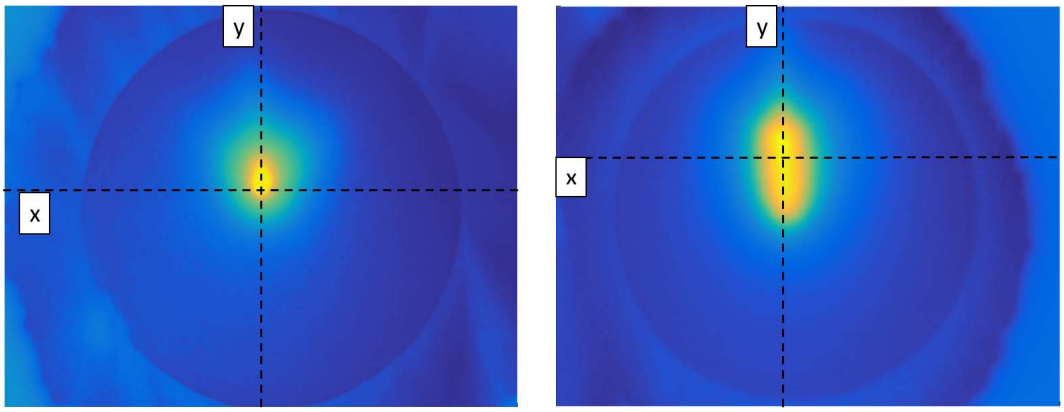

Figure 5.6: Inner layer thermal image taken during the experiments of a 400 µm flat tip fiber (left) and of the diffusive fiber (right).

The thermal distribution along the delivery fiber axis is shown in Fig. 5.7(left) where is possible to quantitative compare the temperature distributions obtained with the two fibers. For the non-modified fiber, the temperature reaches 60 °C, but the distribution presents a very narrow peak with gradients up to 2 °C/mm. The modified fiber, instead, presents a smaller peak temperature and an approximately flat temperature distribution around the radiating area.

This result shows that the modified fiber is the best candidate to be employed in a probe for laser ablation.

The test also shows that the temperature barely reaches cytotoxic levels, but is possible to tune the laser power and thus scale up the power distribution to the desired values.

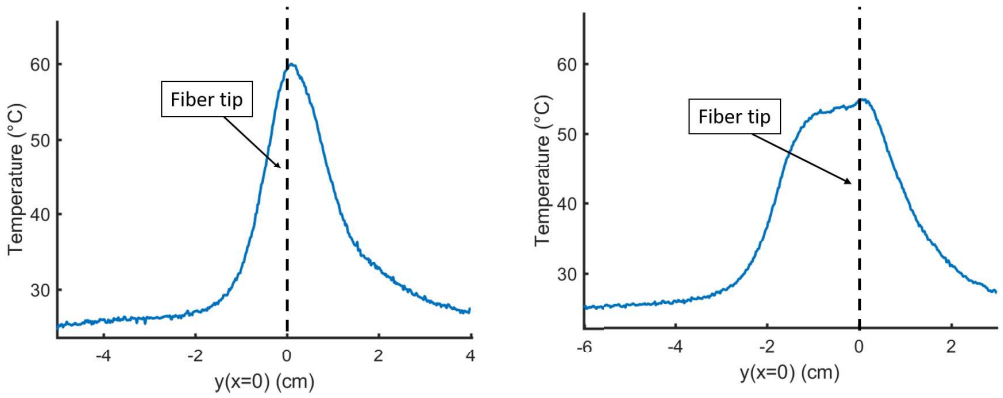

Figure 5.7: Comparison between the temperature distributions obtained during the tests on liver phantom with a flat tip fiber (left) and the diffusing fiber (right). At y=0 is positioned the fiber tip.

The shape of the temperature distribution in Fig.s 5.7 severely constraints the FBG measurements. The temperature gradient is as large as 2 °C mm so, as shown in the previous chapter, any error in the sensor position significantly affects the temperature measurements. Moreover, the FBG works in a region where the temperature distribution is non-linear, thus resulting in further uncertainty contribution, as discussed in the following section.

5.2.1 Errors due to FBGs length

The particular case of linear temperature distribution, studied in the previous chapter, has shown that the FBG returns the average of the temperature along its sensitive area. The response in the presence of a non-linear distribution has been analyzed using the FBG model based on the transmission lines which has been applied on a particular distribution recorded with the IR camera.

The simulation was based on a standard 1.5 cm that slides on the temperature distribution, providing the FBG response at different positions.

The temperature error was obtained as the difference between the measured temperature and the average temperature in the grating area (Fig. 5.8).
As can be seen, larger errors correspond to more substantial non-linearity in the temperature pattern and, in particular, the maximum error registered is of 3 °C in ($y = -1.5$). In the region of uniform radiation, that is in the middle of the

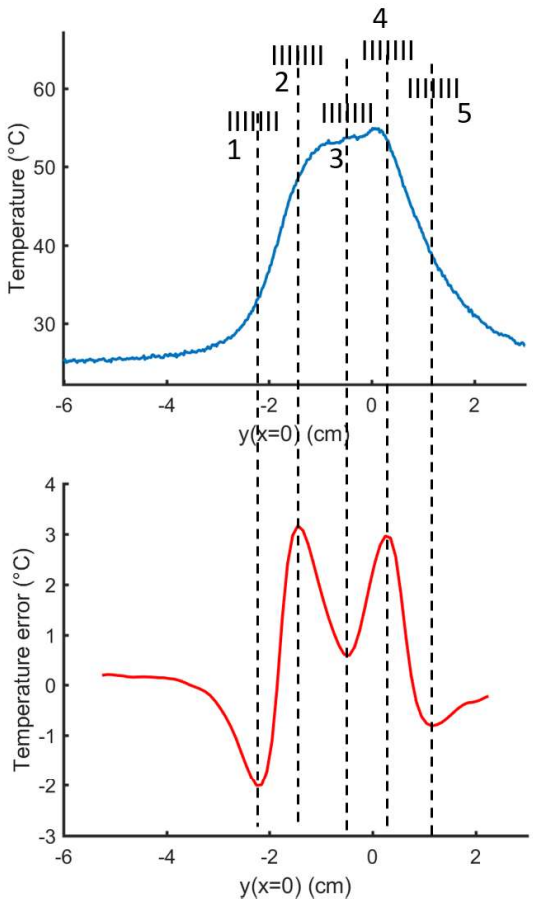

Figure 5.8: Temperature error (bottom) provided by a 1.5 cm FBG shifted along the temperature distribution (top).

diffusing part, the error is 0.7 °C.The temperature non-linearity has thus an effect on the sensor output and it can be considered as an influence quantity on the FBG measurement.

Moreover, the obtained error is valid only for a 1.5 cm length FBG, but it should be smaller in case of a shorter one. As a verification, another simulation was carried out keeping the FBG always in the same position but reducing its length. For the position $(x, y) = (0,1.5)$ (i. e. where the error function presents a maximum) the error corresponding to different FBG lengths is reported in Fig. 5.9 where it can be seen that the error monotonically decreases with the sensor length, starting from 3 °C when the sensor is 1.5 cm long to 0.5 °C when its length is 1 mm. As a consequence, the optimal solution would be to work with a sensor as short as possible but, unfortunately, as the sensor length decreases the spectral response intensity decreases and the peak width increases (Fig. 5.9 (right)) thus compromising the accuracy in the peak identification. Moreover, the risk of spectra

overlapping, in case of an FBG array, is higher. A reasonable compromise is to use sensors having a length of a few millimeters.

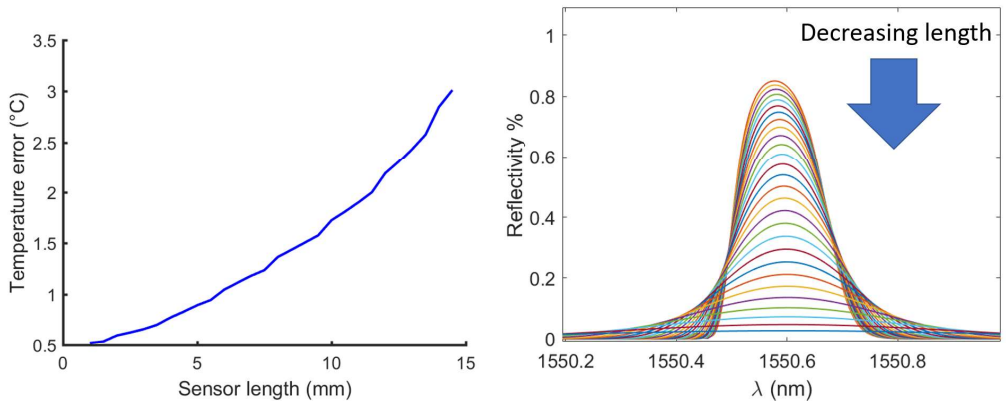

Figure 5.9: Error for different FBG lengths (left); the corresponding increasing peak width and intensity reduction (right).

In order to verify the results obtained from simulations, an experimental setup was devised which is based on the agar phantom already employed in Chapter 4. Even in this case, in order to have an accurate metallic reference sensor, was not possible to use the laser. Therefore, the agar was not loaded with the ink and was heated with a cylindrical resistor. The aim of this test was to compare, under the same non-linear temperature profile, FBGs with different lengths and thermocouples. The following sensors were embedded inside the agar perpendicularly to the cylindrical resistor:

- a silica 10/125 µm fiber with a 1.5 cm FBG inscribed, previously characterized on the setup for linear gradients, in order to know the exact position of it (FBGL);
- a silica 10/125 µm fiber with three 1 mm length FBGs inscribed, spaced by 4 mm (FBG1, FBG2, FBG3, FBG4);
- four type-T thermocouples placed one on the resistor and then every 5 mm in order to cover the whole longer FBG length.

The resistor was turned on and the temperature was recorded from all the sensors. The measurements recorded at steady state conditions are reported in Fig. 5.10. Here the temperatures from the four thermocouples have been interpolated in order to compare values at the FBG positions. It appears that, as reported in Table 5.1, the longer FBG (FBGL) presents a higher temperature difference since the distribution is not linear along it. For the shorter FBGs (FBG1, FBG2, FBG3,

FBG4) the difference is smaller and is comparable with their expected uncertainty (±0.6 °C)and to the uncertainty due to the non-perfect knowledge of the sensor position (±0.5 mm).

Table 5.1: FBGs measured values

	FBG L	FBG 1	FBG 2	FBG 3
Position P (mm)	8	4	8	12
Taverage (Celsius)	45.6	50.2	43.5	37.4
Tmeasured (Celsius)	41.8	49.2	42.5	38

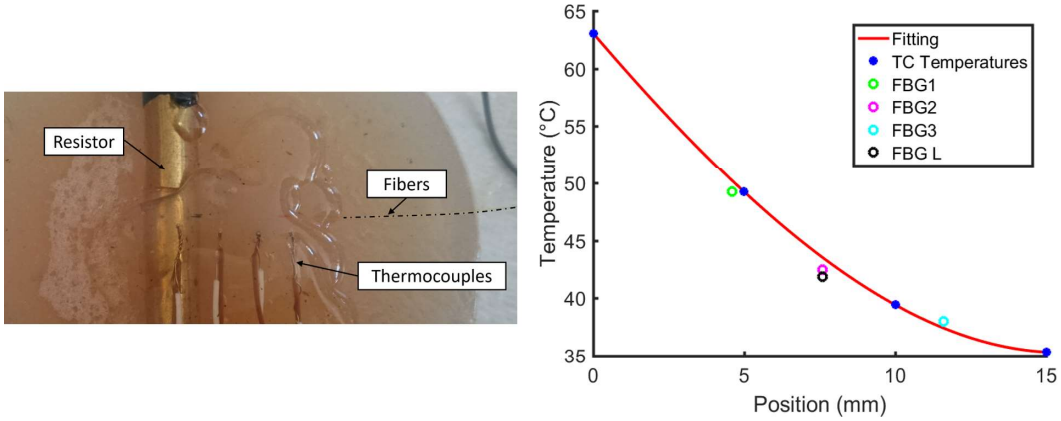

Figure 5.10: Agar setup with two fiber placed perpendicularly to a resistor (left); measurements taken from the different temperature sensors (right).

5.3 Validation in liver phantom

In this section, are described the procedures developed to validate the probes composed of FBGs encapsulated in a quartz capillary. In these tests the simplest probe version, having separated delivery and measurement fibers, was used. The measurement fiber embeds three 1.5 cm FBGs arranged in the quartz capillary with the 1 cm diffusing fiber, sealed and fixed on one side. The three FBGs are placed in order to cover different regions on the diffusing part: the first (FBG1) is in the area of almost uniform irradiation (and thus temperature), the second (FBG2) is on the edge of the irradiating part and the third (FBG3) is outside the radiating region, far from the fiber tip. The FBGs centers are spaced of about 1 cm. In presence of the laser light, was not possible to use metallic sensors to validate FBGs measurements and the agar was loaded with ink in order to reproduce

the ex-vivo liver conditions. An IR-camera was used to register the temperature at the phantom. Also in this case, as already done to estimate the temperature distribution due to the laser, the phantom was made with different slices, in order to quickly remove the upper one and take a more accurate measure with the IR-camera. The probe was placed into the phantom and the laser turned on with power between 2 W and 3 W. The temperature was recorded, simultaneously from all the FBGs, for the entire procedure. After about 10 minutes the temperatures were steady and the camera was turned on. Then, the laser was turned off, the upper agar layer quickly removed and the internal images were taken for few seconds. The FBG measures were compared with the average temperature as recorded by the camera after the layer removal. An example of the results obtained with this procedure is reported in Fig. 5.11. Here, as expected, there is a good agreement between the FBG1 measure and the average temperature measured with the camera. This is because the sensor is in a region of almost uniform temperature. FBG2, instead, measures a lower value with respect to the average, and this can be explained with the results obtained in Chapter 4, since FBG2 is in a region of non-uniform temperature, therefore it will underestimate the average temperature. FBG3 is, as FBG1, in another area of uniform temperature, so, once again, its measure is in good agreement with the camera, with a difference of 0.2 °C from the first measurement taken by the camera immediately after the agar slice removal.

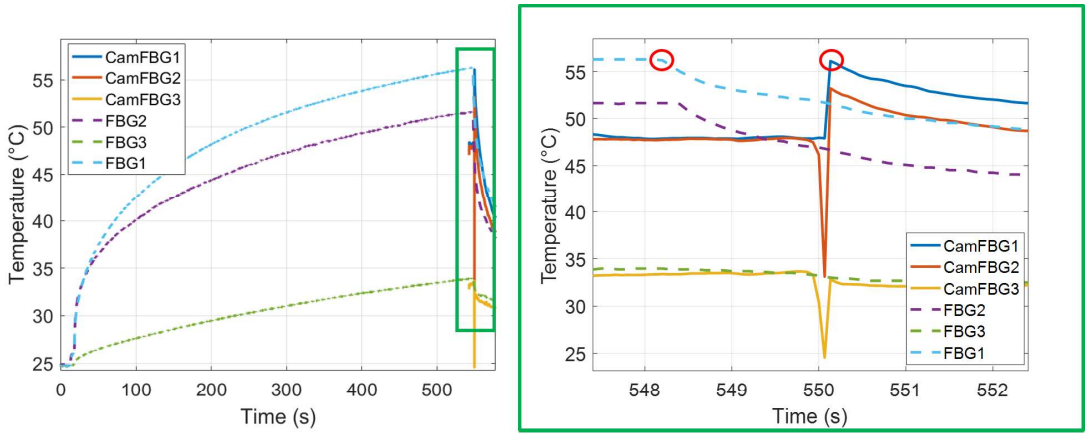

Figure 5.11: Results obtained with 2 W. On the left are reported the temperature during the whole experiment. On the right, the magnification of the green box, where the camera was used to record the temperature evolution for about 30 s. The two red circles represent the two points that are considered for the comparison between the camera and the FBG. The spike at time 550 s is due to the operator's hand.

Further tests were carried out using the probe composed of a single fiber. This probe is based on the double cladding fiber and it has two gratings of 3 mm in

length, spaced by 5 mm. A quartz glass capillary prevents any strain transfer. The validation procedure was made using a different setup still based on the thermo-optic liver phantom already described. In this setup, the ink-loaded agar gel was poured on a plastic cylindrical pot of 3 cm in height and 9 cm in diameter. During the solidification, the probe was positioned on the upper surface in order to be covered by a thin agar layer (Fig. 5.12).

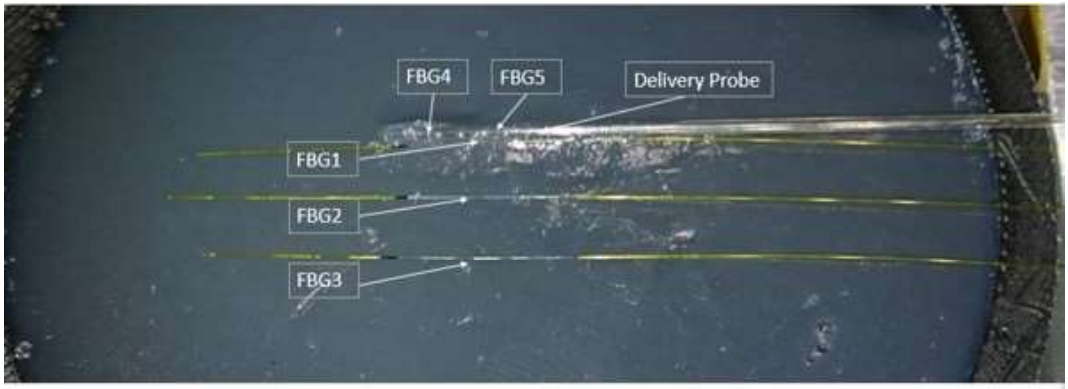

Figure 5.12: The FBGs during the validation test with laser.

The test aim is to compare longer and shorter gratings and to measure the temperature distribution around the probe, so three furthers 1.5 cm gratings have been placed on the phantom surface. With reference to Fig. 5.12:

- FBG1 is placed just outside the capillary, in close contact with the capillary;
- FBG2 and FBG3 are placed parallel to FBG1, at 0.5 cm and 1 cm from it, respectively;
- FBG 4 is inside the dual-cladding fiber core, proximal to the probe tip, in the region of maximum light emission (that is in the middle of the modified part of the fiber);
- FBG5 is in the dual-cladding fiber core, distal from the fiber tip.

Since in this test the probe is also able to deliver the laser light, no further metallic sensors were placed to measure the temperature. Therefore, in this particular case, the reference measurement can be obtained with the IR-camera (Fig. 5.13).
The test procedure was as follow:

1. the phantom was covered with another thick agar slice;
2. the laser was turned on and the temperature from the FBGs registered;

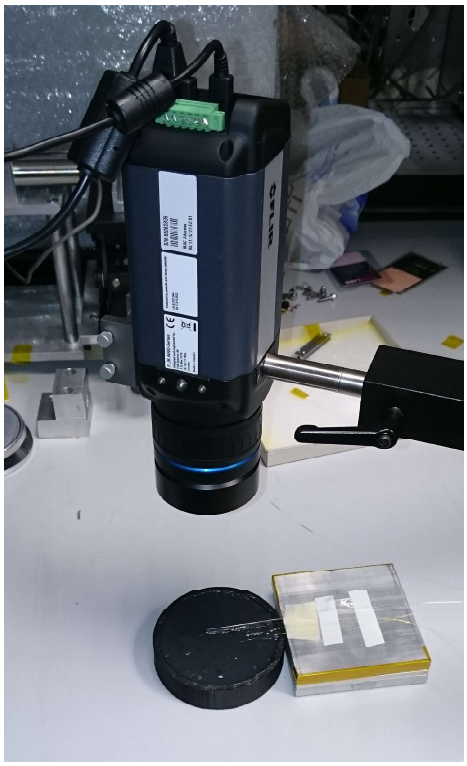

Figure 5.13: Position of the IR-Camera on the agar phantom to record the experiment temperature.

3. once the temperature from the sensors was steady, the upper agar slice was removed and the camera turned on;

4. the uncovered sensors reach another steady state; then the laser was turned off while the camera was still recording.

Test results are reported in Fig. 5.14 where it can be seen the behavior of each sensor and the temperature increase recorded with the camera up to a steady state.

The laser was set in order to deliver a power of only 2 W to avoid temperatures higher than the agar melting point. After about 12 minutes the upper layer was removed and the temperature of the sensors closer to the laser source measure a temperature increase of a few degrees. These sensors, FBG4 FBG5 and FBG1, measured almost the same value, with a maximum difference of 3 °C between FBG4 and FBG1; this is reasonable since FBG4 is in the hottest point, where the radiation is higher, and FBG1 includes a larger region outside the capillary. FBG1 measure is in good agreement with the one provided by FBG5, with a difference of 0.4 °C, which is positioned where the radiation starts to decrease along the fiber. A higher gradient is registered, instead, perpendicularly to the probe, from FBG2 and FBG3. In that direction, the temperature falls of about 20 °C/cm because of the large

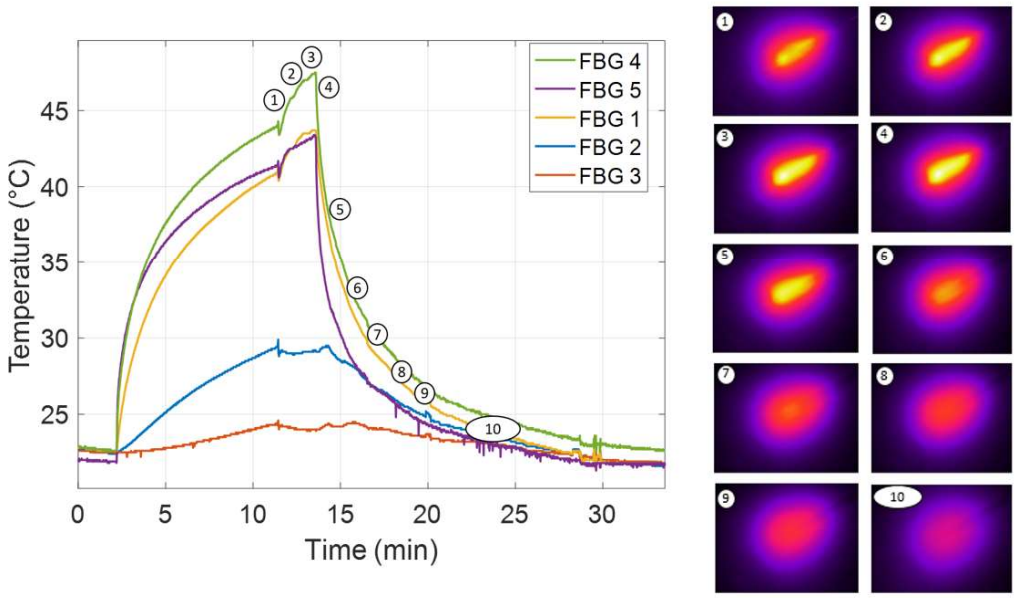

Figure 5.14: Temperature measured from the five FBGs (left). Thermal evolution recorded from the IR-camera after the upper layer was removed (right).

thermal gradient. The comparison with the IR-camera was obtained averaging the pixels of the infrared image in the region of each grating. In Fig. 5.15 are reported the measurements of the three 1.5 cm length FBGs, compared with the averages from the camera. These are in good agreement and therefore a validation of FBGs measurements during an LA on liver phantom can be considered satisfactory.

The next step was to validate these measurements also on a real ex-vivo liver. This was done using the same approach as for the agar phantom, with the delivery fiber included between two swine liver slices (Fig. 5.16). In this case, only the probe made with the DC fiber with the two grating inscribed has been used, and the measurements have been compared once again with the average temperature taken by the camera after the upper layer removal.

The results are reported in Fig. 5.16 where are shown the measurements of the two grating during the whole test and the average obtained from the camera images for a few seconds during the upper layer removal. The test lasts for ten minutes, with 2 W of laser power, and produced the damage shown in Fig. 5.16 (right). In this case, the temperature registered from the FBGs are few degrees higher than in the phantom, probably because of the loaded agar optical absorption is lower than the liver one. However, the difference between the two FBGs (4 °C) is close to the one obtained in the phantom (6 °C), and the difference of the FBG in the hottest region (FBG4) with the measure of the camera is of 1 °C only (Fig. 5.17).

These results so far presented have shown the ability of FBGs sensors integrated into a laser delivery fiber to monitor LA. However, the described tests have been

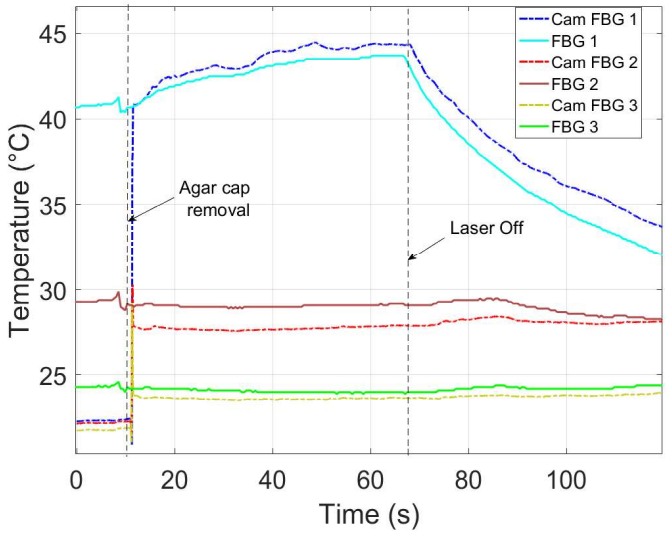

Figure 5.15: Comparison between the longer FBGs and the IR-camera measurements at the FBG position.

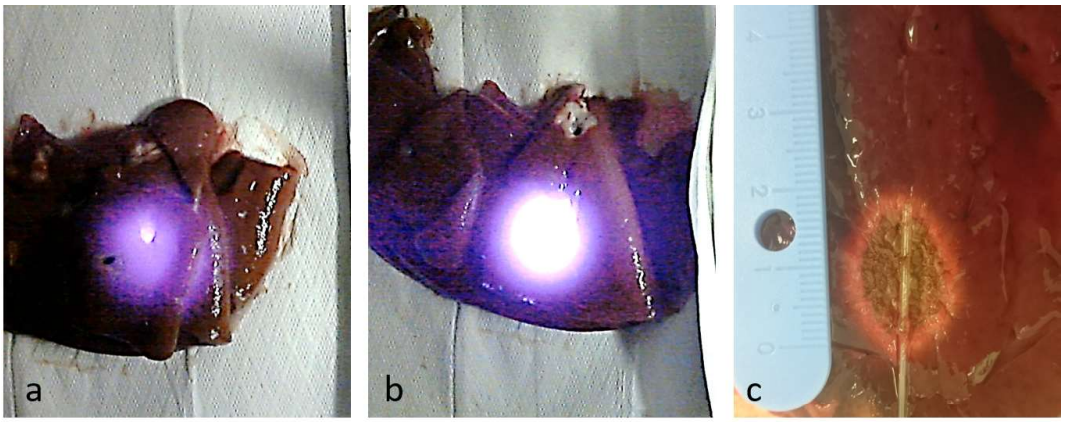

Figure 5.16: Validation test of the DC probe with two FBGs inscribed. (a) The probe included in liver slices; the picture shows a bright spot due to the transmitted laser light which is captured by the camera since it does not embed a strong filter for IR light. (b) Picture of the probe taken while the laser is on and the liver setup open; (c) damage produced by the probe when the power was set to 2 W for 10 minutes (1200 J).

carried out in phantoms and ex-vivo liver, so in conditions that can only approximate the behavior of human organs during a real LA since the presence of blood vessels and, more generally, organ perfusion cannot be taken into account using a bulky phantom.

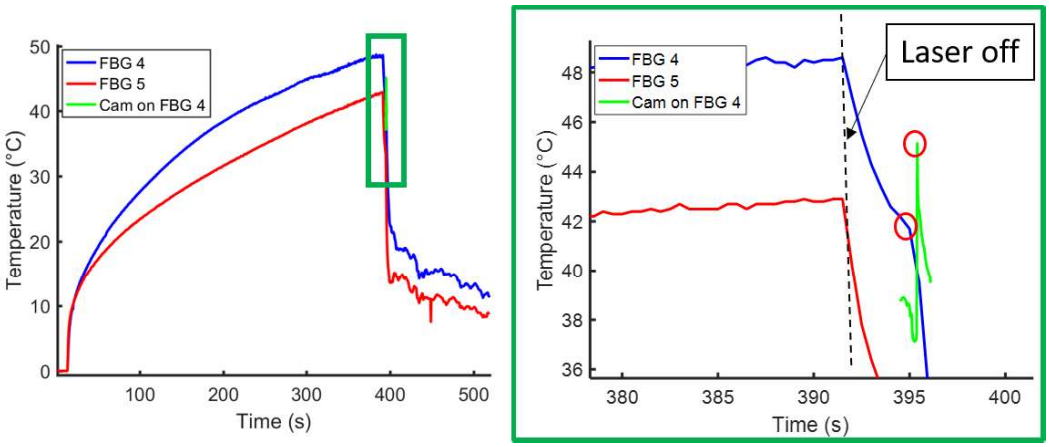

Figure 5.17: Comparison between the FBGs included in the DC fiber and the IR-camera. On the left is reported the temperature acquisition for the whole test; on the right, there is a magnification in order to see the comparison with the camera that acquired for few seconds during the upper layer removal. The red circles are the two points where the temperatures have been compared.

For these reasons, some very preliminary tests have been carried out using a modified setup that emulates the presence of a single vessel. This setup represents only a rough approximation of a live organ but it is useful to assess the quantitative effects on the temperature distribution and thus on the sensor measurements.

5.4 Thermo-optical model

As shown in the previous sections, FBGs are good candidates to monitor the ablation procedure in the presence of intense laser radiation since they do not affect the laser light propagation. It has been shown that few millimeters gratings can be included in a single DC fiber that both delivers the light and performs the measurements, thus allowing a minimally invasive probe to be devised. The results presented in the previous sections are all related to a simplified setup where the tissue around the probe, ex-vivo liver or agar-jelly phantom, is homogeneous and does not present any perfusion. The presence of blood flow is one of the main issues during thermal therapies since it drains a large amount of heat and it thus significantly affects the ablation results. Actually, the vessel heat sink effect can induce distortion in the temperature pattern around the probe and it can lead to a misunderstanding in the interpretation of the FBG temperatures. In order to study this problem, a thermo-optical model was implemented which employs a Finite Element Method (FEM) software that combines ray tracing with heat transfer in solids in a 2D geometry. For the sake of simplicity, the liver block was modeled as a circle and the results obtained from these simulations have been preliminarily validated by means of ablations performed in ex-vivo liver (Fig. 5.18)

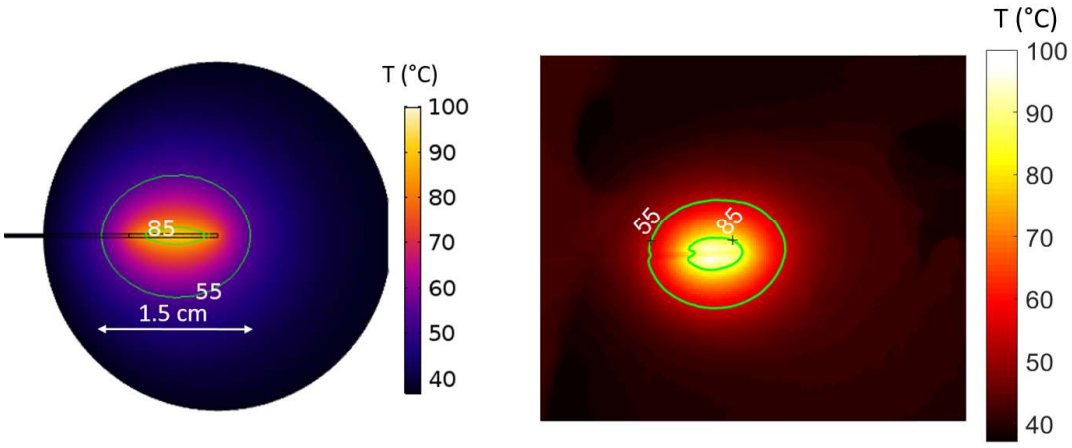

Figure 5.18: Comparison of the isothermal curves obtained from simulations (left) and thermal camera during a real ex-vivo liver ablation (right). The validation of the FEM results in the ex-vivo case allowed the investigation of the in-vivo case with blood perfusion.

It turned out that, even from simulations, with 2 W is possible to reach a cytotoxic region (>55 °C) of about 1.5 cm in length.

This result ensures the simulation validity in the uniform case and it was therefore used to forecast also different conditions where a blood vessel is present. This

situation can be described by the Pennes's equation (Eq.),

$$\rho c_{\mathrm{p}} \frac{\partial T}{\partial t} = \nabla \cdot (k \nabla T) + Q_{\mathrm{laser}} + \omega_{\mathrm{b}} c_{\mathrm{b}} \rho_{\mathrm{b}} (T - T_{\mathrm{b}}) + Q_{\mathrm{m}} \tag{5.1}$$

where ρ_{b}, c_{b}, ω_{b} and T_{b} are, respectively, the blood density, specific heat, perfusion rate and average temperature: these are the quantities needed to evaluate the blood perfusion effect. Q_{m} models the heat source due to metabolic processes, while ρ, c_{p} and k are, respectively, the medium density, specific heat and conductivity, and Q_{laser} is the power source term that takes into account the laser light absorption in the medium (values in Tab. 5.2).

Table 5.2: Parameters values employed in thermo-optic simulations.

Parameter	Value
ω_{b}	$0.064\,\mathrm{s}^{-1}$
c_{b}	$4180\,\mathrm{J/kgK}$
ρ_{b}	$1000\,\mathrm{kg/m}^3$
T_{b}	$37\,^{\circ}\mathrm{C}$
Q_{m}	$0\,\mathrm{W/m}^3$

The metabolic heat rate is usually considered to be negligible, whereas the blood perfusion deeply affects the treatment. Specifically, blood perfusion has the effect of producing a general cooling of the treatment environment and leads to distortions in the otherwise uniform thermal distributions obtained in laser ablation. As these non-uniformities are not easily predictable, it is useful to rely on computational tools in order to simulate the effect of such distortions on the heating process. Given this, it was evaluated the effect of a blood vessel located in different positions around the probe, in order to see if the sensors inside the capillary can discriminate these situations and can give reliable information which can be employed to adjust the laser power and control the ablation size.

5.5 Experimental setup mimicking in-vivo conditions

The liver model described in the previous section was modified by adding a 8 mm circle that emulates a vessel located as shown in Fig. 5.19.
From the simulation results, it is possible to see a reduction of the ablation region as large as few millimeters. The temperature distribution along the fiber axis was studied considering several different vessel distances from the probe (2, 5 and 7 mm, where the distance is considered from the tangent line to the circle). The results are reported in Fig. 5.20, where, in the worst situation, a temperature reduction of

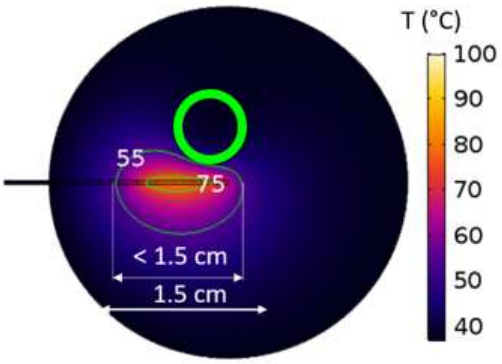

Figure 5.19: Simulation with a blood vessel in proximity of the ablation probe.

up to 5 °C can be observed with respect to a non perfused case, while, after 7 mm, the effect can be considered negligible.

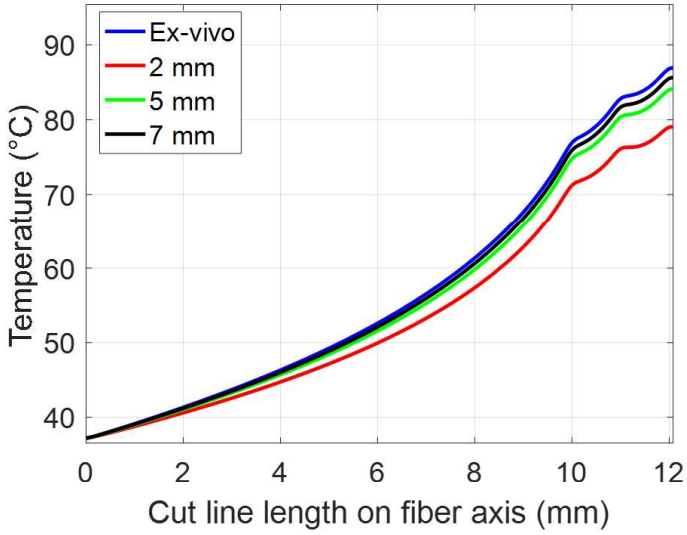

Figure 5.20: Temperature distribution along the LA probe for different blood vessel distances.

The results concerning the worst situation were validated through experiments. To this aim, a PVC pipe was inserted in the agar-loaded phantom during the solidification, and a pump was employed to force a water flow of (240 dm^3/h) (Fig. 5.21).

Temperature was measured using a fiber that embeds four FBGs having length of 1 mm and spaced by 5 mm. The probe was inserted in the phantom, through a 16 G needle at 2 mm from the tube. The laser power was set to 2 W for 10 minutes. In order to have a comparison between the simulations of in-vivo (circulating water)

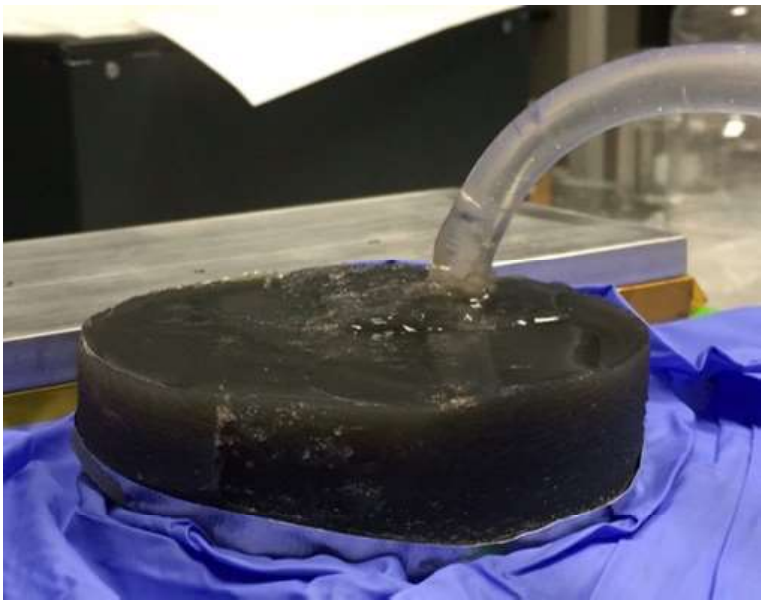

Figure 5.21: In-vivo phantom with the PVC tube inserted to emulate a blood vessel.

and the ex-vivo (no perfusion) organs, the in-vivo was performed at first, then the tube was removed and the gap was filled with other agar and the test repeated.

The comparison between simulations and experimental results is reported in Fig. 5.22, where it can be seen that there is still a mismatch between simulations and experiments that can be explained with the differences between the liver phantom realized and simulated, in terms of optical absorption and thermal coefficients. However, in both simulations and experimental tests, the blood vessel (circulating water) has modified the temperature sensed by the FBGs inside the probe and therefore it could be feasible to adjust the simulation parameters in order to forecast several in-vivo situations, with the probe in proximity of a large blood vessel.

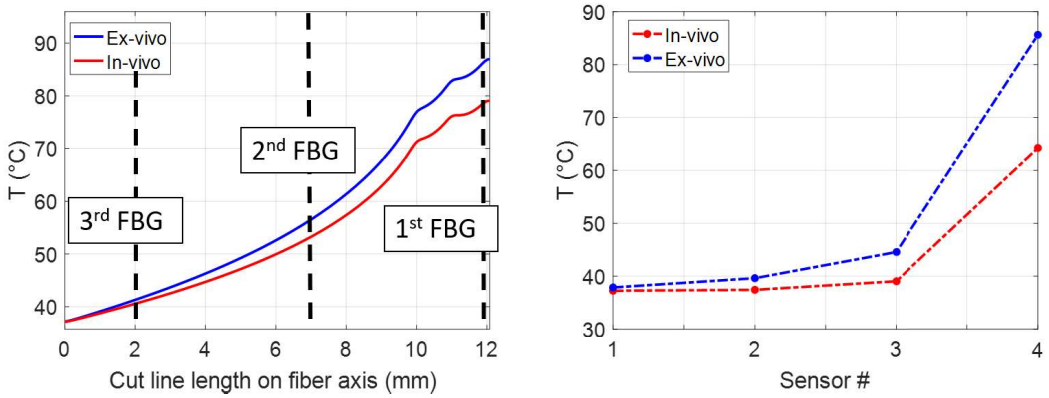

Figure 5.22: Comparison of the temperature distribution along the LA probe in the ex-vivo and in-vivo case between simulations (left) and experiments (right).

Chapter 6

In-vivo experimental tests

Part of the results described in this chapter have been already published in [103] (including Fig. 6.2 and Fig. 6.3) and have been obtained in collaboration with the Institut de Chirurgie Guidée par l'Image IHU in Strasbourg (FR).

The results described in the previous chapter showed that a probe composed of delivery laser fiber and temperature measurement fiber is able to heat the tissue above the cytotoxic level and to measure the temperature increase due to laser absorption. The obtained results are promising but they do not take into account all the aspects related to a real, in-vivo, scenario. The problem of perfusion was preliminarily considered in the last tests shown in 5, anyway, the blood flux was merely modeled as a single vessel, whereas the blood flux is distributed among several vessels and their combined effects depend on aspects that can be hardly taken into account:

- vessels position, or the positioning of the needle in which the probe has to be inserted, often not so accurate;
- the artifacts given by the patient movement.

In order to better understand all these aspects, some tests on animal models were performed thanks to the collaboration with the Institut de Chirurgie Guidée par l'Image (IHU) in Strasburg (FR).

In this chapter are reported the preliminary results obtained using the developed probe to perform LA in liver and pancreas.

6.1 Porcine liver and pancreas LA under CT/MR imaging

Taking advantage of the IHU facilities, in-vivo LA experiments have been conducted on three pigs liver and pancreas, under CT 6.1 and MRI guidance.

Figure 6.1: Picture of a pig under CT scanner employed for the LA experiment.

Given the experimental phase, the delivery probe employed was equipped with one 1.5 cm FBG with central wavelength at 1555.6 nm on a separate fiber, in order to replace it or change its position if needed. The radiating probe portion was 1.5 cm, the same as the grating length, which means that on the one hand, the damage produced can fit a typical tumor size in both pig liver and pancreas and, on the other hand, the sensor can work in an approximately uniform temperature distribution, if correctly overlapped with the emitting portion.

The two fibers, delivery and sense, were put together into the already described 1.2 mm (outer diameter) quartz capillary, which was sealed and glued. The overall probe length is few centimeters longer than the emitting portion (Fig. 6.2). For comparison purposed and in order to map the treatment surrounding area at different positions, another external probe was devised. It was based on an FBGs array of seven elements of 1 mm each, spaced by 2 mm, for a total length of 13 mm (apodized, with a reflectivity >90%, acrylate-coated, Broptics Technology Inc., Taipei, Taiwan), embedded into a carbon fiber needle (1 mm of external diameter) filled with thermal paste (Fig. 6.3).

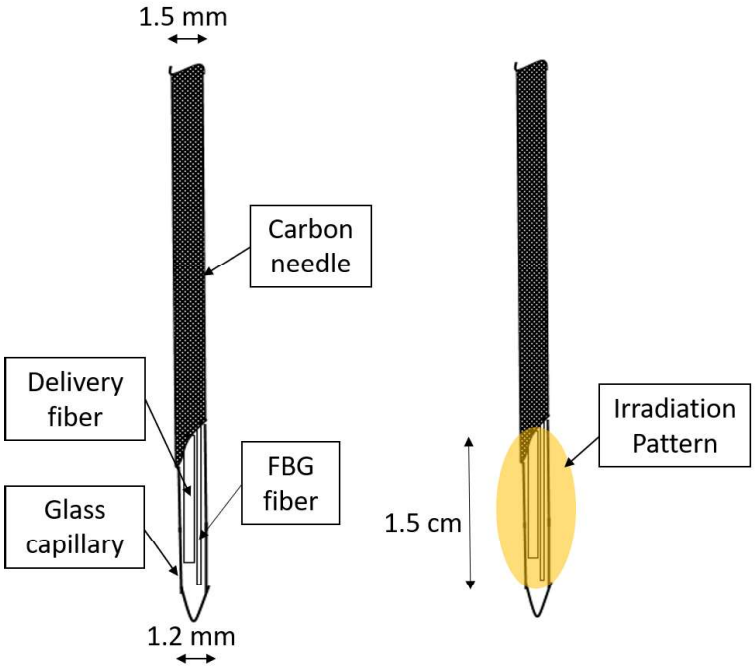

Figure 6.2: Sketch of the FBG equipped probe employed for the tests on pigs.

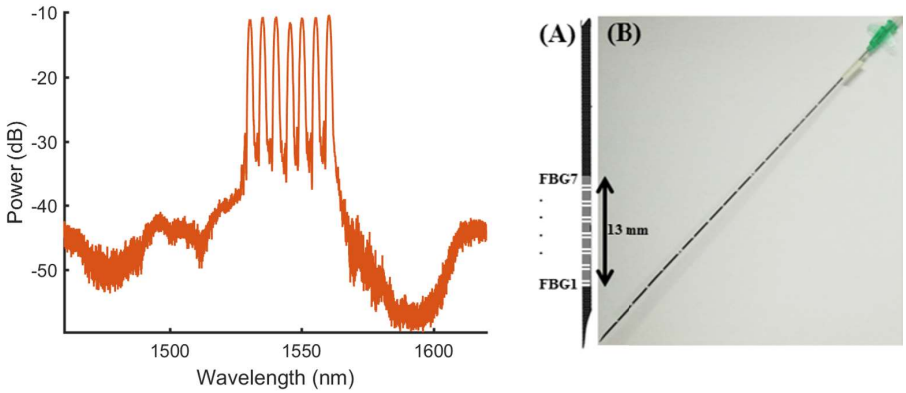

Figure 6.3: Spectrum of the FBGs array (left); FBG equipped needle (right, b) employed to map the temperature in the surrounding of the laser probe. It has seven sensor that are labeled from 1 to 7 starting from the needle tip, as shown in the sketch (right, a).

No metallic parts were employed so everything was, therefore, compatible with the MRI facility that was employed to facilitate the probes positioning and also, in perspective, to perform temperature measurements. Results concerning MRI temperature measurements are not shown in this thesis. The FBG-equipped laser probe was then percutaneously inserted by means of a 1.5 mm (internal diameter)

needle in a liver or pancreas region and, always under MRI guidance, the FBGs carbon needle was positioned parallel to the primary probe, at 4 mm of distance.

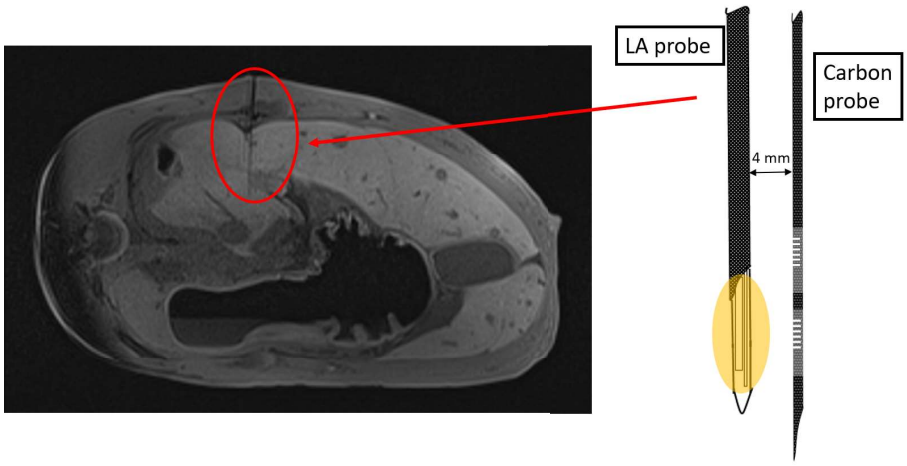

Figure 6.4: Example of an MRI image, taken just before the experiments, showing the probes arrangement inside the pig liver.

During these experiments, several LA ablations were performed in different liver or pancreas locations. The pigs were under heavy anesthesia (10 cm^3 of Propofol and 5 cm^3 of Esmeron, 2% isoflurane), in order to avoid any pain but still autonomously breathing, and, after the experiments, they were immediately sacrificed. These animals did not have any tumors, since the first aim of the activity was to control the treatment, even on healthy tissues. Therefore, the positions (Fig. 6.4) in which the LA were performed have been chosen from surgeons, according to their experience, among the most common for a liver or pancreas tumor eligible for an LA.

In the following are reported, as an example, the results obtained for the first pig during a liver ablation with a power setting of 3 W applied for 10 minutes. The sensors were all acquired by means of the optical interrogator (Micron Optics, si155) through two different channels and had been stored both the raw spectra, with a sampling frequency of 1 Hz, and the peak tracking provided by the acquisition system, with a frequency of 10 Hz. Raw spectra were acquired as a backup, just in case something went wrong with the system algorithm since sometimes it can happen with short gratings that the reflectivity is too weak and the peak tracking can be lost.

This is problem happened in the test of Fig. 6.5 where is shown the comparison between the temperature variations obtained from the fitting algorithm applied to the 1 Hz acquired spectra and the peaks tracking at 10 Hz directly provided by the

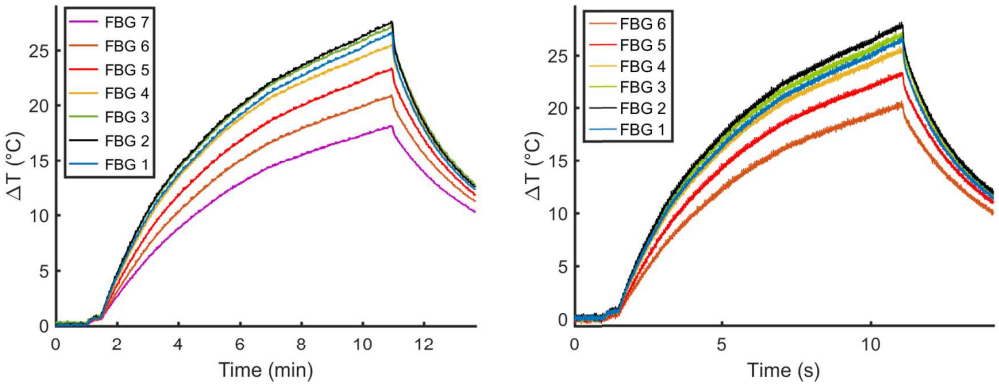

Figure 6.5: Comparison between the temperatures obtained by fitting the spectral responses acquired at 1 Hz (left) and the temperatures obtained by the peak tracking at 10 Hz provided by the acquisition system (right).

acquisition system. In this test, the *FBG 7* in the array was not recognized by the system and would have been lost, but has been retrieved from the spectral analysis. The maximum difference between the two algorithms is of 0.2 °C and it is mainly due to the noise present in the faster acquisition.

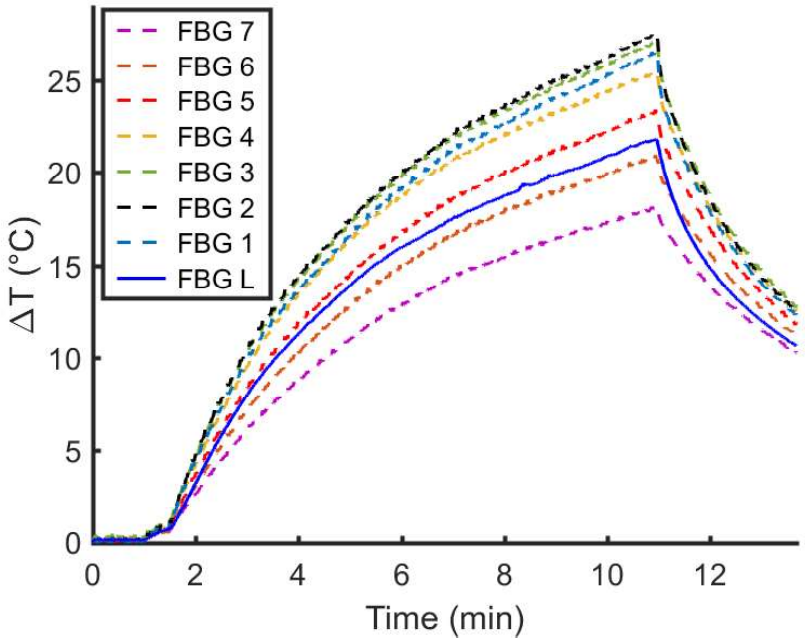

Figure 6.6: Temperature variations obtained from all the sensors employed. The laser was turned on at minute 1 and turned off at minute 11.

In Fig. 6.6 are reported the temperature evolution measured from all the sensors (1 Hz acquisition) employed in the LA ablation on the pig liver and here is possible to see the effect of a longer grating (FBG L) with respect to the shorter: even if the temperature was supposed to be uniform along the probe, the long FBG provides a temperature that is closer to the average of the temperature measured with the array. Moreover, the temperature of the longest FBG should be higher than the other, because of the 4 mm nominal distance between the probes, but, given the issues in the positioning of the insertion needles, the probes are probably in close contact. Moreover, the carbon needle containing the FBGs array could absorb part of the laser light, thus resulting in higher measured temperatures. Although the power settings were higher than in the ex-vivo case (3 W against 2 W), considering a body temperature of 38 °C, it can be seen that the cytotoxic temperature of 55 °C was not reached in all the points, because of the blood perfusion that dramatically affects the treatment.

As mentioned before, one of the main issues that can occur during the in-vivo experiment and that was not present in the ex-vivo conditions, is the movement artifact that can be caused by several reasons but the predominant one, in these case, was the animal respiration. In Fig. 6.7 is reported a magnification of the 10 Hz acquisition where it can be seen that the motion due to the respiration apparently affects the measurements up to 1.2 °C. This problem only arises the FBGs array that is enclosed a more flexible embodiment, while it is not present in the sensor inside the delivery probe which is rigid.

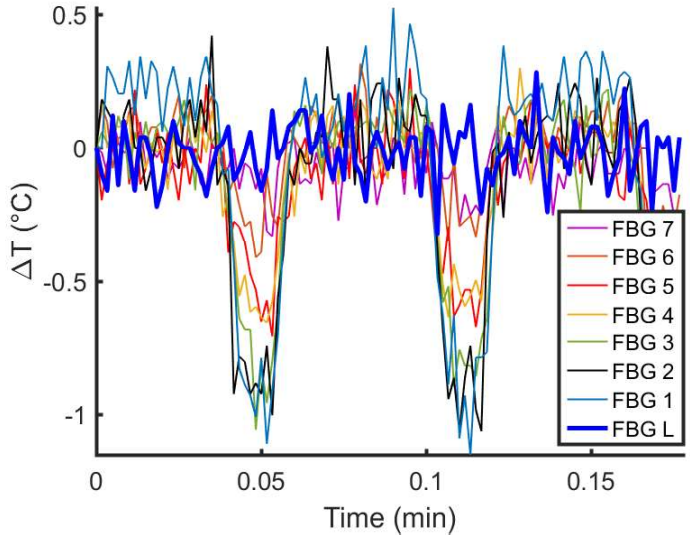

Figure 6.7: Respiration artifact affecting the measurements of the FBGs array. The temperature measured from the FBG in the applicator appears steady.

In order to see the spatial evolution of the ablated area, the temperatures from

the array have been plotted every 200 s (Fig. 6.8 (left)). The power was set to 3 W for 10 minutes. The Figure shows the evolution and the extension of the ablation region during the test and it shows the relative position between the irradiation pattern and the array. At 0 s the temperatures were uniform along the probe, then, at 600 s the temperature distribution was steady and reached its maximum value; at this point, the laser was turned off and the temperature decreases approaching its original value.

The reproducibility of the probe positioning was analyzed with a second ablation performed in another region of the same organ. The result is shown in Fig. 6.8 (right). The laser power was set to 5 W and thus the temperature at the end of the test was higher. Nevertheless, it is clear that the positioning of the second probe close to the ablation probe is a hard task since it was placed nominally in the same position of the previous test, but the measurements obtained with the FBG array show that the position with respect to the radiation pattern is different. The positioning difference is of about 5 mm and it is mainly due to the accuracy of the images taken from the MRI and the accuracy of the marks made on the probe to control the penetration depth.

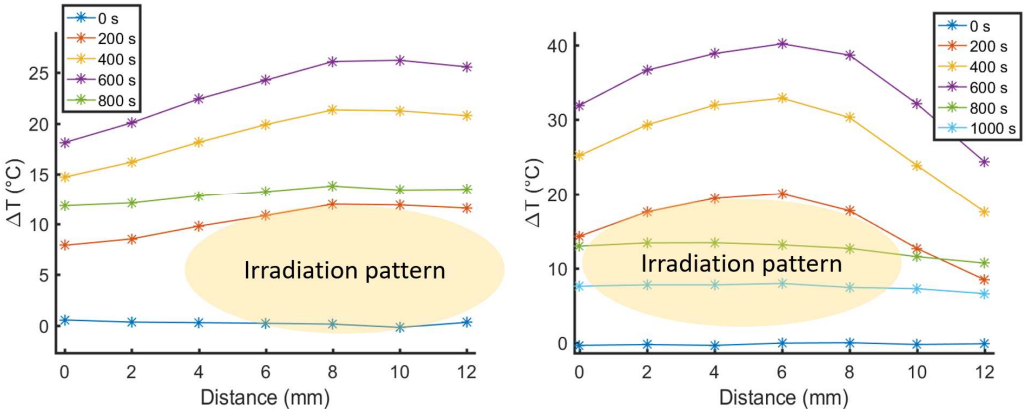

Figure 6.8: Spatial evolution of the temperature measured from the FBGs in the carbon probe positioned at 4 mm from the laser source with 3 W (left) and 5 W (right).

These results have shown that it is essential to measure the temperature during an LA procedure because the consequences strictly depend on the region that reached the cytotoxic temperature. Moreover, it has been highlighted the importance of the positioning of the sensors with respect to the source, because a mismatch can give large errors in the performed ablation estimation.

Given these results, temperature mapping with an auxiliary probe can be very useful to monitor the temperature in any arbitrary position but the positioning error prevents this approach to be really effective. The probe the integrates the sensor with the delivery fiber does not suffer from this problem.

Chapter 7

Conclusions

This thesis work aims to investigate Fiber Bragg Gratings as temperature sensors for laser ablation (LA) of solid tumors, a promising minimally-invasive technique that allows to locally treat several kinds lesions, especially in liver and pancreas.

One of the main issues of the LA is the control of the temperature distribution inside the tissues and, for this reason, the usage of LA is still limited since it presents the risk of undertreatment or unwanted damages to healthy structures. Nowadays, for the most of the commercial devices devised for LA, the laser light is delivered to the tumor site using an optical fiber and the amount of energy is set without any real-time feedback on the treatment effects. These devices do not embed temperature sensors since conventional sensors employed in clinical applications are electrical and they are thus not compatible with the laser radiation. The usage of dielectric sensors, like fiber sensors, is possible but still relegated to some research applications.

Among all the available fiber sensors, Fiber Bragg Gratings have been intensely investigated in this thesis work since they are the most suitable candidates to measure temperature during LA. This kind of fiber sensor is fully compatible with the laser light and can be integrated inside the same fiber employed to deliver the laser radiation thus obtaining an innovative all-fiber applicator that performs LA more safely and in a minimally invasive way.

In order to reach this goal, the performance of commercial FBGs have been evaluated at first. They are well-known sensors that have been already widely employed to measure temperature, but mainly in the structural monitoring field where uniform conditions occur.

FBGs are also sensitive to strain, so they must be protected to unwanted mechanical stresses. A temperature probe has been thus developed (Chapter 3) by encapsulating commercial FBGs into a glass capillary since it is compatible with the laser radiation. These developed probes have been firstly characterized in uniform temperature conditions using a climatic chamber to find their sensitivity with

the temperature. The resulted sensitivity values have always been close to the theoretical value of 10 pm/°C. However, since the considered application is the LA, and thus the temperature gradient along the sensor can as large as few degrees per millimeters, the measurement issues related to these conditions, different from the characterization conditions, have been analyzed. This has been one of the crucial points of this work since the analysis of the measurement errors provided by FBGs employed in non-uniform temperature conditions has not been wholly analyzed so far. The FBG behavior has been intensely investigated both by numerical simulations and experimental tests (Chapter 4). In particular:

- a numerical model that provides the response of an FBG sensor exposed to any arbitrary temperature distribution along its longitudinal axis has been implemented. According to the model, the FBG provides the average temperature in the presence of a linear temperature distribution;
- the position of the grating along the fiber affects the measurement results but the manufacturer provides this position with some millimeters of uncertainty only, that could correspond to some degrees of temperature error. This issue is often not considered in the literature, but it can lead to non-negligible errors. By taking advantage of the numerical result obtained from the model, an experimental setup able to generate reproducible linear temperature distribution has been realized. Experimental results carried out using the developed setup with a commercial grating have shown that the position can be found with a standard uncertainty of 0.3 mm, a value that is acceptable for the considered application;
- the load effect of the sensor embodiment has been evaluated by simulating the temperature pattern of a real laser ablation performed with a flat-tip delivery fiber. Different sensor embodiments have been considered and their effect on the temperature measurements have been computed. In the case of quartz glass, the error can reach up to 2 °C toward the probe tip. These values have been then experimentally verified with a simplified setup developed to compare different embodiments under the same non-uniform temperature distribution. These results can be very useful to quantify the error with other probe materials and to design a probe that minimizes the temperature load effect. Also, this aspect is frequently underestimated in other research works.

The possibility of integrating FBG sensors in the same applicator employed to deliver the laser energy has been considered in Chapter 5. A diffusive delivery fiber has been realized with the twofold purpose of eliminating the hot-spots that typically occur with flat-tip fiber and to have the monitoring sensor in a known position. The probe has been validated using a custom-made setup based on ex-vivo liver phantom/ex-vivo porcine liver. The setup exploits an IR-camera as a temperature reference sensor.

The temperature distribution provided by the new diffusive fiber has been recorded and it has been employed to compute, by simulations, the temperature errors which are related to the non-negligible sensor length. The errors have been verified with an experimental simplified setup.It turned out that, as expected, the error decreases with the sensor length, but also that the grating optical peak become wider and less prominent. Short FBGs are also more expensive than "standard" one because they are not so widespread. One of the outcomes of this thesis is thus a trade-off between sensor length, measurement accuracy and sensor cost: working with commercial FBGs, a good compromise is to use sensors having a length of some millimeters. In the particular case of the temperature pattern provided by the delivery probe developed in this thesis, the error can be as large as 3 °C for a grating of 1.5 cm length and it decreases to 0.5 °C for a 1 mm one.

Working with short FBGs was possible to integrate several FBGs with know position and length into the same fiber employed to deliver the laser. To this aim, a particular double cladding fiber with custom FBGs has been used to build a single fiber probe that has been validated in ex-vivo conditions and, afterward, employed to monitor the ablation in in-vivo conditions on pigs.

The results of these tests have shown that the proposed all-glass fiber probes meet several requirements: the strain sensitivity is drastically reduced and can be thus neglected, the sensor position is known and the associated temperature error can be quantified, the laser absorption is negligible. Moreover, the dimension of the single fiber probe has been significantly reduced.

The probes still present some drawbacks since the fibers are embedded into a quartz capillary, a material that is almost transparent to the laser radiation but that is very fragile and it must be handled with special care using an insertion needle when employed in in-vivo procedures. A preliminary investigation has been carried out in order to find a suitable material to be employed in real conditions and some promising results have been obtained with synthetic polymers such as PTFE.

Bibliography

[1] World Healt Organization. *Cancer*. Visited on 13-10-2018. Sept. 2018. URL: http://www.who.int/en/news-room/fact-sheets/detail/cancer.

[2] Max Roser. *Our World in Data*. Visited on 12-10-2018. 2018. URL: https://ourworldindata.org/.

[3] M. Plummer et al. "Global burden of cancers attributable to infections in 2012: a synthetic analysis". In: *The Lancet Glob Health* 4.9 (2016), e609–e616. DOI: 10.1016/S2214-109X(16)30143-7.

[4] Cancer Research UK. *Worldwide cancer mortality statistics*. Visited on 13-10-2018. Feb. 2014. URL: https://www.cancerresearchuk.org/health-professional/cancer-statistics/worldwide-cancer/mortality#heading-One.

[5] D. Hashim et al. "The global decrease in cancer mortality: trends and disparities". In: *Annals of Oncology* 27.5 (2016), pp. 926–933. DOI: 10.1093/annonc/mdw027. eprint: /oup/backfile/content_public/journal/annonc/27/5/10.1093_annonc_mdw027/2/mdw027.pdf. URL: http://dx.doi.org/10.1093/annonc/mdw027.

[6] American Cancer Society. *What Is Liver Cancer?* Visited on 13-10-2018. Apr. 2016. URL: https://www.cancer.org/cancer/liver-cancer/about/what-is-liver-cancer.html.

[7] Bruno Nardo et al. "Liver resection for metastases from colorectal cancer in very elderly patients: New surgical horizons". In: *International Journal of Surgery* 33 (2016). Special Issue from Italian Society of Geriatric Surgery 2016, S135–S141. ISSN: 1743-9191. DOI: https://doi.org/10.1016/j.ijsu.2016.06.014. URL: http://www.sciencedirect.com/science/article/pii/S1743919116301728.

[8] Yasunori Minami and Masatoshi Kudo. "Radiofrequency Ablation of Liver Metastases from Colorectal Cancer: A Literature Review". In: 7 (Jan. 2013), pp. 1–6.

[9] Saleh Daher et al. “Current and Future Treatment of Hepatocellular Carcinoma: An Updated Comprehensive Review”. In: *Journal of Clinical and Thanslational Hepatology* 6.1 (2018), pp. 69–78. DOI: 10.14218/JCTH.2017.00031. URL: https://www.ncbi.nlm.nih.gov/pmc/articles/PMC5863001/.

[10] Alexander Schlachterman et al. “Current and future treatments for hepatocellular carcinoma”. In: *World Journal of Gastroenterology* 21.28 (2015), pp. 8478–8491. DOI: 10.3748/wjg.v21.i28.8478. URL: https://www.ncbi.nlm.nih.gov/pmc/articles/PMC4515831/.

[11] Cardiovascular and Interventional Radiological Society of Europe. *Ablation*. Visited on 24-10-2018. URL: https://cirse.org/index.php?pid=1011.

[12] Markolf H. Niemz. *Laser-tissue interactions: fundamentals and applications*. Springer-Verlag Berlin Heidelberg, 2007. DOI: 10.1007/978-3-540-72192-5.

[13] Theodora A. Potretzke et al. “Microwave versus Radiofrequency Ablation Treatment for Hepatocellular Carcinoma: A Comparison of Efficacy at a Single Center”. In: *Journal of Vascular and Interventional Radiology* 27.5 (2016), pp. 631–638. ISSN: 1051-0443. DOI: https://doi.org/10.1016/j.jvir.2016.01.136. URL: http://www.sciencedirect.com/science/article/pii/S1051044316001573.

[14] Muneeb Ahmed et al. “Image-guided Tumor Ablation: Standardization of Terminology and Reporting Criteria—A 10-Year Update”. In: *Radiology* 273.1 (2014). PMID: 24927329, pp. 241–260. DOI: 10.1148/radiol.14132958. eprint: https://doi.org/10.1148/radiol.14132958. URL: https://doi.org/10.1148/radiol.14132958.

[15] Shaunagh McDermott and Debra A Gervais. “Radiofrequency ablation of liver tumors”. In: *Seminars in interventional radiology* 30.1 (Mar. 2013), pp. 49–55. ISSN: 0739-9529. DOI: 10.1055/s-0033-1333653. URL: http://europepmc.org/articles/PMC3700792.

[16] R. Illing and A. Gillams. “Radiofrequency Ablation in the Treatment of Breast Cancer Liver Metastases”. In: *Clinical Oncology* 22.9 (2010). Surgical Palliation In Malignant Disease, pp. 781–784. DOI: https://doi.org/10.1016/j.clon.2010.08.004. URL: http://www.sciencedirect.com/science/article/pii/S0936655510003110.

[17] Gerald D. Dodd et al. “Minimally Invasive Treatment of Malignant Hepatic Tumors: At the Threshold of a Major Breakthrough”. In: *RadioGraphics* 20.1 (2000). PMID: 10682768, pp. 9–27. DOI: 10.1148/radiographics.20.1.g00ja019. eprint: https://doi.org/10.1148/radiographics.20.1.g00ja019. URL: https://doi.org/10.1148/radiographics.20.1.g00ja019.

[18] SN Goldberg, GS Gazelle, and PR Mueller. "Thermal ablation therapy for focal malignancy: a unified approach to underlying principles, techniques, and diagnostic imaging guidance". In: *AJR. American journal of roentgenology* 174.2 (Feb. 2000), pp. 323–331. ISSN: 0361-803X. DOI: 10.2214/ajr.174.2.1740323. URL: https://doi.org/10.2214/ajr.174.2.1740323.

[19] Christopher Brace, J Louis Hinshaw, and Meghan Lubner. "Thermal Ablation for the Treatment of Abdominal Tumors". In: 7 (Mar. 2011).

[20] Viola Rieke and Kim Butts Pauly. "MR thermometry". In: *Journal of Magnetic Resonance Imaging* 27.2 (Jan. 2008), pp. 376–390. DOI: 10.1002/jmri.21265. eprint: https://onlinelibrary.wiley.com/doi/pdf/10.1002/jmri.21265. URL: https://onlinelibrary.wiley.com/doi/abs/10.1002/jmri.21265.

[21] Hanping Wu et al. "Real-time Monitoring of Radiofrequency Ablation and Postablation Assessment: Accuracy of Contrast-enhanced US in Experimental Rat Liver Model". In: *Radiology* 270.1 (2014). PMID: 23912621, pp. 107–116. DOI: 10.1148/radiol.13121999. eprint: https://doi.org/10.1148/radiol.13121999. URL: https://doi.org/10.1148/radiol.13121999.

[22] Hiroya Iida et al. "Effectiveness of impedance monitoring during radiofrequency ablation for predicting popping". In: 18 (Nov. 2012), pp. 5870–8.

[23] Alexis D. Kelekis et al. "Percutaneous treatment of liver tumors with an adapted probe for cooled-tip, impedance-controlled radio-frequency ablation under open-magnet MR guidance: initial results". In: *European Radiology* 13.5 (May 2003), pp. 1100–1105. DOI: 10.1007/s00330-003-1847-2. URL: https://doi.org/10.1007/s00330-003-1847-2.

[24] Jin Iwasawa et al. "Temperature-Controlled Radiofrequency Ablation for Pulmonary Vein Isolation in Patients With Atrial Fibrillation". In: *Journal of the American College of Cardiology* 70.5 (2017), pp. 542–553. ISSN: 0735-1097. DOI: https://doi.org/10.1016/j.jacc.2017.06.008. URL: http://www.sciencedirect.com/science/article/pii/S0735109717377331.

[25] Olaf J Eick. "Temperature controlled radiofrequency ablation". In: *Indian pacing and electrophysiology journal* 2.3 (2002), pp. 66–73. ISSN: 0972-6292. URL: http://europepmc.org/articles/PMC1564057.

[26] Maria Franca Meloni et al. "Microwave ablation in primary and secondary liver tumours: technical and clinical approaches". In: *International Journal of Hyperthermia* 33.1 (2017). PMID: 27416729, pp. 15–24. DOI: 10.1080/02656736.2016.1209694. eprint: https://doi.org/10.1080/02656736.2016.1209694. URL: https://doi.org/10.1080/02656736.2016.1209694.

[27] Camilo Correa-Gallego et al. "A Retrospective Comparison of Microwave Ablation vs. Radiofrequency Ablation for Colorectal Cancer Hepatic Metastases". In: *Annals of Surgical Oncology* 21.13 (Dec. 2014), pp. 4278–4283. DOI: 10.1245/s10434-014-3817-0. URL: https://doi.org/10.1245/s10434-014-3817-0.

[28] Paola Tombesi et al. "Thermal Ablation of Liver Tumours: How the Scenario Has Changed in the Last Decade". In: *EMJ Hepatol.* 6.1 (Apr. 2018), pp. 88–94.

[29] Naïk Vietti Violi et al. "Efficacy of microwave ablation versus radiofrequency ablation for the treatment of hepatocellular carcinoma in patients with chronic liver disease: a randomised controlled phase 2 trial". In: *The Lancet Gastroenterology and Hepatology* 3.5 (2018), pp. 317–325. DOI: https://doi.org/10.1016/S2468-1253(18)30029-3. URL: http://www.sciencedirect.com/science/article/pii/S2468125318300293.

[30] L. M. Neira et al. "Characterization and Analysis of Wideband Temperature-Dependent Dielectric Properties of Liver Tissue for Next-Generation Minimally Invasive Microwave Tumor Ablation Technology". In: *2018 IEEE/MTT-S International Microwave Symposium - IMS*. June 2018, pp. 911–914. DOI: 10.1109/MWSYM.2018.8439157.

[31] Rüdiger Hoffmann et al. "MR-guided microwave ablation in hepatic tumours: initial results in clinical routine". In: *European Radiology* 27.4 (Apr. 2017), pp. 1467–1476. DOI: 10.1007/s00330-016-4517-x. URL: https://doi.org/10.1007/s00330-016-4517-x.

[32] P. Saccomandi et al. "Temperature monitoring during microwave ablation in ex vivo porcine livers". In: *European Journal of Surgical Oncology (EJSO)* 41.12 (2015), pp. 1699–1705. DOI: https://doi.org/10.1016/j.ejso.2015.08.171. URL: http://www.sciencedirect.com/science/article/pii/S0748798315007696.

[33] D. Yang et al. "Measurement and Analysis of Tissue Temperature During Microwave Liver Ablation". In: *IEEE Transactions on Biomedical Engineering* 54.1 (Jan. 2007), pp. 150–155. DOI: 10.1109/TBME.2006.884647.

[34] L.A. Coldren, S.W. Corzine, and M.L. Mashanovitch. *Diode Lasers and Photonic Integrated Circuits*. Wiley Series in Microwave and Optical Engineering. Wiley, 2012. ISBN: 9781118148181. URL: https://books.google.it/books?id=GBB1kOYONT4C.

[35] D.R. Vij and K. Mahesh. *Medical Applications of Lasers*. Springer US, 2002. ISBN: 9780792376620. URL: https://books.google.it/books?id=RYQ3Q-3xkksC.

[36] H. Jelinkova. *Lasers for Medical Applications: Diagnostics, Therapy and Surgery*. Woodhead Publishing Series in Electronic and Optical Materials. Elsevier Science, 2013. ISBN: 9780857097545. URL: https://books.google.it/books?id=dg9IAgAAQBAJ.

[37] H.P. Berlien et al. *Applied Laser Medicine*. Springer Berlin Heidelberg, 2012. ISBN: 9783642189791. URL: https://books.google.it/books?id=gIDTBgAAQBAJ.

[38] Muneeb Ahmed et al. "Principles of and Advances in Percutaneous Ablation". In: *Radiology* 258.2 (2011). PMID: 21273519, pp. 351–369. DOI: 10.1148/radiol.10081634. eprint: https://doi.org/10.1148/radiol.10081634. URL: https://doi.org/10.1148/radiol.10081634.

[39] Klingenberg M. et al. "Multifibre Application in Laser-Induced Interstitial Thermotherapy under On-Line MR Control". In: *Lasers in medical science* 15 (Mar. 2000), pp. 6–14. DOI: 10.1007/s101030050041.

[40] Florian Streitparth et al. "Laser-induced thermotherapy (LITT)—evaluation of a miniaturised applicator and implementation in a 1.0-T high-field open MRI applying a porcine liver model". In: *European radiology* 20 (Nov. 2010), pp. 2671–8. DOI: 10.1007/s00330-010-1831-6.

[41] Clinical Laserthermia Systems AB. *Applicator Kit*. Visited on 25-10-2018. URL: https://clinicallaser.se/en/svenska-teknik/applikator-kit/.

[42] "A clinical study of thermal monitoring techniques of ultrasound-guided microwave ablation for hepatocellular carcinoma in high-risk locations". In: *Scientific reports* 7.41246 (Jan. 2017). DOI: 10.1038/srep41246. URL: https://www.ncbi.nlm.nih.gov/pmc/articles/PMC5255547/.

[43] "Residual tumor after laser ablation of human non-small-cell lung cancer demonstrated by ex vivo staining: correlation with invasive temperature measurements". In: *Magn Reson Mater Phy* 25.1 (Feb. 2012), pp. 63–74. DOI: https://doi.org/10.1007/s10334-011-0261-z. URL: https://link.springer.com/article/10.1007/s10334-011-0261-z#citeas.

[44] "Coagulation and temperature distribution in Nd: YAG interstitial laser thermotherapy: an in vitro animal study". In: *Lasers in Medical Science* 18.1 (Mar. 2003), pp. 19–24. DOI: https://doi.org/10.1007/s10103-002-0246-2. URL: https://link.springer.com/article/10.1007.

[45] Fabrice Manns et al. "In Situ temperature measurements with thermocouple probes during laser interstitial thermotherapy (LITT): Quantification and correction of a measurement artifact". In: *Lasers in Surgery and Medicine* 23.2 (), pp. 94–103. DOI: 10.1002/(SICI)1096-9101(1998)23:2<94::AID-LSM7>3.0.CO;2-Q.

[46] Fabrice Manns et al. *Mathematical analysis of the temperature field during ex-vivo and in-vivo experimental laser interstitial thermotherapy (LITT) in breast tissue models*. 1999. DOI: 10.1117/12.351000. URL: https://doi.org/10.1117/12.351000.

[47] E. Schena et al. "Thermocouples for temperature monitoring during pancreatic laser ablation: Analysis of the measurement error". In: *2015 IEEE International Symposium on Medical Measurements and Applications (MeMeA) Proceedings*. May 2015, pp. 219–223. DOI: 10.1109/MeMeA.2015.7145202.

[48] S A van Nimwegen et al. "Nd:YAG surgical laser effects in canine prostate tissue: temperature and damage distribution." In: *Physics in medicine and biology* 54 1 (2009), pp. 29–44.

[49] E Schena et al. "Experimental assessment of CT-based thermometry during laser ablation of porcine pancreas". In: *Physics in Medicine and Biology* 58.16 (2013), p. 5705. URL: http://stacks.iop.org/0031-9155/58/i=16/a=5705.

[50] G. Allegretti et al. "Magnetic resonance-based thermometry during laser ablation on ex-vivo swine pancreas and liver". In: *Medical Engineering and Physics* 37.7 (2015), pp. 631–641. ISSN: 1350-4533. DOI: https://doi.org/10.1016/j.medengphy.2015.04.001. URL: http://www.sciencedirect.com/science/article/pii/S135045331500096X.

[51] Paola Saccomandi, Emiliano Schena, and Sergio Silvestri. "Techniques for temperature monitoring during laser-induced thermotherapy: An overview". In: *International Journal of Hyperthermia* 29.7 (2013), pp. 609–619. DOI: 10.3109/02656736.2013.832411. eprint: https://doi.org/10.3109/02656736.2013.832411. URL: https://doi.org/10.3109/02656736.2013.832411.

[52] P T S Borman et al. "Towards real-time thermometry using simultaneous multislice MRI". In: *Physics in Medicine and Biology* 61.17 (2016), N461. URL: http://stacks.iop.org/0031-9155/61/i=17/a=N461.

[53] Robert D. Peters et al. "Magnetic resonance thermometry for predicting thermal damage: An application of interstitial laser coagulation in an in vivo canine prostate model". In: *Magnetic Resonance in Medicine* 44.6 (), pp. 873–883. DOI: 10.1002/1522-2594(200012)44:6<873::AID-MRM8>3.0.CO;2-X.

[54] Silvia Puccini et al. "Simulations of thermal tissue coagulation and their value for the planning and monitoring of laser-induced interstitial thermotherapy (LITT)". In: *Magnetic Resonance in Medicine* 49.2 (), pp. 351–362. DOI: 10.1002/mrm.10357. URL: https://onlinelibrary.wiley.com/doi/abs/10.1002/mrm.10357.

[55] Mingming Zhu, Ziqi Sun, and Chin K. Ng. "Image-guided thermal ablation with MR-based thermometry". In: *Quantitative Imaging in Medicine and Surgery* 7.3 (2017). URL: http://qims.amegroups.com/article/view/15306.

[56] R Correia et al. "Biomedical application of optical fibre sensors". In: *Journal of Optics* 20.7 (2018), p. 073003. URL: http://stacks.iop.org/2040-8986/20/i=7/a=073003.

[57] Fabrizio Taffoni et al. "Optical Fiber-Based MR-Compatible Sensors for Medical Applications: An Overview". In: *Sensors* 13.10 (2013), pp. 14105–14120. ISSN: 1424-8220. DOI: 10.3390/s131014105. URL: http://www.mdpi.com/1424-8220/13/10/14105.

[58] Emiliano Schena et al. "Fiber Optic Sensors for Temperature Monitoring during Thermal Treatments: An Overview". In: *Sensors* 16.7 (2016). ISSN: 1424-8220. DOI: 10.3390/s16071144. URL: http://www.mdpi.com/1424-8220/16/7/1144.

[59] M. Olivero et al. "Single mode-multimode-single mode optical fiber sensors: Review and application to temperature measurements using a bend-insensitive fiber". In: *2017 IEEE International Instrumentation and Measurement Technology Conference (I2MTC)*. May 2017, pp. 1–5. DOI: 10.1109/I2MTC.2017.7969863.

[60] Daniele Tosi et al. "Fiber optic sensors for sub-centimeter spatially resolved measurements: Review and biomedical applications". In: *Optical Fiber Technology* 43 (2018), pp. 6–19. ISSN: 1068-5200. DOI: https://doi.org/10.1016/j.yofte.2018.03.007. URL: http://www.sciencedirect.com/science/article/pii/S1068520017306302.

[61] Angela D Reid, Mark R Gertner, and Michael D Sherar. "Temperature measurement artefacts of thermocouples and fluoroptic probes during laser irradiation at 810 nm". In: *Physics in Medicine and Biology* 46.6 (2001), N149. URL: http://stacks.iop.org/0031-9155/46/i=6/a=403.

[62] Frank Hübner et al. "The influence of Nd:YAG laser irradiation on Fluoroptic® temperature measurement: an experimental evaluation". In: *Lasers in Medical Science* 28.2 (2013), pp. 487–496.

[63] Ngot Thi Pham et al. "Real-time temperature monitoring with fiber Bragg grating sensor during diffuser-assisted laser-induced interstitial thermotherapy". In: *Journal of Biomedical Optics* 22 (2017). DOI: 10.1117/1.JBO.22.4.045008. URL: https://doi.org/10.1117/1.JBO.22.4.045008.

[64] Ingemar Petermann. "Fibre Bragg Gratings : Characterization, Realization and Simulation". QC 20100812. PhD thesis. KTH, Microelectronics and Applied Physics, MAP, 2007, pp. viii, 64. ISBN: 978-91-7178-621-0.

[65] Sanjeev Dewra. "Fabrication and Applications of Fiber Bragg Grating-A Review". In: *Adv. Eng. Tec. Appl.* Vol. 4. 2. 2015, pp. 15–25.

[66] Carlos Rodrigues et al. "Development of a long-term monitoring system based on FBG sensors applied to concrete bridges". In: *Engineering Structures* 32.8 (2010), pp. 1993–2002. ISSN: 0141-0296. DOI: https://doi.org/10.1016/j.engstruct.2010.02.033. URL: http://www.sciencedirect.com/science/article/pii/S0141029610000866.

[67] Antonella Chiucchiolo et al. "Cryogenic test facility instrumentation with fiber optic and fiber optic sensors for testing superconducting accelerator magnets". In: *IOP Conf. Ser.: Mater. Sci. Eng.* Vol. 278. 1. IOP Publishing Ltd, 2017.

[68] Antonella Chiuchiolo, Andrea Cusano, and Marta Bajko. "Cryogenic Fiber Optic Sensors for Superconducting Magnets and Power Transmission Lines in High Energy Physics Applications". Nov. 2015. URL: https://cds.cern.ch/record/2162944.

[69] Marcelo M. Werneck et al. "A Guide to Fiber Bragg Grating Sensors". In: *Current Trends in Short- and Long-period Fiber Gratings*. Ed. by Christian Cuadrado-Laborde. Rijeka: IntechOpen, 2013. Chap. 1. DOI: 10.5772/54682. URL: https://doi.org/10.5772/54682.

[70] Marcelo M. M. Werneck, Regina C. S. B. Allil, and Fabio V. B. Nazaré. *Fiber Bragg Gratings: Theory, Fabrication, and Applications*. Vol. TT114. Spie Press Book, Sept. 2017, p. 256. URL: https://spie.org/Publications/Book/2286557?SSO=1.

[71] H.Venghaus. "Wavelength filters in fibre optics". In: *Wavelength filters in fibre optics*. Vol. 123. Berlin, Heidelberg: Springer, 2006. DOI: https://doi.org/10.1007/3-540-31770-8.

[72] C. Guattari et al. "Permittivity of Sub-Soil Materials Retrieved through Transmission Line Model and GPR Data". In: *Progress In Electromagnetics Research* 151 (2015), pp. 65–72. DOI: 10.2528/PIER15022002. URL: http://www.jpier.org/PIER/pier.php?paper=15022002.

[73] Nathan Ida. "Theory of Transmission Lines". In: *Engineering Electromagnetics*. Cham: Springer International Publishing, 2015, pp. 725–792. DOI: 10.1007/978-3-319-07806-9_14. URL: https://doi.org/10.1007/978-3-319-07806-9_14.

[74] James R. Wait. "Transmission and Reflection of Electromagnetic Waves in the Presence of Stratified Media". In: *Journal of Research of the National Bureau of Standards* 61.3 (Sept. 1958), pp. 205–232.

[75] Andreas Othonos. "Fiber Bragg gratings". In: *Review of Scientific Instruments* 68.12 (1997), pp. 4309–4341. DOI: 10.1063/1.1148392. eprint: https://doi.org/10.1063/1.1148392. URL: https://doi.org/10.1063/1.1148392.

[76] Nazmi A. Mohammed, Taha A. Ali, and Moustafa H. Aly. "Performance optimization of apodized FBG-based temperature sensors in single and quasi-distributed DWDM systems with new and different apodization profiles". In: *AIP Advances* 3.12 (2013), p. 122125. DOI: 10.1063/1.4859115. eprint: https://doi.org/10.1063/1.4859115. URL: https://doi.org/10.1063/1.4859115.

[77] Ginu Rajan. *Optical Fiber Sensors: Advanced Techniques and Applications*. CRC Press, Mar. 2015, p. 575. URL: https://www.crcpress.com/Optical-Fiber-Sensors-Advanced-Techniques-and-Applications/Rajan/p/book/9781482228250.

[78] G. Fusiek, P. Orr, and P. Niewczas. "Temperature-independent high-speed distributed voltage measurement using intensiometric FBG interrogation". In: *2015 IEEE International Instrumentation and Measurement Technology Conference (I2MTC) Proceedings*. May 2015, pp. 1430–1433. DOI: 10.1109/I2MTC.2015.7151486.

[79] National Instruments. *Fundamentals of Fiber Bragg Grating (FBG) Optical Sensing*. Visited on 04-10-2018. 2018. URL: http://www.ni.com/white-paper/11821/en/#toc4%201%20di.

[80] *Optical Spectrum Analysis - Application Note*. 1550. 4. Agilent Technologies. 2000.

[81] José Luis de Miguel et al. "Experimental Demonstration of Low-Uncertainty Calibration Methods for Bragg Grating Interrogators". In: *Sensors* 18.6 (2018). DOI: 10.3390/s18061895.

[82] Lucas Negri et al. "Benchmark for Peak Detection Algorithms in Fiber Bragg Grating Interrogation and a New Neural Network for its Performance Improvement". In: *Sensors (Basel)* 11.4 (2011), pp. 3466–3482. DOI: 10.3390/s110403466.

[83] A. Lamberti et al. "A novel fast phase correlation algorithm for peak wavelength detection of fiber Bragg grating sensors". In: *Opt. Express* 22.6 (Mar. 2014), pp. 7099–7112. DOI: 10.1364/OE.22.007099. URL: http://www.opticsexpress.org/abstract.cfm?URI=oe-22-6-7099.

[84] T. Bodendorfer et al. "Comparison of different peak detection algorithms with regards to spectrometic fiber Bragg grating interrogation systems". In: *2009 International Symposium on Optomechatronic Technologies*. Sept. 2009, pp. 122–126. DOI: 10.1109/ISOT.2009.5326110.

[85] S Triollet et al. "Discriminated measures of strain and temperature in metallic specimen with embedded superimposed long and short fibre Bragg gratings". In: *Measurement Science and Technology* 22.1 (2011), p. 015202. URL: http://stacks.iop.org/0957-0233/22/i=1/a=015202.

[86] LightGuideOptics Group. *LGO-Side Fire Fiber Probe*. Visited on 29-10-2018. URL: http://www.lgoptics.com/medical/.

[87] R. Gassino, A. Vallan, and G. Perrone. "Evaluation of temperature measurement errors due to FBG sensors during laser ablation of Ex-Vivo porcine liver". In: *2018 IEEE International Instrumentation and Measurement Technology Conference (I2MTC)*. May 2018, pp. 1–5. DOI: 10.1109/I2MTC.2018.8409636.

[88] Riccardo Gassino et al. "Issues and characterization of fiber Bragg grating based temperature sensors in the presence of thermal gradients". In: *Measurement* 124 (2018), pp. 15–19. ISSN: 0263-2241. DOI: https://doi.org/10.1016/j.measurement.2018.03.049. URL: http://www.sciencedirect.com/science/article/pii/S0263224118302331.

[89] K. R. Holmes. *Thermal Properties*. Visited on 28-10-2018. URL: http://users.ece.utexas.edu/~valvano/research/Thermal.pdf.

[90] Engineering ToolBox. *Thermal conductivity for common materials and products*. Visited on 28-10-2018. 2003. URL: https://www.engineeringtoolbox.com/thermal-conductivity-d_429.html.

[91] Min Zhang et al. "Experimental Determination of Thermal Conductivity of Water-Agar Gel at Different Concentrations and Temperatures". In: *Journal of Chemical and Engineering Data* 56.4 (2011), pp. 859–864. DOI: 10.1021/je100570h. eprint: https://doi.org/10.1021/je100570h. URL: https://doi.org/10.1021/je100570h.

[92] Ramajayam K., Yadav S., and Kumar A. "A novel method to determine the thermal conductivity of Tissue-Mimicking Gels". Nov. 2013.

[93] Ali Dabbagh et al. "Tissue-Mimicking Gel Phantoms for Thermal Therapy Studies". In: *Ultrasonic imaging* 36 (Mar. 2014). DOI: 10.1177/0161734614526372.

[94] H. Watanabe et al. "Temperature dependence of thermal conductivity of liver based on various experiments and a numerical simulation for RF ablation". In: *2010 Annual International Conference of the IEEE Engineering in Medicine and Biology*. Aug. 2010, pp. 3222–3228. DOI: 10.1109/IEMBS.2010.5627200.

[95] R. Gassino et al. "A Fiber Optic Probe for Tumor Laser Ablation With Integrated Temperature Measurement Capability". In: *Journal of Lightwave Technology* 35.16 (Aug. 2017), pp. 3447–3454. ISSN: 0733-8724. DOI: 10.1109/JLT.2016.2618618.

[96] R. Gassino et al. "Temperature Distribution Mapping Using an FBG-Equipped Probe for Solid Tumor Laser Ablation". In: *2018 IEEE International Symposium on Medical Measurements and Applications (MeMeA)*. June 2018, pp. 1–6. DOI: 10.1109/MeMeA.2018.8438779.

[97] Dowlat K. et al. "Image-guided percutaneous breast cancer ablation meeting at the American Society of Breast Surgeons". In: *The American Journal of Surgery* 182.4 (), pp. 429–433. DOI: https://doi.org/10.1016/S0002-9610(01)00768-1. URL: https://www.americanjournalofsurgery.com/article/S0002-9610(01)00768-1/fulltext.

[98] G. Park et al. *Fabrication and analysis of cylindrical diffusing optical fiber probe for photodynamic therapy in cancer treatment*. 2018. DOI: 10.1117/12.2289343.

[99] Germer C.T. et al. "Diffusing Fibre Tip for the Minimally Invasive Treatment of Liver Tumours by Interstitial Laser Coagulation (ILC): An Experimental Ex Vivo Study". In: *Lasers in Medical Science* 14 (Mar. 1999), pp. 32–39. DOI: 10.1007/s101030050018.

[100] Goldenberg A. A. et al. "Robot-assisted MRI-guided prostatic interventions". In: *Robotica* 28 (Mar. 2010), pp. 215–234. DOI: 10.1017/S026357470999066X.

[101] Robert D. Peters et al. "Magnetic resonance thermometry for predicting thermal damage: An application of interstitial laser coagulation in an in vivo canine prostate model". In: *Magnetic Resonance in Medicine* 44.6 (), pp. 873–883. DOI: 10.1002/1522-2594(200012)44:6<873::AID-MRM8>3.0.CO;2-X.

[102] Paola Di Ninni, Fabrizio Martelli, and Giovanni Zaccanti. "The use of India ink in tissue-simulating phantoms". In: *Opt. Express* 18.26 (Dec. 2010), pp. 26854–26865. DOI: 10.1364/OE.18.026854. URL: http://www.opticsexpress.org/abstract.cfm?URI=oe-18-26-26854.

[103] E. Schena et al. "Solutions to Improve the Outcomes of Thermal Treatments in Oncology: Multipoint Temperature Monitoring". In: *IEEE Journal of Electromagnetics, RF and Microwaves in Medicine and Biology* 2.3 (Sept. 2018), pp. 172–178. DOI: 10.1109/JERM.2018.2838341.